Dissertation

Investigation of the dynamics of magnetic vortices and antivortices using micromagnetic simulations

Submitted by

Martin Antonio Asmat-Uceda

Department of Physics

In partial fulfillment of the requirements

For the Degree of Doctor of Philosophy

Colorado State University

Fort Collins, Colorado

Spring 2017

Doctoral Committee:

Advisor: Kristen S. Buchanan

Martin P. Gelfand
Mingzhong Wu
Matthew Shores

Abstract

Investigation of the dynamics of magnetic vortices and antivortices using micromagnetic simulations

This thesis is focused on investigating the dynamic properties of spin textures in patterned magnetic structures by using micromagnetic simulations. These textures become particularly relevant at sub-micron length scales where the interplay between magnetostatic and exchange energy leads to unique properties that are of great interest both from a fundamental perspective and for the development of new technologies. Two different systems, a magnetic antivortex (AV) stabilized in the intersection of perpendicular microwires, and three interacting vortices in an equilateral arrangement, were considered for this study. For the first system, the AV, the formation process and the excitation spectra were investigated. Since the AV is a metastable state, the design of a host structure capable of stabilizing it requires careful consideration and it is desirable to have general guidelines that could help to optimize the AV formation rate. The role of the shape anisotropy and the field dependence of the AV formation process is discussed in detail. Micromagnetic simulations along with magneto-optical Kerr effect and magnetic force microscopy measurements demonstrated that the asymmetry in the structure can be used to promote the formation of such AV's and that regions with lower shape anisotropy lead the reversal process, while simulations of the dynamic response show that when the system is excited with in-plane and out-of-plane external magnetic fields, normal modes with azimuthal and radial characteristics are found, respectively, in addition to the low frequency gyrotropic mode. The modes are influenced by the spin texture in the intersection, which offers additional possibilities for manipulating spin

waves (SW). For the second system, three interacting vortices are simulated and compared with a simple analytical model that considers only dipolar interactions. It was found that when a fitting parameter is introduced to the model, the main features of the simulations are captured better than more complex models, which suggest that this simple framework can be used to accurately model more complex vortex networks.

Acknowledgements

First, I want to thank my advisor Dr. Kristen Buchanan for her guidance and support. Her knowledge and passion for science have been a true inspiration. Also, I want to thank current and former members of the Nanomagnetism group as well as graduate students of Colorado State University who have contributed either by participating directly in some of the projects included in this work or with useful discussions.

This work would have been impossible without the support of my family and friends. Thanks to my wife, Sol T. Cintron-Berdecia, who has always been there fighting this battle side to side with me.

This dissertation is typeset in LaTeX using a document class designed by Leif Anderson.

Table of Contents

List of Tables

List of Figures

List of Symbols

μ_o Permeability of free space ..... T.m/A

γ Gyromagnetic ratio ..... $s^{-1}T^{-1}$

λ Wavelength ..... m

H External magnetic field ..... T

$\tilde{N}$ Demagnetization tensor ..... *unitless*

M_s Saturation magnetization ..... A/m

l_{exch} damping parameter ..... m

A Exchange stiffness constant ..... J/m

List of Acronyms

AV ..... Antivortex

BV ..... Backward volume

FD ..... Finite differences

FE ..... Finite elements

FFT ..... Fast Fourier Transform

FWHM ..... Full width at half maximum

GPU ..... Graphical Processing Unit

IP ..... In-plane

OOP ..... Out-of-plane

LLG ..... Landau Lifshitz Gilbert

MFM ..... Magnetic force microscope

MOKE ..... Magneto-optical Kerr effect

OOMMF ..... Object Oriented Micromagnetic Framework

SEM ..... Scanning electron microscope

SW ..... Spin wave

CHAPTER 1

Introduction

Magnetism is a fascinating phenomenon that has captivated curious human minds since ancient times. Despite early reports by the Greeks, around 2600 years ago, and its wide use in important applications such as navigation, significant advancements in understanding the underlying physics of magnetism had to wait until the development of theories such as electromagnetism, relativity and quantum mechanics, in the last two centuries. Along with these major breakthroughs, applications involving magnetism and magnetic materials have become ubiquitous. A few examples include microphones, speakers, transformers, motors, burglar alarms, magnetic resonance imaging (MRI), levitating trains and magnetic recording. Furthermore, fast-paced advances in spintronics, magnonics and related fields are continuously leading to new technologies such as microwave spin torque oscillators and non-volatile memories that transform our daily lives and advance our civilization.

Recent progress in fabrication techniques [1–7] has allowed manufacturing of smaller devices, with sizes in the micro- and nano-scale. When the dimensions of magnetic systems are reduced to these scales interesting effects take place due to the spatial confinement, for example, the wave vector of the elementary excitations becomes quantized. Another important consequence of reducing the size of magnetic elements is the appearance of new and exotic magnetic states with non-trivial topological properties such as the magnetic vortex and the antivortex (AV).

Magnetic vortex and AV states are spatially inhomogeneous configurations where the spins have an in-plane (IP) curling distribution around a small central core region (see figure 1.1a). Both vortex and AV states have some common properties such as the small core

region, which is usually a few nanometers, where the magnetization points out of the plane (OOP). Their IP magnetizations have very distinct configuration though. In the AV, the spins orient such that they point towards the core from opposite sides and away from it in the perpendicular direction. The vortex on the other hand has a magnetization that curls tangentially to concentric circles. The vortex is usually the ground state of sub-micron elements, such as disks or squares, over a considerable range of aspect ratios [8], however the AV is in contrast a metastable state and therefore more difficult to stabilize. A vortex and AV can annihilate each other upon meeting, radiating spin waves (SW).

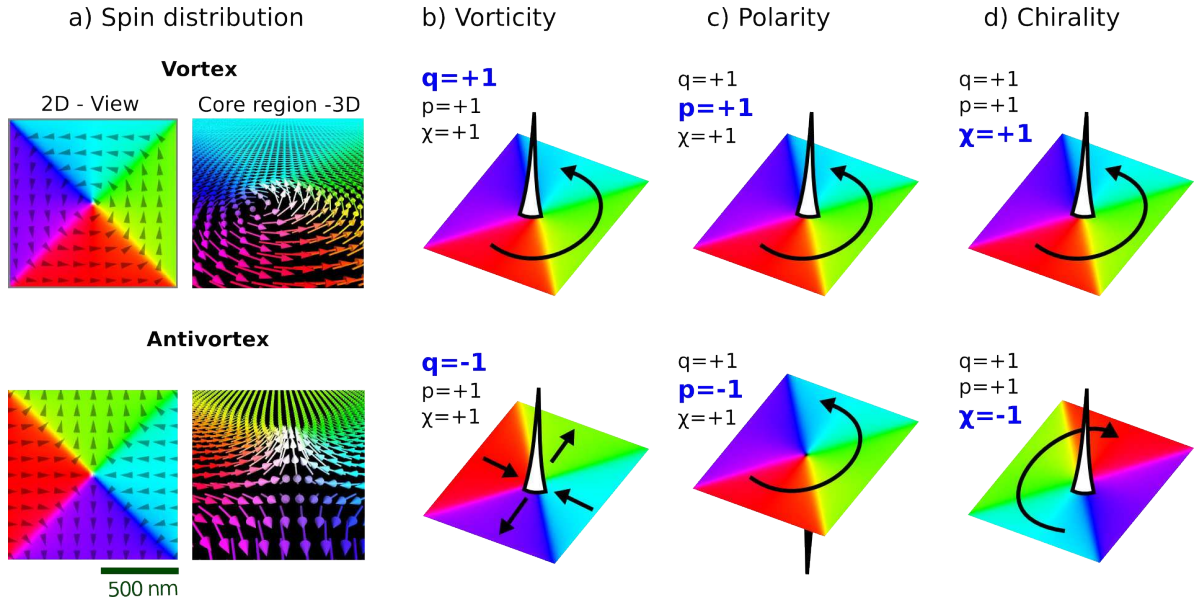

Figure 1.1. Spin distribution and topological parameters of vortex-like textures. Spatial distributions of the magnetization for a vortex (top) and AV (bottom) are shown in a) where the core region is ∼40 nm for both cases. The effect of changing the values for the vorticity b), polarity c), and chirality d) parameters are also illustrated. The color indicates the direction of the spins, a color wheel with clockwise circulation would go from red (right), to green, cyan, purple, and black to red. Differences in the color sequence for vortex and AV are due to the different in-plane orientations of the spins for both magnetic states.

Both states can be described by three parameters, namely their vorticity q, chirality χ, and polarity p. The vorticity q, also known as winding number or topological charge, describes the number of windings that the in-plane projection of the magnetization vector

experiences when following a circular contour around the core. It has the values of +1 and -1 for vortices and AV, respectively. This quantity is said to be a topological invariant because its value does not change under any continuous deformation of the magnetization. The sense of rotation of the magnetization in a circular contour around the core is determined by χ. It can be either clockwise ($\chi = -1$) or counterclockwise ($\chi = +1$). The polarity p defines the out-of-plane orientation of the core and takes values of +1 and -1 for vectors that are oriented parallel and antiparallel to the positive normal vector of the surface. These parameters are illustrated in figure 1.1b-d).

Given the unique properties of these magnetic textures the excitation of SW becomes, in general, more complex than in systems with homogeneous magnetizations. Understanding the magnetization dynamics in small patterned structures is not only relevant from a fundamental point of view but it is also important for technological purposes. As new technologies push towards higher speeds and further miniaturization, patterned magnetic elements with sub-micron lateral dimensions and with operating frequencies in the microwave range are required. Spin textures may offer new functionalities.

The present work used micromagnetic simulations to study the dynamics of magnetic vortices and AV. Micromagnetic simulations are a powerful tool that in conjunction with analytical theory and experimental approaches or even by themselves can provide insightful information about the dynamic properties of magnetic elements. For example, when investigating patterned structures a rigorous theoretical approach can easily become too complex due to the challenge of dealing with the long-range dipolar interaction, however simulations can be used to validate simpler analytical models. On the other hand, experimental techniques are limited to the availability, resolution and the sensibility of equipment, e.g. imaging

techniques such as transmission X-ray microscopy can provide resolutions of up to $\sim$ 20 nm [9], however, there are still challenges like imaging the details of the 3D spin texture. In addition, simulations can provide information about quantities that are not always easy to deduce from experiment such as the different energy contributions.

In particular two different magnetic systems were investigated in this work. The first system consisted of magnetic AVs stabilized in intersecting microstrips. AVs are states that have not been explored as thoroughly as their vortex counterpart, although their particular spin configuration may be preferable for certain technological applications, e.g., their ability to channel SW's in intersecting microwires can be exploited for circulator devices. Micromagnetic and experimental studies on the dynamics of AVs report on a gyrotropic and azimuthal modes [10–18], similar to the vortex states, however the interaction of these AV modes with adjacent wires has not yet been investigated despite the fact that intersecting microstrips are natural geometries that can help stabilize isolated AVs. In this work the dynamic excitations of magnetic AVs were studied in connection with the dynamic modes in the adjacent microstrips. Since the AVs are metastable states, the formation and stabilization process is not a trivial task and the role of the shape anisotropy and field treatment in the formation of stable AVs was also addressed.

The second system consisted of three disks, in a triangular arrangement, that are coupled magnetostatically and each one hosts a magnetic vortex. Vortices are the ground state in many sub-micron elements and great candidates for applications including magnonic crystals, logic devices and biomedical applications, among others, that involve either arrays or large groups of magnetic vortices that can interact magnetostatically. Different models have been proposed to describe the interaction of magnetic vortices [19–21] and each one involves

different degrees of mathematical complexity, however, simpler models might also be useful and accurate enough to capture the main coupling effects. Here, micromagnetic simulations of coupled vortices are compared with a simple analytical model that takes into account dipolar interactions only. This model was formulated by one of our collaborators at Johns Hopkins University. The results of the micromagnetic simulations were also compared to experimental measurements, some of which I made and others were performed by collaborators at Colorado State University, Argonne National Laboratory and Bryn Mawr University.

This thesis is organized as follows:

Chapter 2 provides a brief introduction to the micromagnetic theory and the relevant energy terms. It also gives a brief description of the equation of motion for the magnetization, namely the Landau-Lifshitz-Gilbert (LLG) equation, that is used extensively for micromagnetic modeling.

Chapter 3 describes the methods used in this thesis. The details of the computational procedure for running typical micromagnetic simulations are described as well as the post-analysis process. The experimental techniques used are also presented.

Chapter 4 discusses the problem of the creation and stabilization of isolated magnetic AV in patterned microstructures. A combination of micromagnetic simulations and experimental measurements were used to investigate the effects of structure shape and the field history on the formation of AV. Hysteresis loops were simulated to examine the nucleation and annihilation mechanisms during the reversal and are compared with experimental results.

Chapter 5 addresses the dynamic excitations of magnetic AV stabilized in intersecting microstrips. Micromagnetic simulations reveal a rich excitation spectrum, especially in the

high frequency range, as well as the existence of gyrotropic, azimuthal and radial resonant modes similar to those of a magnetic vortex. In-plane and out-of-plane pulsed magnetic fields are used to selectively excite these modes and spatial modes maps are obtained by using Fourier analysis. The effect that the static spin configuration in the intersection has on the excitations in the legs is also investigated.

Chapter 6 uses micromagnetic simulations to explore the dynamics of magnetic vortices that interact via dipolar coupling. A system of three disks, each containing a single vortex, arranged in an equilateral triangle configuration is studied. A splitting of the gyrotropic frequency is observed due to the magnetostatic coupling when the disks separation is small. The effect of the polarities and chiralities on the frequencies observed is also explored.

Finally in **Chapter 7** a summary of the work and different results discussed in previous chapters is presented, followed by an outlook on future directions.

Some of the results presented in this dissertation have been already published in different scientific journals. Reference [22] summarizes the results discussed in Chapter 4, while references [23] and [24] are relevant for Chapter 6. Chapter 5 is the most recent one and although some of content discussed there has been published as part of an experimental paper in reference [18], most of the simulations results included there have been submitted for publication and are currently undergoing a peer review process.

CHAPTER 2

Theoretical Background

2.1. Micromagnetic Theory

Ferromagnetism, the phenomenon by which materials such as iron exhibit spontaneous magnetization below a critical temperature, is a quantum-mechanical effect caused by the electron spin and the exchange interaction that tends to align neighbouring spins parallel to each other. However, due to the large number of spins involved, a quantum-mechanical description of ferromagnetism at the atomic level is usually restricted to very small systems and approximate models are preferred for sizes above the nanometer length-scale. The selection of an alternative model depends on the characteristic length-scales. The behaviour of ferromagnets in the so-called mesoscopic regime, which is an intermediate length scale between the atomic and macroscopic (or between the crystal lattice and magnetic domain) limits, is commonly described using the micromagnetic theory.

Micromagnetics is a continuum theory that allows for the computation of the magnetization, i.e. the vector field that specify local orientation of magnetic moments, of ferromagnetic materials with arbitrary shapes as well as its time evolution. In the micromagnetic model the atomic structure is ignored and quantum-mechanical effects are approximated using classical approximations, for example, the interatomic exchange constant is replaced with an exchange stiffness parameter and the magnetization is treated as a classical vector that varies slowly in space. For this reason micromagnetics is also referred to as a quasi-classical approach.

Micromagnetics is largely based on the work formulated by Landau and Lifshitz in 1935 [25] and developed further by Brown [26]. Gilbert later [27, 28] introduced a phenomenological damping term to avoid unphysical solutions. The goal of these theories was to explain the

hysteretic behavior of ferro- and ferrimagnetic materials through the multiplicity of local energy minima, however with the advent of high-speed computers and sophisticated algorithms, micromagnetic simulations have become a powerful tool and simulations are routinely used in the design and analysis of magnetic devices including nonvolatile magnetic random access memories[29–31], frequency-tunable microwave oscillators[32, 33], and logic devices [34–38].

2.2. The Micromagnetic Model

Modern micromagnetic theory treats the magnetization as a continuous function of position $\mathbf{M}(\mathbf{r})$ and describes its response to an effective field as a function of time. This effective field is defined as a functional derivative of the free energy and behaves as a real magnetic field acting on the magnetization. The basic assumptions of the model are [39]:

- All vector quantities vary slowly at the atomic scale. This ensures that the discrete character of the system can be disregarded and that it can be described using a continuum approximation instead.

- The modulus of the magnetization is constant ($\mathbf{M} = M_s\mathbf{m}$ with $|\mathbf{m}| = 1$), where M_s is the magnetization per unit volume and the unit vector $\mathbf{m}$ indicates the direction of the magnetization. This is related to the fact that the density of magnetic moments is assumed to be homogeneous. Since $|m_x^2 + m_y^2 + m_z^2| = 1$, this condition also reduces the number of degrees of freedom of the magnetization to two.

The dynamic evolution of the magnetization is described by a set of nonlinear equations, commonly expressed in vector form, known as the Landau-Lifshitz-Gilbert (LLG) equation. Since the modulus of the magnetization is constant, the problem is then to find its spatial orientation, given by the reduced magnetization vector $\mathbf{m}$ in each cell. The micromagnetic

theory provides a framework to study ferromagnetic bodies, which are in general complex nonlinear systems, and allows us to perform an analysis of the magnetization. This is important from both a scientific and technological perspectives as it can be used to find the equilibrium spin configuration, which can be done using either the LLG equation or by minimizing the energy, to simulate reversal (hysteresis) processes, and to model magnetization relaxation and dynamics.

In ferromagnetic materials the interatomic exchange interaction aligns the magnetic moments parallel to each other over certain length known as the exchange length (defined in equation 2.14). In practice the ferromagnetic sample is divided into cells, often rectangular but sometimes other shapes can be used (e.g., finite element mesh), where each cell has a constant magnetization per unit volume M_s. The direction of the magnetization is free to rotate in each cell. The dimensions of the cell are typically chosen to be on the order of the exchange length or smaller, then the direction of the magnetization varies smoothly from cell to cell. The cell dimensions are, however, usually large compared to the lattice constant such that each cell contains many atoms within its volume. Consequently the discrete nature of the material can be ignored.

2.3. Micromagnetic Energy

The micromagnetic energy of the system in a typical simulation includes several contributions such as the demagnetization energy, E_d, anisotropy energy, E_{anis}, Zeeman energy, E_{Zee}, and exchange energy, E_{exch}, and the total energy can be expressed as the sum of all those contributions:

$$E = E_{zee} + E_d + E_{exch} + E_{anis}. \tag{2.1}$$

The model can be also be extended to include additional energy terms, such as magnetoelastic, Dzyaloshinkii-Moriya [40], and thermal effects (by introducing random local fluctuations to the magnetic moments [26]), however these were neglected in this work. Spin transfer torque effects can also be included but this requires modification of the LLG equation [41].

2.3.1. Zeeman Energy

This is the energy associated with the interaction between the ferromagnet and an external magnetic field $\mathbf{H}_{ext}$ and is defined as:

$$E_{Zee} = -\mu_o \int \mathbf{H}_{ext} \cdot \mathbf{M}(\mathbf{r}) d^3 r, \tag{2.2}$$

where the integration is over the ferromagnetic body and the same is true for each of the other energy terms therefore it will be implicitly assumed unless stated otherwise. The lowest energy state is obtained when $\mathbf{M}$ is aligned parallel to $\mathbf{H}_{ext}$ while the highest energy state corresponds to anti-parallel alignment of $\mathbf{M}$ with respect to $\mathbf{H}_{ext}$.

2.3.2. Demagnetization energy

The demagnetization energy E_d or magnetostatic self-interaction energy is caused by the dipole-dipole interaction between atomic moments within the magnetic material. This energy is associated with a demagnetizing field, $\mathbf{H}_d(\mathbf{r})$, is such that:

$$E_d = -\frac{1}{2}\mu_o \int \mathbf{M}(\mathbf{r}) \cdot \mathbf{H}_d(\mathbf{r}) d^3 r. \tag{2.3}$$

The demagnetizing field $\mathbf{H}_d(\mathbf{r})$ is the field generated by all the magnetic moments in the sample. Computing $\mathbf{H}_d(\mathbf{r})$ can be a very difficult task, even when the magnetization $\mathbf{M}(\mathbf{r})$ at all points must is known. To simplify this calculation it is convenient to express it in terms of the so-called demagnetization tensor. The demagnetizing field at point $\mathbf{r}$ produced by a continuous magnetization at point $\mathbf{r}'$ is expressed as (see subsection 2.6.1.2)

$$\mathbf{H}_d(\mathbf{r}) = -\int \tilde{N}(\mathbf{r},\mathbf{r}')\mathbf{M}(\mathbf{r}'))d^3r', \tag{2.4}$$

where $\tilde{N}(\mathbf{r},\mathbf{r}')$ is a symmetric second rank tensor, referred to as the demagnetization tensor, and it depends only on the geometry of the sample but not on its absolute dimensions or physical properties. This tensor is usually written in matrix notation and its elements $N_{ij}(\mathbf{r},\mathbf{r}')$ are called demagnetization factors,

$$\tilde{N}(\mathbf{r}) = \begin{pmatrix} N_{xx}(\mathbf{r}) & N_{xy}(\mathbf{r}) & N_{xz}(\mathbf{r}) \\ N_{xy}(\mathbf{r}) & N_{yy}(\mathbf{r}) & N_{yz}(\mathbf{r}) \\ N_{xz}(\mathbf{r}) & N_{yz}(\mathbf{r}) & N_{zz}(\mathbf{r}) \end{pmatrix}. \tag{2.5}$$

Here $\mathbf{r}'$ was chosen to be at the origin of coordinates, $\tilde{N}(\mathbf{r},0) = \tilde{N}(\mathbf{r})$. The diagonal elements are non-negative and satisfy $Tr(\tilde{N}(\mathbf{r})) = N_{xx}(\mathbf{r}) + N_{yy}(\mathbf{r}) + N_{zz}(\mathbf{r}) = 1$. In general this tensor is a point function, however in the case of a uniformly magnetized ellipsoidal ferromagnet its elements are constant throughout the entire sample. Moreover, if the ellipsoid is homogeneously magnetized along one of the the axis of symmetry, it becomes a diagonal

tensor, N_d:

$$N_d = \begin{pmatrix} N_x & 0 & 0 \\ 0 & N_y & 0 \\ 0 & 0 & N_z \end{pmatrix}, \tag{2.6}$$

and the demagnetizing field can be written as

$$\mathbf{H}_d = -N_d \mathbf{M}. \tag{2.7}$$

The demagnetizing field for a ferromagnet of arbitrary shape is non-uniform, even if the sample is uniformly magnetized, and in general can be an extraordinarily complicated function of position. Analytical expressions and tables for the demagnetizing factors of ellipsoids can be found in Refs. [42–45]. For micromagnetic simulations rectangular cells are frequently used, each with a uniform magnetization, and the expressions for N_d can be found in Refs. [46–50].

All of the energy contributions except for E_d depend on the magnetization in just the nearby cells, whereas E_d involves long range interactions, often over the full extent of the structure. Consequently the evaluation of E_d is usually the most memory intensive and time-consuming part of the micromagnetic simulations as will be discussed in a later section.

2.3.3. Exchange energy

This energy term is associated with the quantum-mechanical exchange interaction that promotes the parallel alignment of neighbouring spins. This interaction is, in turn, related to the Pauli exclusion principle and the exchange symmetry, which requires that the physical observables be unaffected by exchanging two indistinguishable particles.

For a qualitatively description consider a system of two electrons with overlapping wave functions. Since electron are fermions, the wavefunction of the system must be antisymmetric with respect to exchange. If we have parallel orientation of the spins i.e. a symmetric SW function, the spatial part must be antisymmetric which is associated with a larger mean distance between electrons and therefore a reduction of the electrostatic energy. On the other hand, due to the Pauli exclusion principle, electrons with parallel spins must occupy different orbitals, increasing the energy of the system. In the case of ferromagnetic materials the reduction in electrostatic energy dominates and the net balance of energy is such that parallel alignment of the spins is favored.

The exchange energy of two adjacent atoms i, j with spin operators $\hat{\mathbf{S}}_i$ and $\hat{\mathbf{S}}_j$ is usually described by the Heisenberg Hamiltonian, E_{exch} [51]:

$$E_{exch} = -J_{ij}\hat{\mathbf{S}}_i \cdot \hat{\mathbf{S}}_j, \tag{2.8}$$

where the coefficient J_{ij} is known as exchange integral and determines the strength of the interaction. The generalization of the above expression to a system of many localized atomic spins can be obtained by summing over all pairs of atoms on site i, j. However since the exchange interaction is short ranged, usually only nearest neighbours are considered and the Hamiltonian is simplified to a sum with a single exchange constant J:

$$E_{exch} = -J\sum_{i<j}^{NN} \hat{\mathbf{S}}_i \cdot \hat{\mathbf{S}}_j, \tag{2.9}$$

where the restriction $i < j$ ensures that each pair is counted only once and the superscript NN indicates that the sum is over nearest neighbors only. In the quasi-classical approximation, the spin operators are replaced by classical vectors $\mathbf{S}_i$, $\mathbf{S}_j$ with constant magnitude S and unit vectors $\mathbf{s}_i$ and $\mathbf{s}_j$, then the exchange energy can be written as

$$E_{exch} = -J \sum_{i<j}^{NN} \mathbf{S}_i \cdot \mathbf{S}_j \approx -JS^2 \sum_{i<j}^{NN} \cos\theta_{ij}. \tag{2.10}$$

The exchange energy is proportional to the angle between the two spins and the energy reaches a minimum when the spins are parallel (positive J) or anti-parallel (negative J). In addition, if the angle between adjacent spins, θ_{ij}, is small the cosine may be expanded as $\cos\theta_{ij} \approx 1 - \theta_{ij}^2/2! + ...$, such that (neglecting the constant energy term):

$$E_{exch} = JS^2 \sum_{i<j} \theta_{ij}^2. \tag{2.11}$$

Furthermore, a first-order Taylor expansion allows us to write $|\theta_{ij}| \approx |(\mathbf{r}_{ij} \cdot \nabla)\mathbf{s}_j|$, where $\mathbf{r}_{ij}$ is a unit vector that connects lattice points i and j. The exchange energy can then be written as

$$E_{exch} = JS^2 \sum_{i} \sum_{r_{ij}} |(\mathbf{r}_{ij} \cdot \nabla)\mathbf{s}_j|^2. \tag{2.12}$$

In the continuum approximation the unit vector of the atomic spin $\mathbf{s}_i$ is replaced by $\mathbf{m}_i$, the unit vector of the magnetization of cell i (remember that the volume was divided in several cells) and the discrete sum is replaced by an integral. The exchange energy is now written as

$$E_{exch} = \int A(\nabla \mathbf{m})^2 d^3r, \tag{2.13}$$

where A is material-dependent value ($1 - 2 \times 10^{-11}$ J/m for most ferromagnets) that is known as the exchange stiffness constant and is given by $A = \frac{JS^2z}{a}$, where a is the distance between nearest-neighbours and z is an integer that depends on the symmetry of the lattice. Equation 2.13 relates detailed atomic properties to the spatial variation of the magnetization, and tell us that non-uniform distributions of the magnetization have an associated cost in exchange energy.

It is also important to mention that the Heisenberg model assumes localized spins that interact weakly, however, this is not the case in ferromagnetic metals. Exchange is more complex in that case and a description in terms of itinerant electrons and band magnetism is frequently required. The Heisenberg formalism nevertheless provides a useful phenomenological description of the exchange stiffness effect and is commonly used within the continuum approximation.

The competition between magnetostatic and exchange energies leads to the definition of a characteristic length:

$$l_{exch} = \sqrt{\frac{A}{\mu_o M_s^2}}, \tag{2.14}$$

known as the magnetostatic exchange length. This quantity represents the distance over which the exchange interaction counteracts the dipolar interaction and it sets the length scale for domain walls and vortex cores. Typical values for l_{exch} in ferromagnets are on the order of a few nanometers.

2.3.4. Anisotropy energy

In a ferromagnet it is observed that the magnetization generally tends to align along certain preferred directions with respect to the crystalline axes and/or to the external shape of the sample. This property is called magnetic anisotropy. The anisotropy energy is defined as the energy that it takes to rotate the magnetization direction from a direction of low energy towards one of high energy.

Some common types of anisotropy include crystalline (E_K), shape (E_{shape}), and stress-induced (E_{stress}). As a general rule, all of the anisotropy types are present simultaneously in the material, though in some cases of interest one may dominate. Here we will discuss the first two anisotropy types since the are the most relevant to the work that will follow.

2.3.4.1. *Magnetocrystalline Anisotropy.* Magnetocrystalline anisotropy is an intrinsic property that makes it easy to align the magnetization along certain crystallographic directions and it has its origin in spin-orbit coupling (which is a relativistic effect). Thus, materials with rare-earth elements often have strong spin-orbit coupling and significant magnetocrystalline anisotropy. The symmetry of the magnetocrystalline anisotropy reflects the crystalline symmetry of the material. In the case of cubic materials, for example, the anisotropy energy can be written as an expansion of the direction cosines with respect to the cubic axes α_i :

$$E_K = K_0 + K_1(\alpha_1^2\alpha_2^2 + \alpha_2^2\alpha_3^2 + \alpha_1^2\alpha_3^2) + K_2(\alpha_1^2\alpha_2^2\alpha_3^2) + ..., \tag{2.15}$$

with $K_0, K_1, etc.$ are anisotropy constants. Depending on the specific material and experiment, one might have higher order terms. In practice K_i's are treated as empirical constants

obtained usually from angle-dependent hysteresis or from ferromagnetic resonance experiments [52]. In this thesis the materials studied are magnetically soft, which means that the magnetocrystalline anisotropy is small and in most cases can be neglected.

2.3.4.2. *Shape Anisotropy.* Shape anisotropy is the result of the non-spherical shape of the material and although it does not constitute a separate energy contribution -it is, in fact, a consequence of the demagnetization energy- it is a term that is used frequently in the discussion of magnetic nanostructures. The effects of shape anisotropy are usually described in terms of the demagnetizing tensor, discussed in the previous section. Shape anisotropy is important when magnetocrystalline anisotropy is small, for instance when the material is polycrystalline with random grain orientations. Consider a prolate ellipsoid as the one shown in Fig. 2.1a, in which case the component of N_d and therefore the demagnetizing field along the long axis is very small (see equation 2.7). Consequently, it will require little to no field to saturate the ellipsoid along the long axis, whereas along the short axis the demagnetizing field is big and a large field is needed instead. An expression for the energy associated with the shape anisotropy can be obtained combining eqs. 2.3 and 2.7 for the case of a uniformly magnetized ellipsoid as

$$E_{shape} = -\frac{\mu_o}{2}\int \mathbf{M}\cdot(-\tilde{N}_d\mathbf{M})d^3r = \frac{\mu_o V}{2}(N_x M_x^2 + N_y M_y^2 + N_z M_z^2), \tag{2.16}$$

where V represents the volume of the ellipsoid. In the case that the ellipsoid is magnetized along one of the axes $i = x, y, z$ the only non-zero component of the magnetization is M_i and the energy is proportional to the demagnetization factor such that

$$E_{shape}(M \parallel i) = \left(\frac{\mu_o V M_i^2}{2}\right) N_i, \tag{2.17}$$

which tell us that the shape anisotropy energy is minimized when the sample is magnetized along the axis with lower N_i as illustrated figs. 2.1b-d.

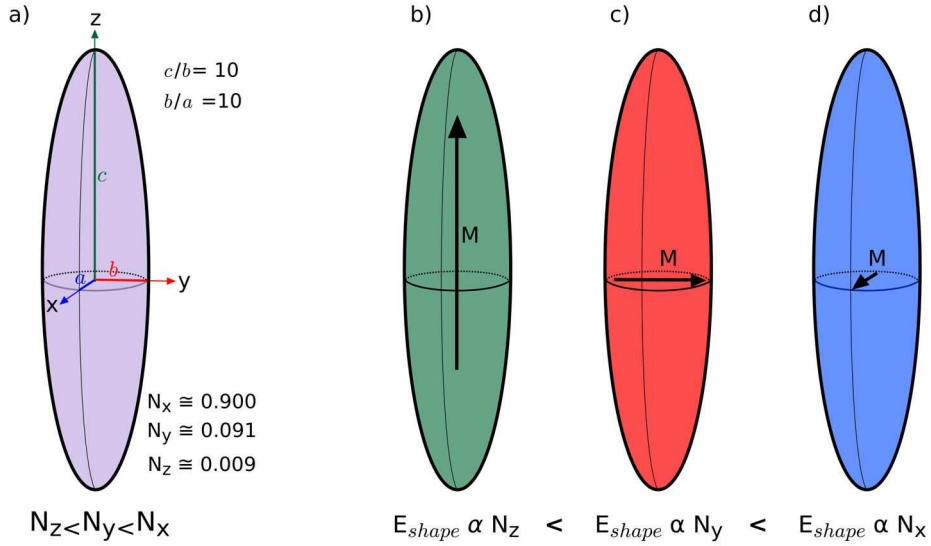

Figure 2.1. The effect of shape anisotropy is illustrated for a prolated ellipsoid. The geometry determines the demagnetization coefficients N_x, N_y and N_z along the different axes shown in a). Since the shape anisotropy energy is proportional to these coefficients, the magnetization tends to align along the axis with lower demagnetization factor such that the energy is minimized. Values of demagnetization coefficients were extracted from [53].

2.4. Brown's equations of micromagnetism

The initial formulation of the micromagnetic theory by Brown [26] followed an energy minimization process to find the equilibrium magnetization configuration. The total energy $E(\mathbf{M}(\mathbf{r}))$ is obtained by summing all of the contributions discussed in the previous subsections (no anisotropy) and integrating over the entire volume of the ferromagnet:

$$E(\mathbf{M}(\mathbf{r})) = \int \left[-\mu_o M_s(\mathbf{H}_{ext} \cdot \mathbf{m}) - \frac{1}{2}\mu_o M_s(\mathbf{H}_d \cdot \mathbf{m}) + A(\nabla \mathbf{m})^2 \right] d^3r. \tag{2.18}$$

An effective field, $\mathbf{H}_{eff}$, is defined in terms of the total energy:

$$\mathbf{H}_{eff} = -\frac{1}{\mu_o}\frac{\delta E}{\delta \mathbf{M}}, \tag{2.19}$$

where $\frac{\delta E}{\delta \mathbf{M}}$ is the functional derivative of the energy with respect to the magnetization. In practice this derivative is calculated using the definition of a variation, δE,

$$\delta E = E(\mathbf{M} + \delta\mathbf{M}) - E(\mathbf{M}) = \int \frac{\delta E}{\delta \mathbf{M}} \cdot \delta\mathbf{M} dV, \tag{2.20}$$

where $\delta\mathbf{M}$ represents a small variation of the magnetization.

The minimization of energy by standard variational principles leads to the condition under which the system reaches equilibrium:

$$\mathbf{m} \times (\mathbf{H}_{ext} + \mathbf{H}_d + \frac{2A}{\mu_o M_s}\nabla^2\mathbf{m}) = 0. \tag{2.21}$$

This condition can frequently expressed in terms of the effective field [54], and together with a boundary condition for the magnetization, are known as Brown's equations of micromagnetism:

$$\begin{cases} \mathbf{m} \times \mathbf{H}_{eff} = 0 \\ \left.\frac{\partial \mathbf{m}}{\partial n}\right|_S = 0, \end{cases} \tag{2.22}$$

where S and n represents the surface and the direction normal to the surface of the ferromagnet respectively. The first equation means that in order to reach equilibrium the torque that the effective field exerts on the magnetization has to vanish. This corresponds to the situation when the magnetization is parallel to the effective field. The second equation defines a boundary condition for the magnetization; this is usually not addressed in Maxwell's

equation of electromagnetism where only boundary conditions for the normal components of the magnetic flux density B and tangential components of the magnetic field H are specified. To deal with the inhomogeneity of the magnetic field near the boundary, two boundary conditions are usually introduced: pinned or unpinned magnetization. The equation shown above represents the case of "unpinned" magnetization, i.e. a situation where the spins at the surface are totally free to rotate as opposed to the case of "pinned" magnetization ($\mathbf{M} = 0$) where the orientation of the spins at the surface of the ferromagnet is fixed. For a more extensive discussion of the boundary conditions for the magnetization see [55] and references therein.

The energy landscape is, in general, not trivial. It usually contains several local extrema and saddle points, therefore the minimization process generates results that depend strongly on the initial magnetic state. The formalism presented so far can be used to find the equilibrium magnetization but it does not provide any information how the system evolves from an initial state towards that equilibrium. The formalism that is used to describe the magnetization dynamics is presented in the following section.

2.5. LLG equation

This equation describes the dynamics of the magnetization field $\mathbf{m}(\mathbf{r}, t)$. It links the magnetization to the effective field $\mathbf{H}_{eff}$ (and hence to the total energy) such that:

$$\frac{d\mathbf{m}}{dt} = -|\gamma_o|(\mathbf{m} \times \mathbf{H}_{eff}) + \alpha \left[\mathbf{m} \times \frac{d\mathbf{m}}{dt}\right], \tag{2.23}$$

where γ_o is the gyromagnetic ratio of the electron ($|\gamma_o| \approx 176.1$ MHz/mT or $\approx 2.2 \times 10^5$ $(\mathrm{A/m})^{-1}\mathrm{s}^{-1}$) that connects the magnetic dipole moment of a particle to its angular

momentum. The LLG equation describes a damped gyromagnetic precession. The first term in the right hand side represents the Larmor precession of $\mathbf{m}$ about the direction of the effective field due to the torque $\mathbf{m} \times \mathbf{H}_{eff}$. The second term is a phenomenological damping term that describes the dissipation of energy, where α is a dimensionless, effective damping parameter and its value depends on the material, for example for Fe, Ni and Co metals and alloys α=0.001-0.01 while for ferro- and ferrimagnetic oxides it can even be one or two orders of magnitude smaller.

Scalar multiplication by $\mathbf{m}$ on both sides of the LLG equation will produce:

$$\frac{d}{dt}(\mathbf{m} \cdot \mathbf{m}) = 0, \tag{2.24}$$

showing that it preserves the magnitude of the magnetization as required by the micromagnetic theory.

Despite the apparent simplicity of the LLG equation, it is non-linear and involves a complicated spatial dependence because the effective field at one cell depends on the magnetization at every cell. Due to this complexity the LLG equation is generally solved using numerical techniques.

For efficient implementation of numerical solutions it is convenient to write the LLG equation in its simplest form. For example the term $\frac{d\mathbf{m}}{dt}$ appears on both sides of equation 2.23 however this can be can be written in a more tractable way by performing a vector multiplication by $\mathbf{m}$ on both sides such that

$$\mathbf{m} \times \frac{d\mathbf{m}}{dt} = -|\gamma_o|\mathbf{m} \times (\mathbf{m} \times \mathbf{H}_{eff}) + \alpha \mathbf{m} \times \left[\mathbf{m} \times \frac{d\mathbf{m}}{dt}\right]. \tag{2.25}$$

Using the identity $\mathbf{a} \times (\mathbf{b} \times \mathbf{c}) = (\mathbf{a} \cdot \mathbf{c})\mathbf{b} - (\mathbf{a} \cdot \mathbf{b})\mathbf{c}$ and $\mathbf{m} \cdot d\mathbf{m}/dt = 0$, we have that

$$\mathbf{m} \times \frac{d\mathbf{m}}{dt} = -|\gamma_o|\mathbf{m} \times (\mathbf{m} \times \mathbf{H}_{eff}) - \alpha \frac{d\mathbf{m}}{dt}. \tag{2.26}$$

This expression can be substituted on the right hand side of equation 2.23 to obtain

$$\frac{d\mathbf{m}}{dt} = -\gamma' (\mathbf{m} \times \mathbf{H}_{eff}) + \alpha' [\mathbf{m} \times (\mathbf{m} \times \mathbf{H}_{eff})], \tag{2.27}$$

where

$$\gamma' = \left(\frac{|\gamma_o|}{1 + \alpha^2} \right) \text{ and, } \alpha' = \alpha \left(\frac{|\gamma_o|}{1 + \alpha^2} \right).$$

2.6. Computational approach

For computational micromagnetics the magnetization distribution at time t_0=0, $\mathbf{M}(x, y, z, t_o)$ and material appropriate parameters needs to be defined. This information is then fed into the LLG equation to find the magnetization distribution at a later time t, $\mathbf{M}(x, y, z, t)$, and this process is repeated iteratively to find the magnetization at even later times. To implement this idea, the continuous space and time domain is usually replaced by a set of discrete set of points and the relevant equations are solved numerically for each cell.

Most micromagnetic solvers currently available are based on finite-elements (FE) or finite-differences (FD) methods. In the FE method the space is divided into polyhedral elements, usually tetrahedra (four triangular faces and four vertices or nodes) or hexahedra (six faces, eight vertices for cuboidal hexahedra). The mesh generation is a non-trivial task and adaptive mesh generation techniques, that decide whether an element needs to be refined or not by calculating the error associated with each element, are usually implemented.

FE allows local modification of the number of elements and nodes, i.e., irregular (or unstructured) meshes and it is widely used to solve problems with curved or complex geometries or in situations where the properties vary locally. For example, regions where the magnetization changes quickly can lead to large errors that can be reduced by refining the mesh, while in regions where the magnetization is expected to be smooth it can be coarsened to reduce the computational expense.

On the other hand, in the FD method the space is divided into regular cuboid cells and it is preferable when the geometry is based on rectangular shapes. It usually requires less computer memory than the FE method.

Once the discretization is established, there are two major tasks that require special attention: 1) Calculating the demagnetizing field and 2) Determination of the initial magnetization distribution. A brief overview of both is given here. For a review on the common methods used in micromagnetics see reference [56].

2.6.1. Calculation of the demagnetizing field

This is the most time-consuming part of any micromagnetic simulation, due to the long-range nature of $\mathbf{H}_d$, and considerable effort has been put into finding more efficient ways to do this task. A distinction can be made between solvers that find the demagnetizing field by calculating the scalar potential and those who use a convolution of the demagnetization tensor and the magnetization.

2.6.1.1. *Vector Potential.* If there are no currents, i.e. ($\mathbf{J} = 0$), Ampere's law $\nabla \times \mathbf{H} = \mathbf{J}$ allows the introduction of a magnetic scalar potential Φ_M such that:

$$\mathbf{H}_d = -\nabla \Phi_M. \tag{2.28}$$

Considering that $\mathbf{B} = \mu_o(\mathbf{M} + \mathbf{H})$ and since $\nabla \cdot \mathbf{B} = 0$, then $\nabla \cdot \mathbf{H} = -\nabla \cdot \mathbf{M}$ and it can be shown that the potential Φ_M satisfies Poisson's equation:

$$\nabla^2 \Phi_M = -\rho_M, \tag{2.29}$$

where $\rho_M = \nabla \cdot \mathbf{M}$ is sometimes referred as magnetostatic volume charge (or pole). Solving Poisson's equation gives the magnetization-dependent potential Φ_M [57]:

$$\Phi_M = -\frac{1}{4\pi} \int_V \frac{\nabla' \cdot \mathbf{M}(\mathbf{r}')}{|\mathbf{r} - \mathbf{r}'|} d^3 r' + \frac{1}{4\pi} \int_S \frac{\mathbf{M}(\mathbf{r}') \cdot \mathbf{n}}{|\mathbf{r} - \mathbf{r}'|} d^2 r' \tag{2.30}$$

where $\mathbf{n}$ is the unit vector normal to the surface. The second term is integrated over the surface of the magnetic body and it can be rewritten as a volume integral by using the divergence theorem,

$$\Phi_M = -\frac{1}{4\pi} \int \left[\frac{\nabla' \cdot \mathbf{M}(\mathbf{r}')}{|\mathbf{r} - \mathbf{r}'|} + \nabla' \cdot \left(\frac{\mathbf{M}(\mathbf{r}')}{|\mathbf{r} - \mathbf{r}'|} \right) \right] d^3 r' \tag{2.31}$$

and using the property for the divergence of a product between a vector and a scalar function, the last equation can be written as

$$\Phi_M = \frac{1}{4\pi} \int \nabla' \left(\frac{1}{|\mathbf{r} - \mathbf{r}'|} \right) \cdot \mathbf{M}(\mathbf{r}') d^3 r'. \tag{2.32}$$

Replacing this expression in equation 2.28 gives the demagnetizing field as:

$$\mathbf{H}_d = \frac{1}{4\pi} \nabla \left[\int \nabla' \left(\frac{1}{|\mathbf{r} - \mathbf{r}'|} \right) \cdot \mathbf{M}(\mathbf{r}') d^3 r' \right], \tag{2.33}$$

which in turn can be used in equation 2.3 to calculate the E_d. Although this procedure can potentially lead to an analytical solution for the demagnetization energy, in practice the integrals cannot typically be solved analytically and alternative methods are employed. Other approaches include fast Fourier transform (FFT), fast multipole and non-unform grid interpolation.

2.6.1.2. *Fast convolution.* A widely used technique, fast convolution is advantageous in terms of computational resources and time. This approach is based on recognizing the fact that the demagnetizing field due to a continuous magnetization distribution can be represented as a convolution operation, the convolution of $\tilde{N}$ and $\mathbf{M}$. The expression for $\mathbf{H}_d$ is [58]

$$\mathbf{H}_d(\mathbf{r}) = -\int \tilde{N}(\mathbf{r}-\mathbf{r}')\mathbf{M}(\mathbf{r}')d^3r', \tag{2.34}$$

where the integral is performed over the full ferromagnetic volume and the demagnetization tensor, $\tilde{N}(\mathbf{r}-\mathbf{r}') = -\frac{1}{4\pi}\nabla\nabla' G(\mathbf{r},\mathbf{r}')$, is defined in terms of the Green's function, $G(\mathbf{r},\mathbf{r}') = \frac{1}{|\mathbf{r}-\mathbf{r}'|}$.

In the continuum approximation, the magnetization of each cell can be considered as a source for the demagnetizing field at an arbitrary cell. Let the index $\mathbf{i} = (i_x, i_y, i_z)$ represent the i-th cell along the x, y, z directions of the three-dimensional mesh, with magnetization $M_\mathbf{i}$. The demagnetizing field at cell $\mathbf{i}$ can be written as [48]:

$$\mathbf{H}_{d\mathbf{i}} = -\sum_{\mathbf{j}} \tilde{N}(\mathbf{r_i}-\mathbf{r_j})\mathbf{M_j}, \tag{2.35}$$

where the sum is over all cells including $\mathbf{i}$ and the demagnetizing tensor is [48]:

$$\tilde{N}(\mathbf{r_i} - \mathbf{r_j}) = \frac{1}{V_\mathbf{i}} \int_{S_i} \int_{S_j} G(\mathbf{i}, \mathbf{j}) dS_i dS_j, \tag{2.36}$$

where $V_\mathbf{i}$ and S_i are the volume and surface of cell $\mathbf{i}$ respectively. The total demagnetization energy E_d can be written as:

$$E_d = -\frac{\mu_o}{2} \sum_\mathbf{i} \mathbf{M_i} \cdot \mathbf{H}_{d\mathbf{i}} V_\mathbf{i} = \frac{\mu_o}{2} \sum_{\mathbf{i},\mathbf{j}} \left[\mathbf{M_i} \cdot \tilde{N}(\mathbf{r_i} - \mathbf{r_j}) \cdot \mathbf{M_j} \right] V_\mathbf{i}. \tag{2.37}$$

Note that the demagnetizing tensor only depends on the vector connecting the center of the source and target cells and only needs to be computed once. Once $\tilde{N}(\mathbf{r_i} - \mathbf{r_j})$ is known, the demagnetizing field can be obtained using a discrete convolution of $\mathbf{M}$ and $\tilde{N}$. A convolution operation in the spatial domain is equivalent to a point-wise multiplication in Fourier space, which is often used in practice to save time. For more details on the fast convolution technique see references [58, 59].

2.6.2. Determination of the equilibrium magnetization distribution

Most solvers use either a static or dynamic methods to find the equilibrium magnetization distribution. Static methods are convenient when one is only interested in finding the local minima of the energy. The spins in each cell of the material are allowed to rotate gradually towards the direction of $\mathbf{H}_{eff}$. This process decreases the energy of the system for each iteration and is repeated until the maximum angle between the magnetization and the effective field is smaller than a specified tolerance. Some of the numerical techniques used in this approach include the Conjugate Gradient Steepest Descent and Gauss-Seidel methods.

In the dynamic approach, the LLG equation is integrated subject to a user-specified initial state $\mathbf{M}(t = 0) = \mathbf{M}_o$, including saturated, completely random, or user-designed

states that are close to the sough-after configurations are typical initial configurations. The magnetization state is updated after each time step and the process continues until the total simulation time reaches a user-specified value.

The methods used to integrate the LLG equation are commonly classified in explicit and implicit methods. Explicit methods calculate the magnetization at a later time by using only the magnetization at the current time, while implicit methods require both the magnetization at the current and at a later time.

Explicit methods can achieve high accuracy however a stable solution cannot be obtained in all cases unless the time steps are sufficiently small. They are frequently used in systems where the exchange coupling is weak. Commonly used explicit methods include Runge-Kutta of different orders. Implicit methods are more stable but also more difficult to implement and do not preserve the amplitude of magnetization in the limit of small damping, which is one fundamental requirement of the micromagnetic model. Some of the techniques used include predictor-corrector algorithms. For the present work only explicit methods were used.

2.7. Summary

In summary, the micromagnetic model and the LLG equation provide the theoretical framework to predict the dynamic behaviour of ferromagnets, however the mathematical complexity involved makes analytical solutions impractical for all but the simplest cases and a computational approaches are commonly used instead. Except for the magnetocrystalline anisotropy, all the energy terms presented in the previous sections were considered to calculate the effective field, spin distributions, and dynamics. Details on the different

micromagnetic solvers and experimental techniques used in this work will be discussed in the next chapter.

CHAPTER 3

Methods

In this thesis, a combination of micromagnetic simulations and experimental techniques to study static and dynamic properties of magnetic vortices and AVs. The main approaches used for this work, numerical and experimental, are described in this chapter. The micromagnetic simulations were performed using two free and open-source software packages. A general description of these solvers as well as general considerations regarding the procedure to set up the micromagnetic simulations are discussed in the first section of this chapter. Section 3.4 provides details on two experimental characterization techniques, Magnetic Force Microscopy (MFM) and magneto-optical Kerr effect (MOKE), that were used for part of the work presented in this thesis.

3.1. Micromagnetic Simulations

3.1.1. Micromagnetic solvers

Micromagnetic simulations are a powerful set of tools that can help to expand our understanding in a variety of magnetization processes at the nano- and microscale. With the rapid advances in numerical algorithms and the availability of more powerful computers, the bridge between experiments and micromagnetic simulations is narrowing quickly and more realistic results are obtained with modern software packages.

In this work two different micromagnetic solvers were used, the Object Oriented Micromagnetic Framework (OOMMF) [60] developed by the National Institute of Standards

and Technology and MuMax^3 [61], developed by the DyNaMat group at Ghent University. An important difference between these solvers is that OOMMF uses a central processing unit (CPU) to perform the calculations, while MuMax^3 is designed to use a graphical processing unit (GPU), which makes it run comparatively much faster and allows us to tackle larger problems. On the other hand, both solvers use a finite differences approach to solve dynamic simulations, using rectangular cells, and include energy minimization routines; also both allow 3-D and multilayer simulations, and include extensions for spin torque and Dzyaloshinskii-Moriya interaction. Although these solvers use different programming languages, the output spin distribution files are binary files with a format that is compatible between both packages.

3.1.1.1. *OOMMF environment.* OOMMF is a modular, object oriented micromagnetic solver that uses a finite differences method to solve the LLG equation. It is widely used and has been tested thoroughly by the scientific community in a multitude of scenarios. The source code, written in C++, can be accessed and modified, and new, user-defined modules can be added in order to adapt the software to the particular needs of the user. A top level menu is used to open individual modules, via network sockets, which include a problem editor, several graphical display modules, a 2-D and a 3-D extensible solver, and saving modules. The graphical interfaces for some of these modules are shown in figure 3.1.

Typically simulations are defined using input scripts (*.mif files) written in Tool Commanding Language (Tcl). These scripts specify the simulation parameters such as material type, geometry, external field, current, etc. can be loaded and executed at run time in some of the modules. Example scripts can be found in appendix.

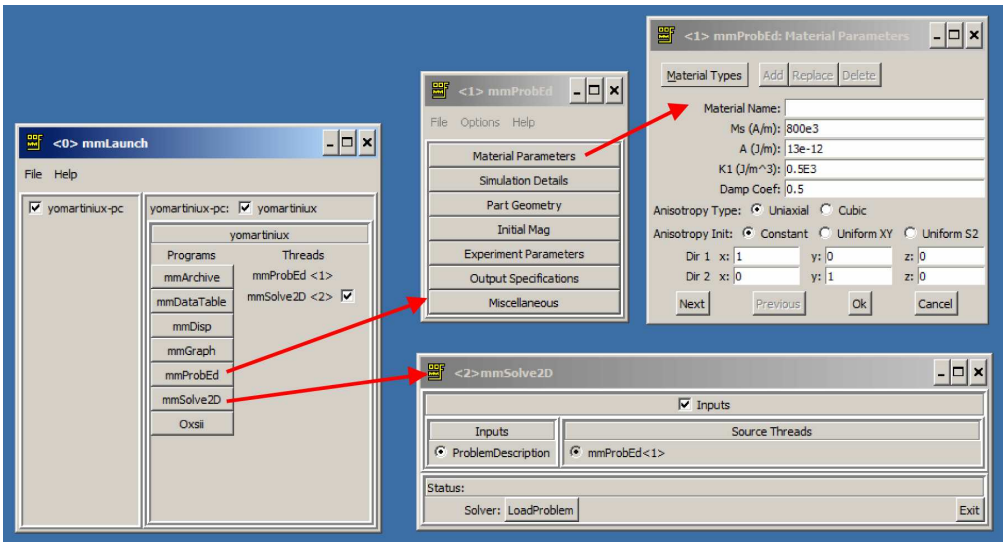

Figure 3.1. Graphical interface of an instance of OOMMF running in Windows operating system.

3.1.1.2. *MuMax*^{3} *environment.* MuMax^3 is also based on the finite differences method to solve the LLG equation. Its main advantage is that it runs the numerical calculations on GPU, which due to their high number of cores can achieve speed-ups of up to 100x compared to traditional simulations based on CPU. Simulation parameters are specified via a script (*.txt file) that uses a syntax that is a subset of Go programming language. During execution, a web graphical user interface (GUI) can be accessed through an internet protocol (IP) address to visualize the progress of the simulation. Figure 3.2 shows an instance of a MuMax^3 script being executed in the command line (left) and the corresponding web GUI (right) in a Linux operating system.

For this work MuMax^3 was executed on a GeForce® GTX NVIDIA® Titan, Black edition GPU with 2880 cores and 6 GB standard memory installed on a personal computer with an Intel® Core™ i7-4771 (8MB, 3.5GHz) Quad Core processor, 2×8GB Ram memory cards, and AsusZ87-A motherboard on a Linux operating system.

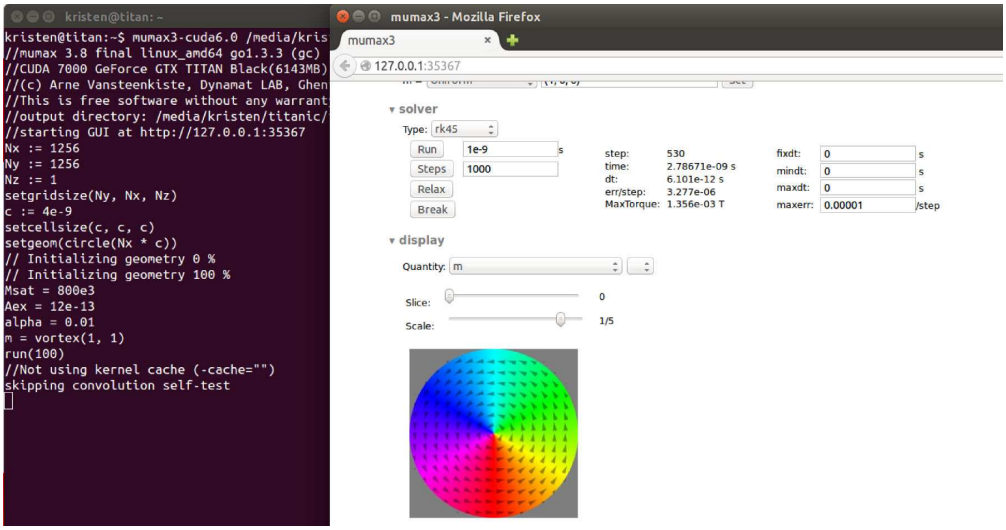

Figure 3.2. MuMax^3 script being executed via the command line (left) and corresponding web GUI (right) running on a Linux operating system.

3.2. Simulation types

The different simulations presented here were initially performed using OOMMF, in particular those related with the interaction of magnetic vortices (see Chapter 6). Once MuMax^3 became available and after some tests we incorporated it as a main tool due to its high efficiency for handling larger simulations. The simulations regarding AV formation (see Chapter 4) incorporate results from both solver, while the results for the dynamics of AV (see Chapter 5) were obtained using MuMax^3. Regardless of the particular micromagnetic solver used, the simulations results fall into three different categories that are presented in the next subsections: equilibrium configuration, hysteresis loops and normal modes.

3.2.1. Equilibrium configurations

An equilibrium configuration is a state where the energy is a minimum. Since this minimum could be local instead of global a system might have, in general, several equilibrium configurations. If the system is in an equilibrium configuration with a local energy minimum,

a small perturbation can increase the energy the system but it will eventually return to its initial state however if the perturbation is large enough the system might evolve towards a different equilibrium configuration. Fig. 3.3 illustrates some of the common equilibrium configurations found at zero field for a rectangular thin-film element [62]. The C and S states are quasi-homogeneous states that are characterized by a large average magnetization along the long axis. Flux closure states such as the Landau and cross-tie states have lower average magnetization and are regarded as low remanence states. Vortices and AV appear naturally in some of these states, for instance a vortex-AV-vortex configuration is found along the axial line of the cross-tie domain wall.

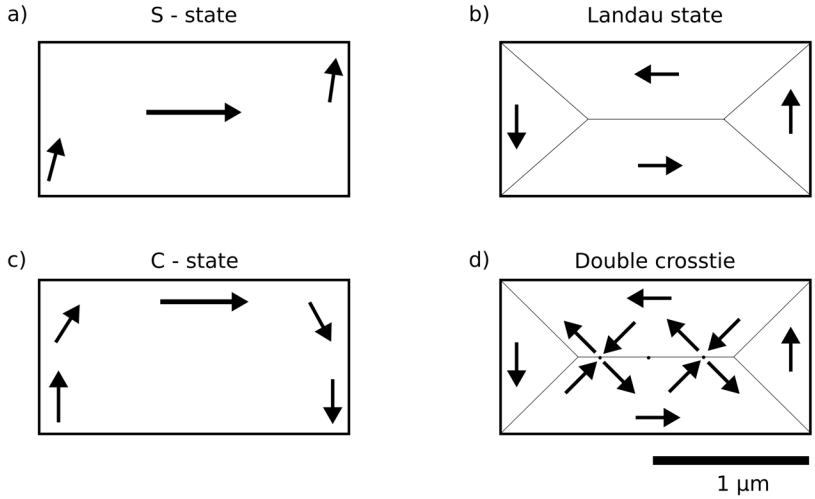

Figure 3.3. Illustration of some of the common equilibrium configurations in a rectangular thin film element.

In a static approach, energy minimization routines can be used to determine the equilibrium configuration of a system. Given an initial spin distribution the energy is compared to that obtained for a configuration with similar spins distribution except for a small deviation or rotation. Since for an equilibrium configuration the magnetization is parallel to the local effective magnetic field and the torque $\tau = \mathbf{m} \times \mathbf{H}_{eff}$ vanishes everywhere in the magnetic structure, either the angle or the torque can be used as reference or control parameters.

Consider the case of the torque for example, the solver evaluates the torque in each cell τ_i and considers that the state is at equilibrium when this value is below a certain threshold,

$$|\tau_i| \leq \tau_{max}, \tag{3.1}$$

where τ_{max} represents the maximum torque and typical values of $\sim 1 \times 10^{-5}\ M_s$ are used.

Alternatively, in a dynamic approach the system is allowed to evolve in time until eventually reaches equilibrium under dissipative effects. To speed this process up, usually a large damping constant ($\alpha = 1$) is chosen so that there is minimal precession and the system converges rapidly towards equilibrium.

In the present work, both approaches were used. The results obtained with MuMax[3] are based on the static approach, while for the results obtained with OOMMF, a dynamic approach was used instead. The spin textures of interest included vortices, AV, and mainly saturated configurations. In the case of vortices, since the shapes used were circular disks for which the vortex was the ground state, the vortices formed easily even when starting from a random magnetization. In contrast, a careful optimization of the shape anisotropy and field-treatment was needed to promote the formation of the AV state.

3.2.2. Hysteresis Loops

Hysteresis refers to the fact that the response of the magnetization to an external magnetic field depends on the previous history of the material.

To simulate a hysteresis loop or reversal process, an initial magnetic field is stepped in small increments and the average magnetization (all components) and the magnetization distributions are recorded after once equilibrium is reached at each step. Usually an initial

magnetic field that is large enough to saturate the sample is chosen. Subsequently the field is decreased until the system reaches saturation in the reverse direction. The process is then repeated in the opposite direction until the field reaches the initial saturating value.

Depending on the sample size, it may take several days to complete a full loop. However reducing the number of cells of the sample allows us to obtain a quick estimate of some of the relevant values such as the coercive field. Better accuracy can be obtained with further refining the mesh or by combining it with other strategies such as running very coarse loop to get rough estimates of the saturation field and any transitional regions. Once these regions are known, a variable field step can be used, where a large field step is selected for regions that do not change much and finer steps are used near the transitional regions.

3.2.3. Normal modes

The normal modes of a magnetic structure are independent patterns of motion, in which all the parts of the system oscillate harmonically with the same frequency (known as the normal mode frequency). If the response of a micromagnetic system to an external excitation is such that the deviation of the spins from equilibrium is small then the magnetization dynamics can be described as the superposition of normal modes. Interpreting results in the context of normal modes can be especially helpful when the temporal behavior is complex.

In this work the dynamics of systems of coupled vortices and isolated AV were studied and the results were analyzed in the context of the normal modes of the structures. In order to obtain the normal modes a spectral mapping technique [63, 64] was used, which is illustrated in figure 3.4.

This technique uses Fourier transformations to obtain the frequency-domain spectrum of the magnetization for each individual cell. Then this information can be converted into a set

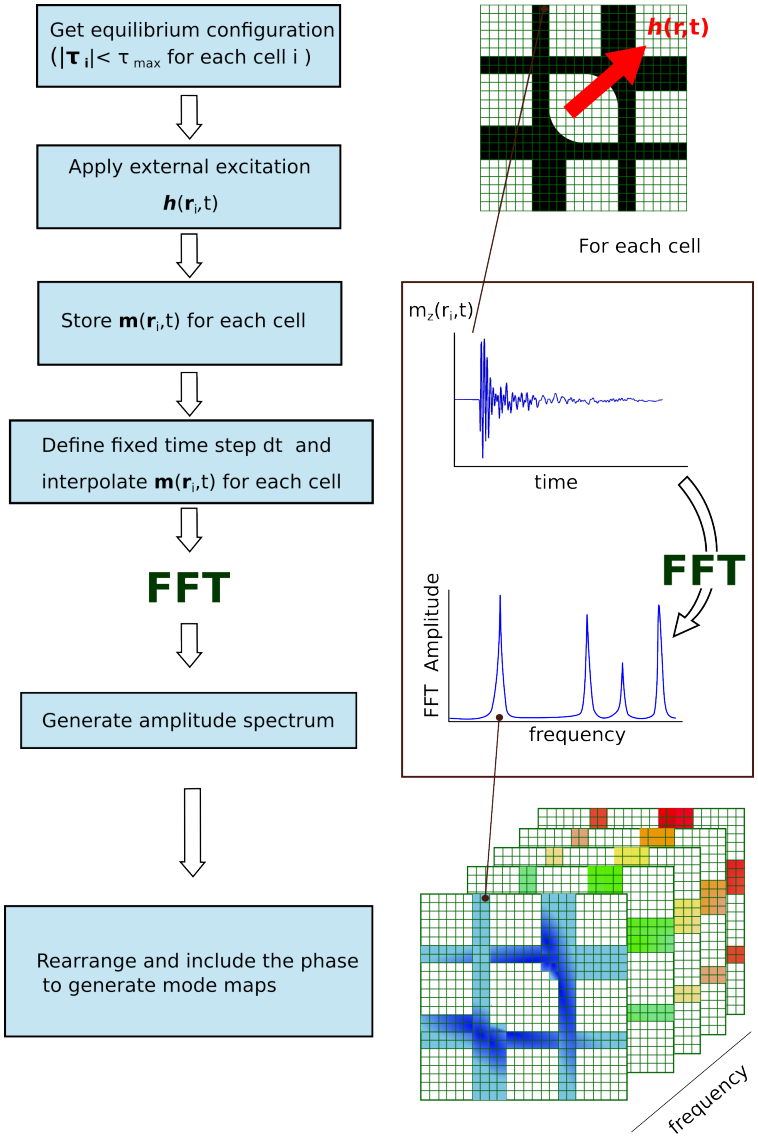

Figure 3.4. Diagram illustrating the micromagnetic spectral mapping technique.

of "mode maps" or spatial distributions of the Fourier amplitude and phase for each resonance frequency. Often this information (amplitude and phase is) is used to display snapshots of the normal modes at an instant of time and they can be used to create animations of each mode. The basic procedure to obtain the mode map is as follows:

(1) First, the magnetic structure of interest is relaxed to an equilibrium spin configuration either using energy minimization or a dynamic approach with large damping.

(2) Next, the structure is perturbed from equilibrium using an external excitation that can be, for example, a magnetic field pulse. All three components of the magnetization are recorded at each cell over a finite period of time and using a realistic damping constant.

(3) Once the simulations are finished, a post-processing analysis of the results is performed using an in-house-developed matlab code: A FFT is applied to the time series of the OOP component of the magnetization $M_z(t)_i$ of each individual cell obtaining a frequency spectrum for all cells. The reason why only M_z is considered is because the samples are magnetized IP, therefore this component should be sufficient to show the normal mode patterns.

3.2.3.1. *Spectra.* Given a time series, the corresponding frequency spectrum can be obtained by applying a discrete Fourier transform. One of the first considerations when doing this transformation is whether the time-domain series should include just the average magnetization (over the full sample or any subregion) or the magnetization of individual cells instead. In the first case, some information may be lost because of the spatial averaging. For example, for a mode that has even symmetry the M_z component will average to zero at all times and therefore its corresponding Fourier amplitude will also vanish. In the second case the individual spectra of the Fourier amplitude as a function of frequency for each cell are obtained and all modes within the spatial resolution of the simulation are captured (at least all of the modes that are excited by a particular choice of field). This was the technique adopted for the work presented in this thesis.

Some of the relevant parameters and considerations for the Fourier transform are as follows:

(1) Time step (dt). The default option in the micromagnetic simulation software is to use an adaptive time step (Δt) to run the simulation more efficiently in terms of computational time and memory, however FFT algorithm requires a fixed time step. To address this the raw simulation output magnetizations were interpolated using a fixed time step dt.

(2) Sampling frequency (f_s): Also known as sampling rate, it is defined as the number of data points collected over a given period of time. It is given by $f_s = \frac{1}{dt}$.

(3) Nyquist frequency (f_N): Is the maximum frequency that can be recovered at a given sampling rate and it is given by $f_N = \frac{f_s}{2} = \frac{1}{2dt}$. Choosing a small value for dt during the interpolation is therefore necessary to preserve high frequencies. In the present work, dt was typically chosen to be 10 ps, which is larger than the typical adaptive time step (<0.1 ps) and, in principle allows one to observe frequencies of up to 50 GHz.

(4) Number of Fourier points (N_{fft}): Number of points that the Fourier transform will produce. N_{fft} must be greater than or equal to the number of points of the (interpolated) time series. If N_{fft} is larger than the number of points in the time series, then the latter is padded with trailing zeros. Since the maximum frequency is already set by the Nyquist frequency, increasing N_{fft} leads to a more closely spaced points in the frequency domain. In the present work the FFT algorithm was used. This algorithm is more efficient when the number of points is set to a power of two hence and N_{fft} was generally set to the next power of two from the number of points in the time series.

3.2.3.2. *Mode maps.* The relative intensity of the peaks in the frequency spectrum shows which modes will be excited more efficiently and can therefore be used as a guide to pre-select specific frequencies for generating the corresponding mode maps. After selecting a particular frequency then, the mode maps, typically represented using $Acos\phi$ for each cell, are plotted. Performing Fourier analysis on the $M_z(t)$ not only provides an accurate picture of the magnetization dynamics for an IP magnetized structure but this is also the component of the magnetization that is the most important for experiments such as BLS, where the intensity of the light scattered by SW is proportional to the A^2 where A is the Fourier amplitude of the OOP component.

3.2.4. Important considerations

Micromagnetic simulations are a valuable tool, however, the parameters must be chosen carefully in order to yield accurate results. Parameters that are particularly important are the cell size and maximum torque. The cell size is usually chosen such that its length is small compared to the exchange length of the material so that the assumption that the magnetization is uniform in each cell is valid. As a general rule the smaller the cells the more accurate the results are, however the price to pay is that this increases the total number of cells (typical simulations can have millions of cells), which in turn demands more computer memory and could make the simulation impractically long. A balance between accurate but reasonably fast simulations is usually achieved by carrying out cell size dependent tests, where the same simulation is run using progressively smaller cell sizes until the results converge below a critical size, which can be taken as the maximum recommended cell size for that simulation. Even if the computer capabilities allow very small cell sizes, it must be noted

that the micromagnetic framework is a continuum mesoscopic model so it is not sensible extend the model to the atomic scale.

The time is discretized into several points with step size h. In general, the time step h is preferably chosen such that it is much smaller than $\frac{2\pi}{\omega_o}$, where ω_o is the Larmor precession frequency for a particular cell. The smallest time step for the simulation is set by cells with highest effective fields and therefore highest Larmor frequencies. These cells are usually located at the boundaries and do not contribute much to the dynamic response. Mumax[3] also implements adaptive time step so that in each iteration the maximum error of cells is below a preset value.

Although the present thesis is focused mainly on the results obtained using micromagnetic simulations. There were experimental techniques that were used to measure the hysteresis loops and also the spin distribution.

3.3. Material parameters

The material chosen for the present work, Permalloy ($Ni_{80}Fe_{20}$), is a soft ferromagnetic material. For the simulations, the material parameters used were exchange stiffness constant, $A = 1.3\times10^{-11}$ J/m, saturation magnetization, $M_s = 8.6\times10^5$ A/m, (for vortex simulations) and $M_s = 8.0 \times 10^5$ A/m (for AV simulations), gyromagnetic ratio, $\gamma = 1.76 \times 10^{11}$ $s^{-1}T^{-1}$, magnetocrystalline anisotropy was neglected, and damping constant, α=0.01 (for dynamics) and α=0.1-1 (for non-dynamic simulations). Both M_s values are within the range that is typical for Permalloy. The values correspond to choices that were made to match materials for two different projects, are not related to the spin configuration, and have no effect on

the main conclusions of this thesis. The cell size was chosen as 4×4 nm^2 unless specified otherwise.

3.4. Experimental techniques

Two experimental techniques, MFM and MOKE, were used to obtain images and hysteresis loops of the samples containing AVs and are discussed in the following subsections.

3.4.1. Magneto Optical Kerr Effect (MOKE)

When linearly polarized light is reflected from a magnetic surface the reflected beam becomes elliptically polarized with the polarization rotated over a small angle θ_K, an effect known as the magneto-optical Kerr effect. Since the penetration depth of light is usually just a few tens of nanometers, MOKE is a useful tool to study surface magnetism and it is widely used in the study of magnetic thin films. Three distinct configurations are conventionally defined based on the direction of the magnetization and the plane of incidence (3.5): a) longitudinal, b) transverse, and c) polar MOKE as shown in figure 3.5. For the present work, longitudinal MOKE configuration was used.

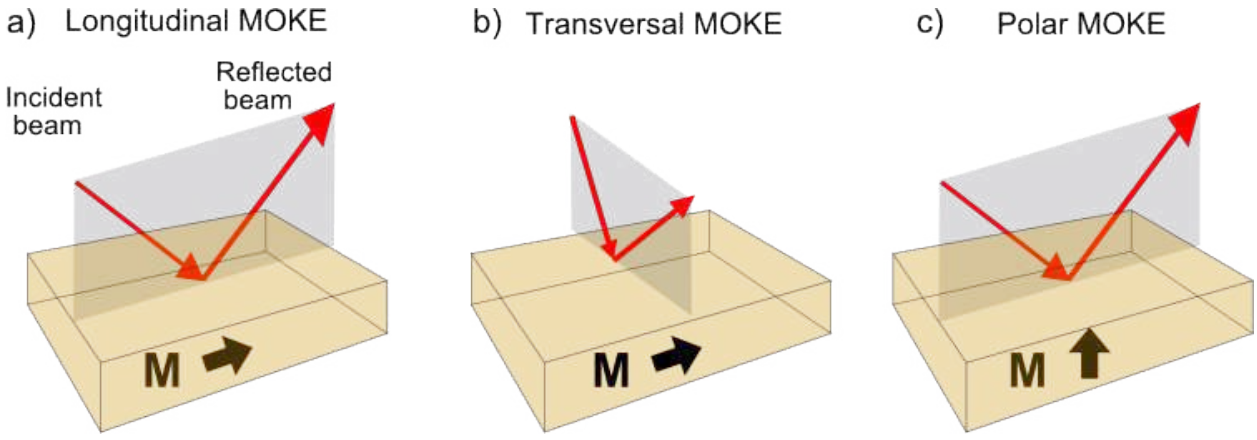

Figure 3.5. Schematic of the a) longitudinal, b) transverse, and c) polar MOKE configurations. Red arrows indicate the direction of the incident and reflected light while black arrows indicate the direction of the magnetization M.

This effect has a quantum mechanical origin, however it is usually described classically in terms of the dielectric tensor. Consider a linearly polarized beam propagating towards a magnetic material. Linearly polarized light can be thought of as the superposition of left- and right-circularly polarized light. The electrical field of the incoming beam causes the electrons within the material to move. The characteristics of this response are described by the dielectric tensor. In the absence of a magnetic field, a right-circularly polarized (RCP) electric field will make the electrons move into a right-circular orbit, and similarly left-circularly polarized (LCP) electric field will lead to a left-circular motion. The electric dipole moment is proportional to the radius of these trajectories, which in this case is the same regardless of the polarization of the electric field, therefore the elements of the dielectric tensor are the same and no Kerr rotation is expected. However, if an external magnetic field (or the magnetic field due to the magnetization of the material) is applied parallel to the propagation of the beam, the electrons then experience a Lorentz force $\vec{F}_L = q\vec{v} \times \vec{B}$ that selectively reduces (increases) the radius of the circular trajectories for a RCP (LCP) electric field. This difference in radii adds non-zero off-diagonal components to the dielectric tensor.

Although a detailed quantum mechanical description is beyond the scope of this work, it is worth mentioning that the motion of the electron is coupled to its spin via the spin-orbit interaction. For magnetic materials, the unbalanced population of spin-up and spin-down electrons enhance the Kerr rotation. For more information, refer to Ref. [65]. MOKE can probe the magnetization in small regions but the ultimate spatial resolution is restricted by the diffraction limit of light, which is about 200 nm. Therefore it is especially convenient when investigating small patterned structures such as wires, dots, etc.

In this work MOKE measurements were performed using a home-built magnetometer (see appendix B) to study the hysteretic response of arrays of patterned structures. The equipment had a plastic enclosure to minimize air currents and a diode laser with a wavelength of 632 nm. A bi-polar power supply and a computer interface allowed precise control of the applied magnetic field. A Stanford Research System SR830 DSP Lock-In Amplifier was used to improve the signal to noise ratio.

3.4.2. Magnetic Force Microscopy (MFM)

Magnetic force microscopy is a non-contact technique used for imaging magnetization patterns. Usually an atomic force microscope (AFM) is used, including a small cantilever with a sharp tip fixed to its free end. For MFM measurements the tip is covered with a relatively thick (about 40 nm) coat of magnetic material. Typical lateral resolution is on the order of 50 nm and specially designed equipment can possibly obtain 10-20 nm. In order to gain information about the local orientation of the magnetization in the sample, the tip is brought to a distance of $\sim$100 nm from the sample surface. The distance is chosen so that it is close enough that the magnetic forces are significant but far enough away that the atomic forces are minimized. An illustration of MFM is shown in figure 3.6.

For the experiments presented in this thesis, the measurements were done using a dynamic mode where the cantilever is sinusoidally excited at its clamped end with amplitude A and frequency $\omega_o = \sqrt{k/m}$ where k and m are the spring constant and the effective mass of the probe respectively. The tip also oscillates sinusoidally with amplitude a and it is phase-shifted with respect to the driving signal. The separation between the tip and the sample d_o is made small enough that the motion of the cantilever is affected by a force $\mathbf{F}$, with a vertical component F_z. This force accounts for the static and dynamic interactions and is, in

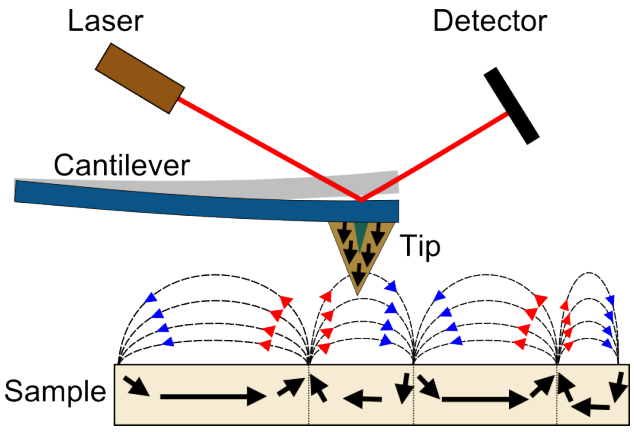

Figure 3.6. Schematic of the magnetic force microscopy measurement. The black arrows represent the direction of magnetization. Dotted lines represent the stray field caused by the magnetization of the sample. The vibrations of the magnetic tip, which are monitored using a laser and detector, are affected by the stray fields of the sample.

general, of non-linear nature however in the low amplitude limit ($a \ll d_o$), the tip detects the vertical gradient of the vertical component of the force $\partial F_z/\partial z$. In this case the cantilever can be modelled as forced oscillator with a modified spring constant $k' = k - \partial F_z/\partial z$ and resonant frequency $\omega = \omega_o\sqrt{k'/k}$ such that a shift in resonant frequency is given by:

$$\Delta\omega = \omega - \omega_o = \omega_o(1 - \sqrt{1 - \frac{1}{k}\frac{\partial F_z}{\partial z}}), \tag{3.2}$$

and will cause a change in the oscillation amplitude as well as a phase shift, so measurements of those quantities can be used to obtain the lateral variation of $\partial F_z/\partial z$. Since MFM measures the stray field and hence is not a direct measure of the magnetization, interpretation of the MFM contrast is not straightforward and requires careful consideration. The force $\mathbf{F}$ can be expressed as:

$$\mathbf{F} = \nabla(\mathbf{m} \cdot \mathbf{B}), \tag{3.3}$$

where $\mathbf{B}$ is the stray field of the sample and $\mathbf{m}$ is the magnetic dipole moment of the tip. Since the magnetization of the tip is constant, and directed along the out-of-plane (z) direction, MFM is only sensitive to the z component of the out-of-plane field.

In this chapter, the methods used for simulations, MOKE, and MFM have been described and in the subsequent chapters they will be applied to study magnetic vortex and AV textures. The formation process of magnetic AVs is discussed first, where MOKE and MFM measurements were used to investigate the effect of shape anisotropy on the AV formation rate and micromagnetic simulations were used to study the hysteresis process and gain more insight about the reversal mechanism. The dynamic response of AVs to different excitation fields was also explored by using micromagnetic simulations. Finally, the magnetostatic coupling of interacting vortices is investigated using micromagnetic simulations.

CHAPTER 4

Antivortex Formation

4.1. Introduction

In recent years, magnetic vortices have attracted great interest, propelled in part by the recognition that vortices form naturally, as the ground state, in a variety of submicron patterned elements, such as disks, [66, 67] ellipses, [68] triangles, [69] squares, and rectangular nanodots [70] made of soft ferromagnetic materials. However, despite the extensive research that has been conducted on vortices, AVs have not been studied as intensively and only a comparatively small number of experiments have been done so far to study magnetic AVs. The unique properties of an AV might offer important advantages over its vortex counterpart, for example its particular spin distribution offers a natural path to channel spinwaves along different directions, however formation of isolated stable AVs is rather difficult and general guidelines on how to optimize the formation rate are highly valuable. In this chapter, the effects of field history and structure shape on the formation of magnetic AVs are discussed. In a previous report [71], our research group has proposed a simple procedure to nucleate AVs in pound-key-like structures. Here, I expand this work to investigate the role of shape anisotropy on the formation rate by using experimental techniques and micromagnetic simulations. The results presented in the remaining sections of this chapter have been published in reference [22]. The reversal process was investigated for a series of patterned micron-sized permalloy pound-key structures with varying degrees of asymmetry using micromagnetic simulations and the role of the shape anisotropy was investigated using MOKE hysteresis combined with MFM measurements. I was responsible for all of the micromagnetic simulations and the analysis; the experimental measurements were done with the help

of other members of our research group. Brian Shaw made some of the MFM measurements and Lin Li collected most of the MOKE hysteresis data presented here. I also made some of the MFM measurements and participated in the calibration and optimization of the MOKE equipment as well as preliminary MOKE data collection.

Magnetic AVs are commonly observed in conjunction with vortices as part of a cross-tie domain wall [72, 73], however, unlike magnetic vortices that form easily in sub-micron elements, individual AVs are rather elusive. This can be explained in terms of the magnetic flux lines associated to the particular spin distribution of the AV and its higher energetic cost as compared to the vortex. As illustrated in Fig. 4.1, the flux lines of a vortex in a disk form closed loops that channel the flux entirely within the disk and reduce the magnetostatic energy to zero. In contrast, an AV state in a circular disk (Fig 4.1b) will produce stray fields that increase the magnetostatic energy. The AV hence tends to be a metastable state. In the disk geometry, for example, the AV is unstable and generally some effort needs to be made to channel the flux in order to make it a metastable state.

Because AVs are metastable states, there are few experimental reports on the formation and stabilization of isolated AVs that are not coupled to nearby vortices or AVs [74, 75, 14, 73]. Investigation of the physical properties of magnetic AVs depends upon reliable procedures and geometries to create stable, isolated AVs. Since AVs are metastable states, this task involves a careful design of the host magnetic structure as well as post-fabrication magnetic field treatments. The strategies to isolate AVs include the use of patterned structures with clover-shaped [73] and infinity-shaped [14] geometries (Fig. 4.2a and 4.2b respectively).

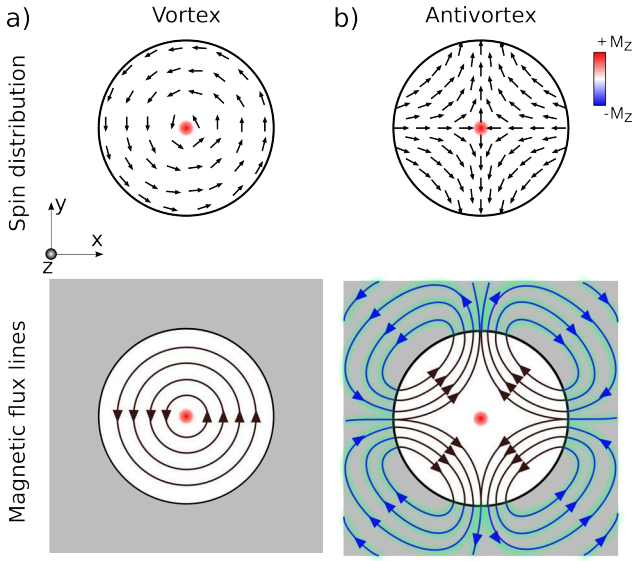

Figure 4.1. Spin distribution (top) and magnetic flux lines (bottom) of a vortex and a AV in a circular disk are shown in a) and b) respectively. Flux closure of a vortex produce no stray field while open flux lines of the AV create significant stray fields outside the disk, which increases the magnetostatic energy and makes it energetically less favorable

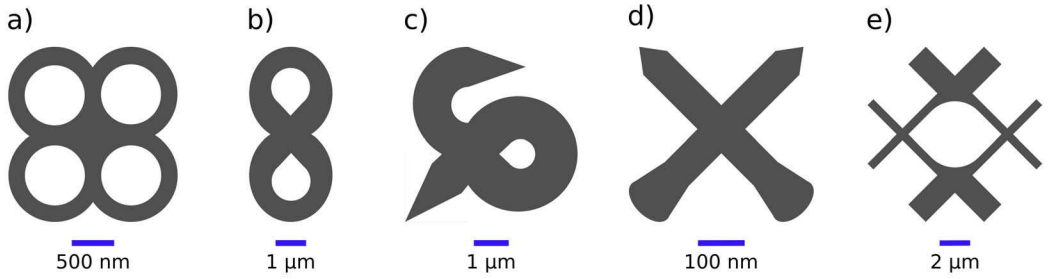

Figure 4.2. Geometries that have been used previously by other authors to stabilize a magnetic AV: (a) clover (b) infinity, (c) ϕ-shape, (d) cross-like, and (e) the pound-key shape used for this work. Thicknesses are in the 30-50 nm range for all the structures.

The loops used in this approach promote flux closure, improving stability by minimizing stray fields, however reliable formation can be problematic. Another strategy include formation via controlled domain wall nucleation and propagation, in ϕ-shaped structures [74] (Fig. 4.2c), which provides reliable results but the field treatment requires either a rotating magnetic field or a rotation stage. The use of shape anisotropy to selectively reverse certain regions of an asymmetric cross structure [75] (Fig. 4.2d) or a pound-key-like structure [71]

(Fig. 4.2e) has also been reported to assist the AV formation. This strategy only requires a simple one-component field treatment and is followed in the present work for the latter geometry. In particular, the role of structure shape and field treatment on the formation of AVs is addressed.

In [71], it was shown that a two-step field treatment can be used to promote the formation of AVs where the first field H_1 is large enough to saturate the sample along the diagonal of the structure and the second field H_2, applied antiparallel to the first, promotes reversal of the central and fatter-leg regions causing AVs to form at the two intersections along the diagonal that is perpendicular to the direction of the magnetic field. Micromagnetic simulations used in the present work indicate that the value of the coercive field H_c corresponds to the nucleation field for Permalloy and therefore provides a practical value for H_2. These results of the field treatment were tested using MOKE to measure hysteresis and MFM for imaging and allowed us to explore the effects of the geometrical parameters on the formation and stabilization of AVs in those structures in more detail.

4.2. Methods

The previous work in [71] looked at two specific structure designs and sizes. Here we looked at additional designs and sizes. Square arrays ($250\times$ 250 μm^2) of patterned structures with widths ranging from 8 to 16 μm and thickness of 37 nm were fabricated on a Si wafer by standard e-beam lithography, magnetron sputtering, and lift-off. Samples with circular and square central regions were considered. The curvature of the circular region provides a smooth and gradual change of direction of the spins and the curvature of the surface is expected to help to guide the reversal process, while rectangular shapes require a more drastic

change of direction especially near the intersection, however, they allow a simple comparison between the aspect ratios, and hence the shape anisotropy, of the central region and the outer legs. SEM images of the different shapes considered are presented in Figure 4.3a-d as well as the parameters used to characterize their dimensions (Figure 4.3e). The structures with a square central region, were designated as AV-S and structures with a circular central region, as AV-C.

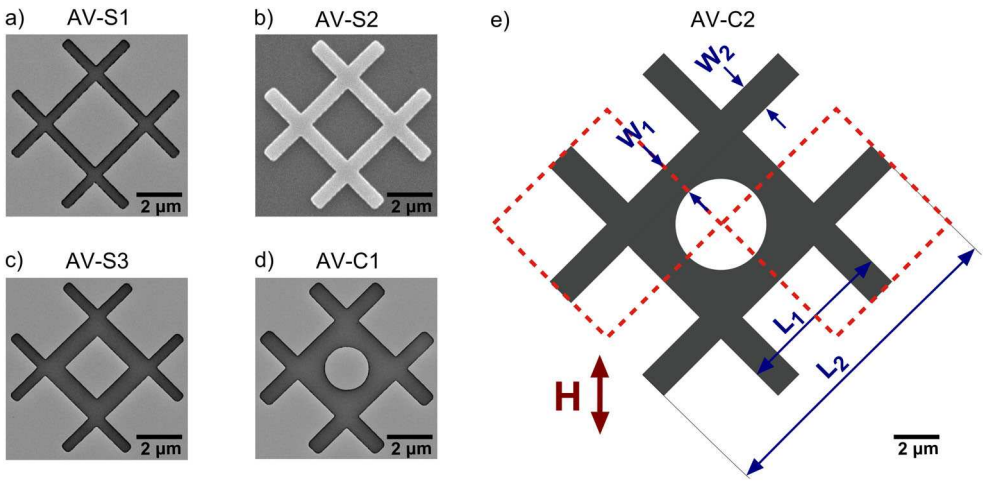

Figure 4.3. Scanning electron microscope images (a-d) and diagram (e) of structures used to stabilize magnetic AV. Structures can be grouped depending if they have a square central region (AV-S) or a circular central region (AV-C). The external magnetic field H is applied along the structure diagonal, as indicated by the double-headed red arrow, and the square areas enclosed by the dashed lines highlights the intersections where AVs are expected to form.

The values of the key structure dimensions are summarized in table 4.1 for each sample. AV-S structures with central/outer leg width ratios, w_1/w_2, of either 1 or 2 were used (table 4.1). Two of the AV-S samples (AV-S1 and AV-S2) have $w_1/w_2 = 1$, but since the central connectors in AV-S1 are more elongated as compared to AV-S2, the shape anisotropies are different. Sample AV-S3 allows us to test an even more pronounced difference in shape anisotropy since $w_1/w_2 = 2$. The AV-C structures, AV-C1 and AV-C2, differ both in overall size L_2 as well as in their relative leg widths ratio w_1/w_2.

4.2.1. Experimental methods

MOKE hysteresis measurements were made on each of the samples to study the reversal process of the different arrays and to evaluate important physical quantities such as the coercive field, nucleation and annihilation fields of the AVs.

Sample	w_1 (μm)	w_2 (μm)	L_1 (μm)	L_2 (μm)	w_1/w_2
AV-S1	0.50	0.50	4.0	8.0	1.00
AV-S2	0.75	0.75	4.0	8.0	1.00
AV-S3	1.00	0.50	4.0	8.0	2.00
AV-C1	1.00	0.75	4.0	8.0	1.33
AV-C2	1.75	1.50	8.0	16.0	1.17

Table 4.1. Dimensions of the AV-S and AV-C samples. w_1, w_2, L_1, L_2 represent the widths of the central leg, internal leg, central region and total width respectively. Last column provide central/outer leg ratio

The longitudinal MOKE configuration with linearly s-polarized (i.e., with electric field oscillating perpendicular to the plane of incidence) light and an angle of incidence of 45° was used in all measurements. The laser beam was focused down to a spot size of approximately 160 μm, as estimated from knife-edge measurements (see Appendix for more details). A static magnetic field H, parallel to the plane of incidence (Fig. 3.5), was applied in-plane along the diagonal of the pound-key structures, as indicated by the double-head red arrow in figure 4.3e. This allows us to measure the component of the magnetization along the direction of H. Hysteresis curves were measured by monitoring the rotation of the polarization Θ_k as a function of H.

In order to verify the formation of AVs states after the magnetization process, imaging was conducted using MFM. A large external magnetic field $\mu_o H_1 \geq 39.5$ mT is first applied along the structure diagonal to saturate the sample, followed by a smaller field $\mu_o H_2$ applied in the opposite direction. Finally the external field is reduced to zero, which will preserve the

AV or any other stable state that might have formed. The samples were imaged at remanence using MFM and the numbers of AVs was counted in selected regions, where approximately 150 intersections were examined in each run. This procedure was performed for a sequence of values of $\mu_o H_2$ that starts from a field slightly lower than the coercive field $\mu_o H_c$, where no AVs are expected and repeated in steps of 0.5 or 1.0 mT, depending on the structure, until the samples are eventually completely saturated and AVs were no longer observed in the array. The field treatment/imaging procedure was repeated at least twice for each value of $\mu_o H_2$. Hysteresis measurements and MFM imaging at selected $\mu_o H_2$ values were also conducted for angles of up to 20° from the structure diagonal to investigate the effects of the field angle on the AV formation.

4.2.2. Simulation methods

Micromagnetic simulations were performed to investigate how the hysteresis loops evolve as a function of structure size and to understand the correlation between general features of the loops and the underlying spin distributions. Hysteresis loops were simulated for scaled-down versions of structure AV-S3, the structure that showed the highest rate of AV formation in the experiments. Material parameters typical for bulk Permalloy were used, saturation magnetization $M_s = 8.6 \times 10^5$ A/m, gyromagnetic ratio $\gamma = 1.76 \times 10^{11}$ $\mathrm{s^{-1}T^{-1}}$, exchange stiffness constant $A = 1.3 \times 10^{-11}$ J/m, and magnetocrystallyne anisotropy was neglected. In addition, a large damping parameter $\alpha = 1$ was chosen to ensure rapid convergence. The AV spin distributions expected at remanence were also calculated by choosing AV-containing intermediate states in the hysteresis loop and allowing them to relax in zero field.

Hysteresis simulations generally use energy minimization routines that can take considerable amount of time and computer resources therefore strategies, such as simulating scaling-down versions of the sample, are frequently considered to minimize the computational cost. In this work, the larger structure that was simulated ($L_2 = 4$ μm) was scaled-down by a factor of 2 with respect to the real dimensions ($L_2 = 8$ μm). In addition, choosing 2-D instead of 3-D simulations also reduces significantly the computational requirements, and it is common to do so when the thickness is small compared to the lateral dimensions and when little variation in M along the thickness is expected. The smallest structure simulated here had an overall width of $L_2 = 0.8$ μm and a corresponding lateral dimension was $w_2 = 50$ nm, which is comparable to the thickness of the sample(40 nm), therefore 3-D simulations were also necessary. Both OOMMF [60] and MuMax^3 (Ref. [61]) packages were used, in this case we used OOMMF to run 2-D hysteresis simulations of structure AV-S3 with $L_2 = 0.8 - 4.0$ μm and cell size of 4×4 nm^2 and constant thickness of 40 nm while, due to its better efficiency, MuMax^3 was used to run 3-D simulations over the same range of L_2 with a cell size of $4\times4\times4$ nm^3.

4.3. Results

4.3.1. Experimental results

The hysteresis loops obtained for each array are shown in the top row of Fig. 4.4, where 20 loops were averaged for each sample. In most cases the value of Θ_K changes rapidly from positive to negative saturation near H_c; however, in sample AV-S3, the signal drops to an intermediate value of Θ_K before reaching saturation in a second abrupt drop at $H > H_c$. Steps like this are common in hysteresis loops for patterned structures and usually indicate

the presence of a transitional domain state. Sample AV-C2 may also show a similar feature but it is less pronounced; this feature is difficult to identify in the hysteresis loops of the other samples. The coercive field differs for each sample, with $\mu_o H_c$ values ranging from 5.2 to 16.0 mT (Table 4.2). Quantitative results extracted after MFM imaging are shown in the bottom row of Fig. 4.4. The fraction of AVs observed in the MFM images as compared to the number of intersections where AV formation is expected, which is two AVs per structure, is shown as a percentage value. Three sub-arrays of 5×5 elements were chosen for the imaging and counting process for each sample, which allowed for sufficiently high resolution to reliably determine the presence or absence of AVs. The imaging was repeated at least twice for each sample after re-applying the same field treatment. A stochastic character was noticed in the formation of AVs in terms of exactly which intersections contained AVs in any given run; however, the total number of AVs observed remained consistent between field treatment repetitions; fluctuations in the number of AVs for each array were typically within a few percent. The same general trend of AV formation vs. H_2 was observed for all of the samples.

The results show that the AV percentage starts to increase when H_2 is close to the coercive field H_c, reaches a maximum value at a field $H_{2,max}$ that is slightly greater than H_c, and then it decreases, producing a Gaussian-shaped distribution that is symmetric around $H_{2,max}$. The main characteristics of these distributions are tabulated in Table 4.2. The values of $H_{2,max}$ and the full width at half maximum (FWHM) of the distribution differ for the samples but the most striking difference between the samples is the maximum number of AVs stabilized, which ranges from as low as 5% up to $> 72\%$. The structures that show the highest percentage of AVs as well as the distribution widths ΔH_2 in the order of most to least favorable are AV-S3, AV-S2, and AV-C2. The others (AV-S1 and AV-C1) show only

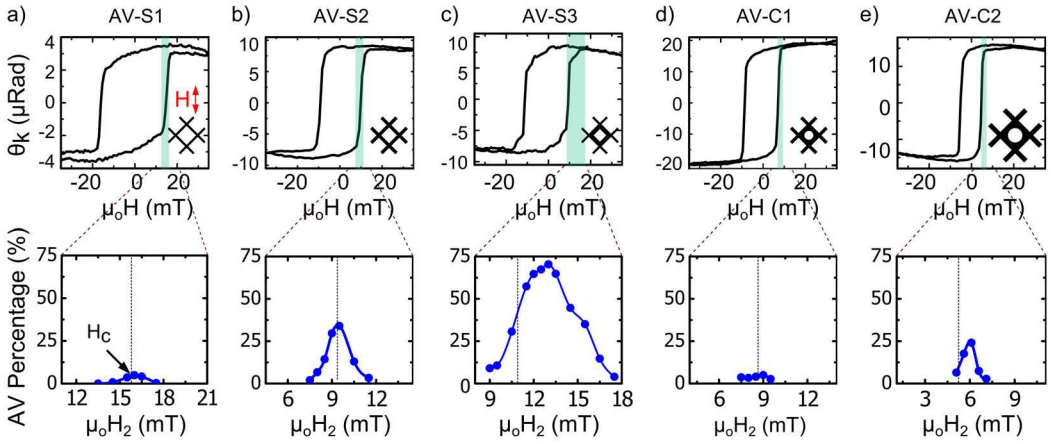

Figure 4.4. Experimental MOKE hysteresis measurements and a compilation of MFM results. The top row shows MOKE hysteresis loops for each sample. The direction of the magnetic field, applied in the plane of the sample, is indicated by the double arrow. The bottom row shows the percentage of AVs observed as a function of the secondary field H_2, as determined by counting the number of AVs observed in MFM images. Solid lines are included as a guide to the eye and the dotted lines correspond to H_c for each sample.

a few AVs. Structure AV-S3, is the sample that shows the highest number of AVs ($> 72\%$) and this is also the sample that exhibits the more pronounced shoulder in the hysteresis loop and the sample with the largest w_1/w_2.

A representative image of one of the three sub-arrays that was chosen for sample AV-S3 is shown in Fig. 4.5a. This was obtained after using $\mu_o H_2 = 13$ mT, close to $H_{2,max}$ for this sample. An individual zoomed-in structure shown in Fig. 4.5a displays an hourglass-shaped contrast at the two intersections where AVs are expected and indicated by the blue circles (labeled as AV_1 and AV_2). A scaled down simulation of AV spin distribution at remanence was used to calculate the corresponding MFM contrast at a distance of 50 nm above the sample using the procedure described in chapter 3 and it is presented in Fig. 4.5b.

The in-plane components in the simulations are reminiscent of the AV counterpart of a Landau pattern that forms in squares, which occurs due to the structure shape. The calculated image also displayed a similar hourglass-shaped contrast in intersections that

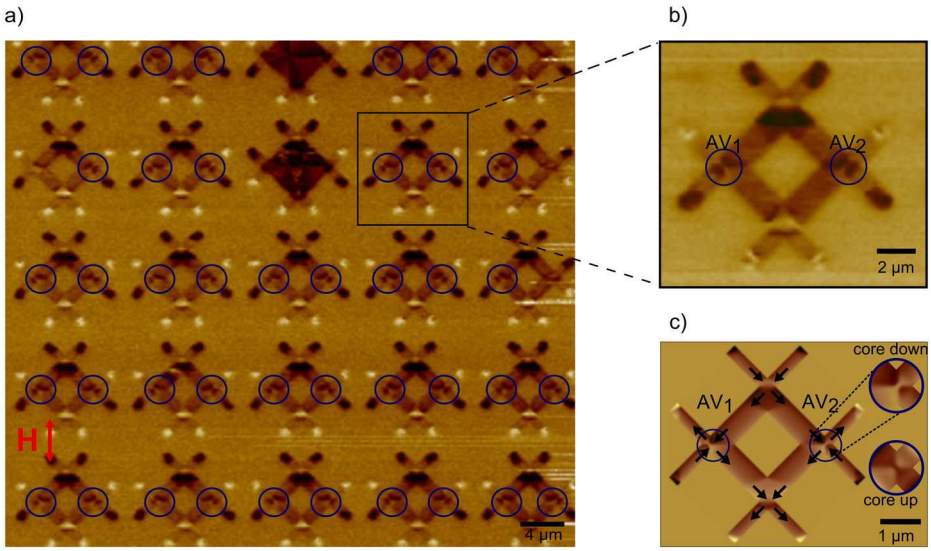

Figure 4.5. a) Experimental MFM image of a sub-array of sample AV-S3 magnetized using $\mu_o H_2 = 13$ mT along the direction indicated by the double-head arrow. Inset provides detail of the constrast in the intersection where AVs are expected to form (circled regions labeled as AV_1 and AV_2). b) Simulated MFM contrast for individual structure of the same sample. Black arrows indicate the in-plane spin distribution in regions of interest. Both core polarities are down in the structure shown in (c). The inset shows show the effect of different AV core polarity on the MFM contrast.

contain AVs, which was used to identify AVs in the experimental MFM images. The main differences between the experimental and simulated contrast are due to the lower resolution in the experimental images (approximately 50 nm for MFM). As shown in the inset of Fig. 4.5c, AVs of opposite polarities should exhibit similar contrast except that the image will appear as either a light hourglass on a dark background or vice versa depending on the core polarity. Fig. 4.5b shows a contrast consistent with that expected for downward cores and although this was also the case for most of the structures in the different arrays, control of the polarity was not one of the goals of this projects, so no intentional effort was put into that.

To determine whether the AV states, once set, are stable against thermal fluctuations, the MFM imaging was repeated after intervals of as long as seven days for randomly selected

samples. In all cases, the MFM images showed that the structures were all in the same state as they were immediately after the field treatment indicating that, once formed, the AVs are stable at room temperature.

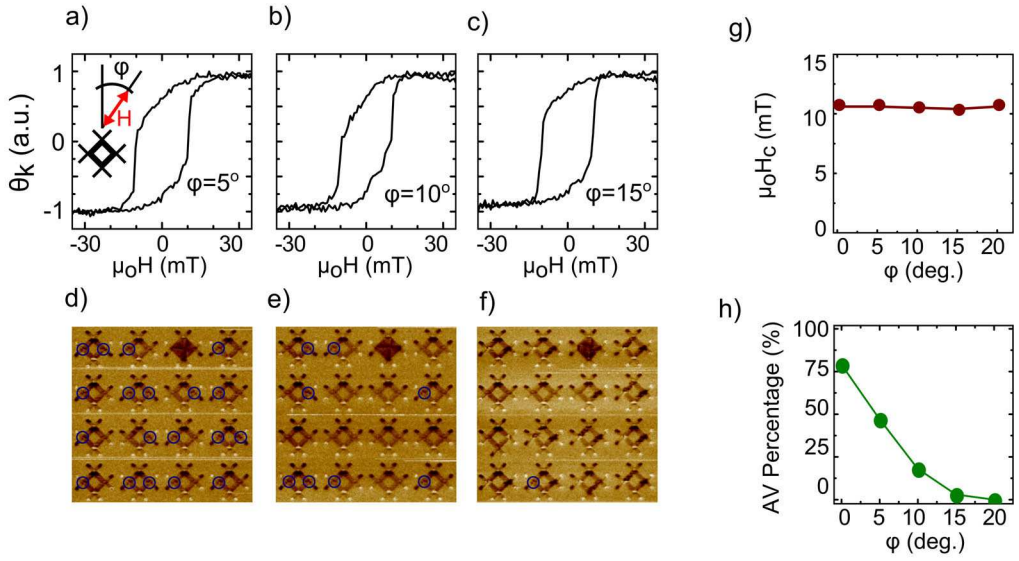

Figure 4.6. MOKE hysteresis loops (a-c), and MFM images (d-f) of a 35×35 μm^2 sample area obtained with H applied at angles ϕ of 5° ((a) and (d)), 10° ((d) and (e)), and 15° ((c) and (f)) with respect to the diagonal of sample AV-S3. The MFM images were obtained after applying $\mu_o H_2$ =13 mT. Blue circles in the MFM images indicate the presence of an AV. The H_c and the rate of AV formation are shown as a function of ϕ in (g) and (h), respectively, where the symbols represent the data and the lines are included as a guide to the eye.

The effect that the angle at which H is applied, with respect to the diagonal of the structure, has on AV formation was also investigated. Figure 4.6a-c shows MOKE hysteresis loops for selected angles for sample AV-S3 and corresponding MFM images that were obtained with $\mu_o H_2$ = 13 mT, which corresponds to $H_{2,max}$ for θ = 0. The coercive field H_c did not show significant variation with increasing angle (Fig. 4.6g), therefore the value of $H_{2,max}$ obtained at $\theta = 0°$ was used for all measurements. The corresponding MFM images (Fig. 4.6d-f show that the number of AVs decreases considerably with increasing angle (Fig. 4.6h). The percentage of AVs drops from ∼78% (slightly higher than observed in the

initial measurements) to 47% for a deviation from the diagonal of only 5°. As the angle is increased further, the number of AVs decreases rapidly and for an angle of 20°, no AVs were observed.

4.3.2. Micromagnetic simulation results

Micromagnetic data provides details of the spin re-orientation and can help to understand the different transitions during the reversal process. Here micromagnetic simulations were used to study the mechanics of these transitions and the effect of the structure's overall width L_2 on the coercive and critical fields. Simulated hysteresis loops for selected scaled-down versions of sample AV-S3 are presented in Figure 4.7a. The thickness was held constant at 40 nm, as were the ratios of w_1/w_2, and L_1/L_2. The simulated hysteresis loops presented in Fig. 4.7a were obtained using 2D simulations with OOMMF. The values obtained for H_c and $\mu_o \Delta H$ were slightly lower for the 3D simulations, which are shown in Figs. 4.7b and 4.7c, respectively (calculated using MuMax^3), but the 2D and 3D hysteresis loops are otherwise very similar. Since the 3D simulations are expected to be more accurate only those results are shown. See appendix A for a comparison of the simulations using both micromagnetic solvers.

Along with the hysteresis loops, the corresponding spin distributions were examined during the reversal process. It was observed that after reducing the external field from saturation, the spins reorient along the directions of the legs due to shape anisotropy and that the wider areas of the structure, in this case located in the central region, lead the reversal process, in agreement with [71]. At field H_c, the central region begins to reverse while the outer legs adjacent to these two intersections, due to its higher shape anisotropy, act as pinning sites for the initial magnetization direction. This causes the AVs to form at

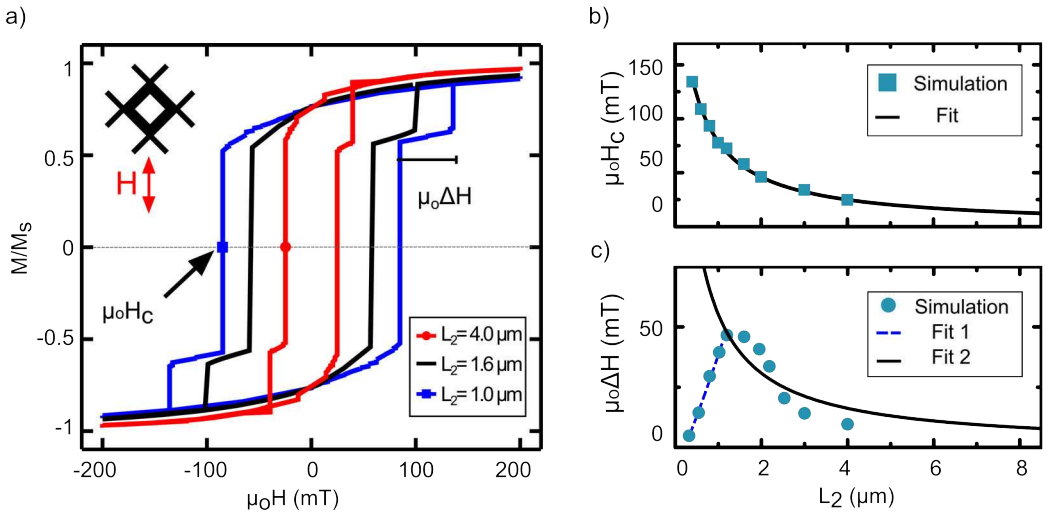

Figure 4.7. a) Simulated hysteresis loops for scaled versions of structure AV-S3 ($w_1/L_2 = 1/8, w_2/L_2 = 1/16$, and $L_1/L_2 = 1/2$) with $L_2 = 1.0, 1.6$ and 4.0 μm. The coercivity $\mu_o H_c$ and field window of AV stability $\mu_o \Delta H$ are shown as a function of L_2 in b) and c), respectively. See discussion for details of the fits represented by the solid lines. These results were obtained using 3D simulations with MuMax[3]

the intersections that are perpendicular to H. Once formed, the AVs persist over a finite field window $\mu_o \Delta H$ up to the annihilation/saturation field. Near both transition fields the field step in the simulations was kept at 1 mT to capture their value with high accuracy as compared to regions of the hysteresis loop with less activity where the field step was chosen such that only included ten points between the saturating field and the beginning of the transition.

Figure 4.7b shows that H_c, also the AV nucleation field, decreases monotonically with increasing L_2. The field window $\mu_o \Delta H$ (Fig. 4.7c) exhibit two different regimes. For small values of L_2, namely for $L_2 < 1\mu$m, $\mu_o \Delta H$ increases almost linearly with increasing L_2 and it levels off at $L_2 = 1$ μm. However for $L_2 \geq 1.6$ μm it decreases as a function of L_2. The change in behavior of the $\mu_o \Delta H$ curve shown in Fig. 4.7c can be understood by examining the spin distributions (see Fig. 4.8). The basic mechanism of the AV nucleation does not change appreciably with size as shown in Fig. 4.8, where the reversal process starts in the

central region, at the nucleation field, with some vortex states forming in the intersections perpendicular to the diagonal and traveling away from the center driving the magnetization reversal in their immediate neighborhood. Additional vortices are formed that, like the initial ones, eventually reach one of the edges of the sample and disappear. Once the central region is aligned parallel to the external field, AVs are formed in the intersections where the original vortices appeared. The reversal process continues in the external legs along the direction of the field.

The polarities of the vortices shown in Fig. 4.8 are all $p = -1$ (see section 1 for definition of p), however a stochastic character was observed for the individual polarities. The trajectories of the traveling vortices are affected by the particular combination of polarities, however the general mechanism is the same and hence a single trend in H_c vs. L_2 is observed. The initial and final AV states in the far left and right columns of Fig. 4.8 respectively are equilibrium magnetization configurations. Since a large damping parameter is used ($\alpha = 1$), the states shown in the central columns of Fig. 4.8, which are transient intermediate states, should not be interpreted as true dynamic states of the structure but instead as a general indication of the annihilation mechanism.

On the other hand, the spin distributions show that the final step in the reversal process, the annihilation of the AV, does change with L_2. Figure 4.9 presents spin distributions of selected states before, during, and after the annihilation process for $L_2 < 1$ μm (0.4 and 0.8 μm) as well as for $L_2 > 1$ μm (1.6 μm), obtained using 3D simulations in MuMax^3.

For $L_2 < 1$ μm, the reversal starts from the central region and the AV moves towards the outer corner where it annihilates. For $L_2 = 0.4$ μm, two domain walls remain next to the intersection after the AV annihilation, one in each of the narrow outer legs, and the domain

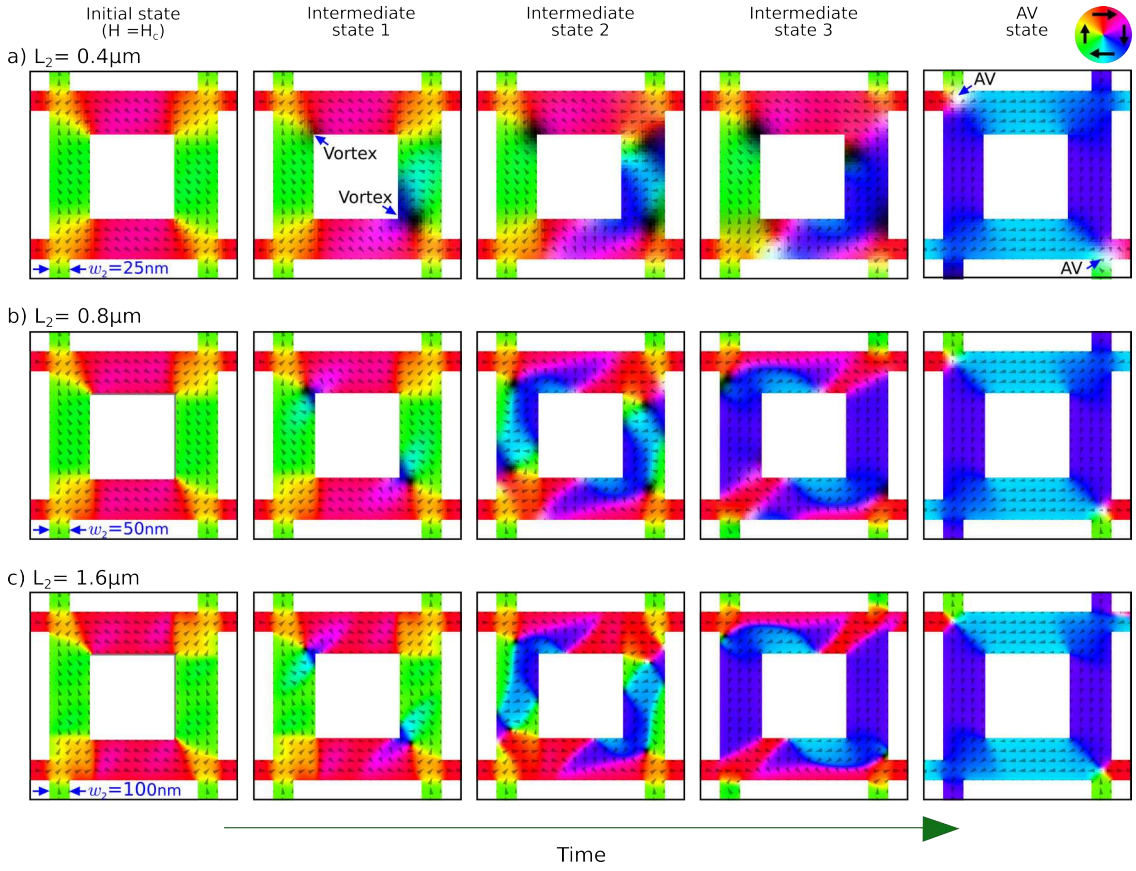

Figure 4.8. Selected spin distributions during the AV nucleation process are shown for scaled versions of structure AV-S3 with L_2 = a) 0.4, b) 0.8 and c) 1.6 μm. The initial state (left column) corresponds to the spin distribution once the system reaches $H = H_c$ and subsequent columns illustrate the changes at the same fixed field. The reversal of the central region is driven by the appearance of traveling vortices that promote the reorientation of the spins and eventually disappear. The color contrast corresponds to the direction of the magnetization, and the cones indicate the direction of the spins, which lie mainly in-plane with the exception of the AV cores and within some domain walls. Areas that are white (black) represent regions where the magnetization points out of (into) the page.

walls propagate along the legs to complete the reversal. In contrast, for $L_2 = 1.6$ μm the reversal starts in the narrow outer legs where the reversal is by quasi-coherent rotation and the AV annihilation follows. For larger structures, the final reversal step is similar except in some cases domain walls are also involved. Hence, the change in functional behavior of the $\mu_o \Delta H$ vs. L_2 at $L_2 \sim 1$ μm reflects a change in the mechanism of the final reversal step.

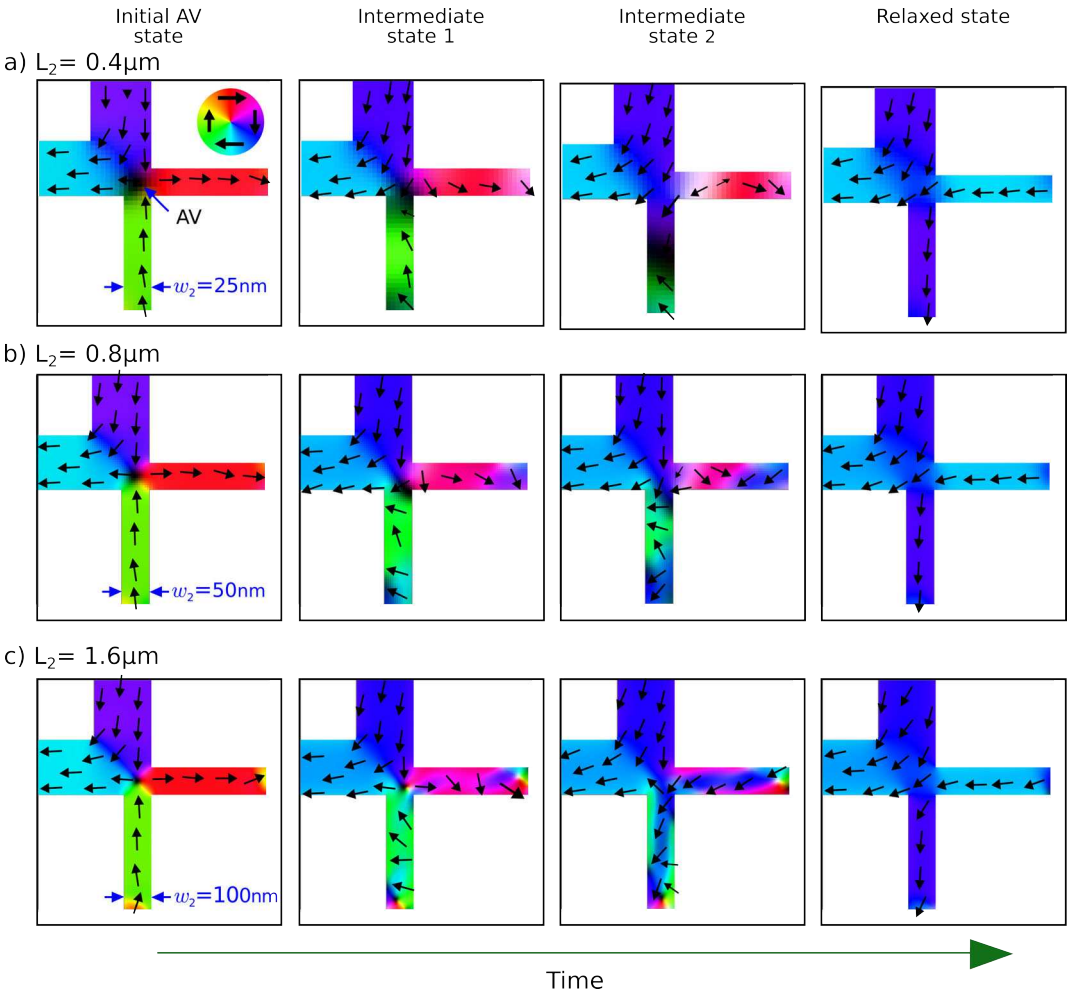

Figure 4.9. Selected simulated spin distributions for scaled versions of structure AV-S3 with L_2 = 0.4, 0.8 and 1.6 μm to illustrate the final step in the reversal process. Zoomed images of one of the AV-containing intersections, each with an area of $L_2/2 \times L_2/2$ that is outlined by dashed lines in Fig. 4.4, are shown for each structure. The images show the AV state at the start of the final reversal step (left column), and subsequent columns are transient intermediate states that occur during the reversal process, and the final (right column) relaxed, saturated state. The color contrast corresponds to the direction of the magnetization, and the black arrows indicate the direction of the spins, which lie mainly in-plane with the exception of the AV cores and within some domain walls. Areas that are white (black) represent regions where the magnetization points out of (into) the page.

For $L_2 < 1$ μm, the AV annihilation leads the reversal, whereas the reversal begins in the legs for $L_2 > 1$ μm and can be more complex.

4.4. Discussion

To gain a better understanding of the simulation results shown in Figs. 4.7b-c), we compare them with a simple phenomenological model. The structure reversal proceeds such that the central region reverses first at field H_c and then the outer legs reverse at field $H_c + \Delta H$. Here, we break the structure down into rectangular sections to represent the inner and outer regions and calculate the demagnetization factors. Given the fact that these regions are magnetized longitudinally we consider them as ellipsoids in a first approximation, whose demagnetization factors are easier to calculate than the rectangular case. The demagnetization coefficients N_w, N_L, and N_z along the wire width, length, and thickness, respectively, were calculated using Ref. [45] assuming that the lengths of the central and external legs are $L_{in} = L_1 - 2w_2$ and $L_{out} = (L_2 - L_1)/2$ and are shown in Table 4.2. Since the sum $N_w + N_L + N_z = 1$, the value of N_z is can be obtained from the other coefficients and hence is not included in the table.

Sample	$(N_L)_{in}$	$(N_w)_{in}$	$(N_L - N_w)_{in}$	$(N_L)_{out}$	$(N_w)_{out}$	$(N_L - N_w)_{out}$	ΔN	$\mu_o H_c$ (mT)	$\mu_o H_{2,max}$ (mT)	FWHM (mT)	Peak AV (%)
AV-S1	0.067	0.004	0.063	0.066	0.008	0.058	-0.005	16.0	16.0	1.67	5.0
AV-S2	0.044	0.007	0.037	0.043	0.010	0.033	-0.004	9.2	9.5	1.69	32.4
AV-S3	0.033	0.006	0.027	0.066	0.008	0.058	0.031	11.2	13.0	4.95	72.1
AV-C1	0.033	0.008	0.024	0.043	0.010	0.033	0.009	8.6	9.0	0.28	5.0
AV-C2	0.019	0.004	0.015	0.022	0.005	0.017	0.002	5.2	6.0	1.00	24.1

Table 4.2. Dimensions of the inner and outer regions for the different samples and corresponding demagnetization parameters. The last four columns contain parameters extracted from the experimental hysteresis and MFM data.

One of the simplest models of ferromagnetism is the Stoner-Wohlfarth model, which considers that the magnetic moments of the ferromagnet are aligned parallel to each other all the time, i.e. that the sample is in a single domain state, with constant exchange energy. Under the application of an external magnetic field, the magnetization undergoes coherent rotation and the only competing energies are that of the external field and the anisotropy

term, which in our case comes from the shape anisotropy. This approach is only meant as a simple estimate of the role of the shape anisotropy in the reversal and will be used here with that in mind. Examining the Stoner-Wohlfarth model for coherent reversal of a prolate spheroid [76] suggests that the coercivity for a general ellipsoid with strong in-plane anisotropy ($N_z \sim 1$), should scale as $H_c \sim N_w - N_L$. The shapes of the structures are more complex and, furthermore, the MFM images indicate that other domain states occur during the reversal. Nevertheless, $\mu_o H_c = C_1(N_w - N_L)_{in}$, where C_1 is a fitting parameter, provides a reasonable fit to H_c vs. L_2 when the demagnetization coefficients for the inner region are used (Fig. 4.7b)), suggesting that this simple model provides a useful qualitative guide for how H_c should scale with the structure dimensions. Following a similar approach, $\mu_o \Delta H = C_2 \Delta N$, where $\Delta N = (N_L - N_w)_{out} - (N_L - N_w)_{in}$, was used to fit the simulation results with C_2 as a fitting parameter for $L_2 \geq 1.6$ μm. The simulations and model both show a decreasing trend for $L_2 \geq 1.6$ μm and the spin distributions suggest that the AV annihilation occurs, at least in part, via quasi-coherent reversal of the outer legs, however, the agreement is not as good, which suggests that a more refined model for the annihilation is needed.

Extrapolating these results to the dimensions of sample AV-S3 ($L_2 \approx 8$ μm), yields predicted values for $\mu_o H_c$ and $\mu_o \Delta H$ of approximately 13.9 mT and 10.9 mT, respectively. These are larger than the values extracted from experimental MOKE data of 11.2 and 3.8 mT, respectively. Note that the latter value is estimated from the step width in the MOKE data and is smaller than the FWHM obtained from the MFM data of 4.95 mT. The model provides a reasonable estimate for $\mu_o H_c$ −within $< 20\%$ of the measured value, which is good considering the assumptions used for this model− but the model is not refined enough

to provide quantitative agreement for $\mu_o \Delta H$. In addition, the result obtained from a MOKE measurement is an average of many structures and as a result the shelf observed in the hysteresis loop is smeared out.

Examination of the spin distributions from the micromagnetic simulations indicates that the wider areas of the structure that have lower shape anisotropy lead the reversal process for the AV nucleation step, whereas the external legs, which are thinner and have higher shape anisotropy, help to pin the magnetization during the reversal process. It follows that structures with more of a difference between the aspect ratio of the central vs. the outer legs (and consequently a larger difference in demagnetization coefficients) should show higher reliability of AV formation. This general idea agrees well with the observation that structure AVS-3 not only shows a greater number of AVs but also a larger stability window $\mu_o \Delta H_2$ (Fig. 4.7). The MFM results as well as a comparison with the micromagnetic simulations suggest that the shoulder in the hysteresis loop observed for this sample (Fig. 4.4d) is indicative of the formation of AVs in these structures, although when AVs are present in lower numbers this feature is more difficult to observe (e.g., for sample AV-S2).

As mentioned above, the ellipsoid demagnetization coefficients provide a reasonable description of the main trends observed for H_c and ΔH obtained from the simulations, provided the sample dimensions are large enough ($L_2 \geq 1.6$ μm). Table 4.2 shows that the approximate demagnetization coefficients for the inner and outer regions are also correlated with some features of the experimentally measured samples. For the AV-S samples, sample AV-S3 shows the largest FWHM and this sample also has the largest ΔN, which is consistent with the trend observed in the simulations. It also has the large number of AVs. Sample AV-S1 has a larger H_c as compared to AV-S3, and it also has a larger $(N_L - N_w)_{in}$ as compared

to AV-S3. The parameters also suggest that samples AV-S1 and AV-S2 should have similar FWHM since they have almost identical ΔN, which is also consistent with the experiments. The data show, however, that in spite of the almost equal FWHM and ΔN, sample AV-S2 exhibits a much higher percentage of AVs of 32% as compared to only 5% for sample AV-S1. The model provides a reasonably good description of the critical fields but other factors may influence whether AVs actually form as part of the intermediate state. The experiments suggest, in this case, that the larger w_1 and w_2 of sample AV-S1 favor the formation of AVs over the smaller wires in sample AV-S2. The trends in $(N_L - N_w)_{in}$ and ΔN also match the observed trend in H_c and the FWHM, respectively, for the AV-C samples, which is somewhat surprising since an ellipsoid is a poor approximation for the shape of the central connecting wires. Here, the larger FWHM is not correlated with the higher percentage of AVs, it is rather the structure that is larger in size that appears to support the higher percentages of AVs, though the percentage is still lower than structures AV-S2 and AV-S3, both of which are AV-S structures. It is interesting to note that scaled-down simulations of sample E (with $L_2 = 0.4 - 2.0$ μm) showed no AVs, whereas the experimental MFM images show that while the success rate was low, a small number of AVs did form. This could be related to defects in fabrication that provide nucleation sites for the AVs or it could be due to the fact that the simulations are at zero temperature, which can sometimes make it more difficult to accurately predict the nucleation. Overall, the results suggest that increasing the structure asymmetry will improve the AV formation rate and that the demagnetization factors provide a reasonable estimate of trends in the critical fields.

4.5. Conclusions

The effect of various geometric parameters on the formation of AVs was investigated for two variations of pound-key-like structures with either circular or square central regions. A combination of MOKE hysteresis measurements and MFM imaging showed that the critical magnetic field at which the highest AV formation rate occurs is slightly higher than the coercive field, which is likely due to the existence of a distribution of nucleation fields within the array.

The experiments also showed that the AV formation is sensitive to the relative dimensions of the sample. A significant enhancement of the AV formation −as high as 79% as compared to $< 5\%$− was found for structures with a high degree of asymmetry, i.e, a combination of thin external legs and wider areas within the central region, which also showed an intermediate state in the hysteresis loop and is consistent with the idea that a mismatch in shape anisotropies aids in the AV formation. It was also found that the AV formation is sensitive to the angle of the applied field, where the highest AV formation rate is observed when the field is aligned along the structure diagonal.

Micromagnetic simulations revealed that the regions with lower shape anisotropy lead the reversal in the formation step and the upper field limit for the AV stability is related to the reversal of the regions with higher shape anisotropy. The annihilation mechanism changed to one that involves domain wall propagation when the smallest structure dimensions were below 60 nm.

These results demonstrate how the shape anisotropy affects the formation of magnetic AVs, and provide general guidelines on how to maximize the AV formation, which will facilitate future investigations of this topological magnetic state.

CHAPTER 5

Antivortex Dynamics

5.1. Introduction

The dynamics of ferromagnetic systems with non-uniform magnetization such as vortices and AVs has generated increasing interest in recent years both from the point of view of fundamental physics and also because of the potential for applications in new technologies. Knowledge of the dynamic properties of these spin textures, such as the excitation spectra and the spatial configuration of their normal modes, is very valuable for a proper understanding and accurate prediction of their response to different type of excitations. In addition, information on how the resonant modes of these spin textures interact with SW in adjacent microstrips might be crucial in the development of the new technologies including logic and magnonic devices.

Vortices and AVs are topological counterparts of one another and although they have some common characteristics such as a small (∼10 nm) OOP core, the differences in their IP magnetization (see Fig. 1.1a) lead to important variations in their dynamic properties [11]. Vortex excitations have been studied intensely for more than a decade [77–82]. For sub-micron cylindrical dots, the frequency of the gyromode (see introduction of Chapter 6 for description of the gyromode) has been reported to be proportional to the dot aspect ratio [78] and is usually in the 100-MHz range. Excitation of this mode can also lead to IP/OOP switching of the core, which is of particular interest for non-volatile data storage applications. At higher frequencies (typically several GHz) radial [80] and azimuthal [82] SW modes can be observed.

The AV configuration, on the other hand, has received much less attention than the vortex and comparatively a few studies have been published thus far. Nevertheless, the AV has some advantages compared to the vortex, for example in the case of an AV located at the intersection of long wires the topology of the spin configuration provides a natural path for channeling SW. The dynamic characteristics of an AV are predicted to have many similarities to those of a vortex, including size-dependent gyromode and dynamic core reversal [10–12, 83–85, 13]. In fact, excitation of the gyrotropic mode of an AV has been demonstrated using spin-polarized currents and alternating magnetic fields [11]. In addition, experiments with circular-rotational currents show that the gyromode of a vortex (AV) is excited only if the sense of rotation of the field is the same (opposite) as the intrinsic sense of gyration [86, 14].

Higher frequency excitations of an AV have been less explored than the translational gyromode. In [10] micromagnetic simulations are used to investigate the response of an AV inside an astroid-shaped ferromagnet to pulsed magnetic fields applied at different angles of the sample surface. In addition to the low-frequency gyromode, the authors report azimuthal and radial SW modes similar to those found in a vortex. However recent experimental results performed by our group using Brilluoin light scattering [18] suggest that when the AV is located in geometries such as rectangular crosses or more involved structures, a new level of complexity is added to the dynamical response and a more detailed study is needed.

In this work the high-frequency excitation modes of a magnetic AV, stabilized at the perpendicular intersection of two microstrips in pound-key-shaped Permalloy structures [71, 22], were studied using micromagnetic simulations. Although the pound-key shape considered

in this work might seem more complex than the astroid shape used in [10], this particular geometry offers some key advantages, for example the longer microstrip legs allow for SW propagation: the fact that the AV is stabilized in the intersection of two microstrips facilitates the study of coupling between AV modes and SW in the a wires. In the present chapter, the high frequency spectrum obtained for IP and OOP excitation is discussed along with maps of the spatial distribution of the Fourier amplitude for each mode. The coupling of these modes to propagating SW in the adjacent microstrips is investigated using dispersion calculation for backward volume (BV) SW. Fourier analysis reveals spatial modes with standing and propagating characteristics. It was found that the observed modes involve a combination of quantization along the diagonal of the intersection and coupling to SW's in the legs. Also, the results of this study show that the backward volume dispersion curves provide a useful tool to predict possible leg modes but that the mode symmetry also factors into the efficiency of the intersection/leg coupling.

5.2. Methods

The dynamic spectra and mode maps were obtained for a magnetic AV, stabilized at one of the intersections of a pound-key-shaped Permalloy structure (Fig. 5.1a). Two different magnetic excitation directions were considered: IP and OOP as well as several sample sizes: w = 0.25, 0.50, and 1.00 μm, where w is the width of the narrower leg of the structure. In addition, the effect of using different excitation types, long excitation, short pulse and continuous wave (CW) was also explored. Standard magnetic parameters of Permalloy (see section 3.3) were used for the simulation. The thickness was 37 nm for all the simulations presented here and a cellsize of $4 \times 4 \times 37$ nm^3 was used, i.e., only one cell along the thickness

because the sample is thick enough to yield a stable AV state but thin enough that the spin configuration is still essentially two dimensional. Additional simulations performed with smaller cells in all dimensions showed no significant differences. All the simulations were performed using MuMax^3 software.

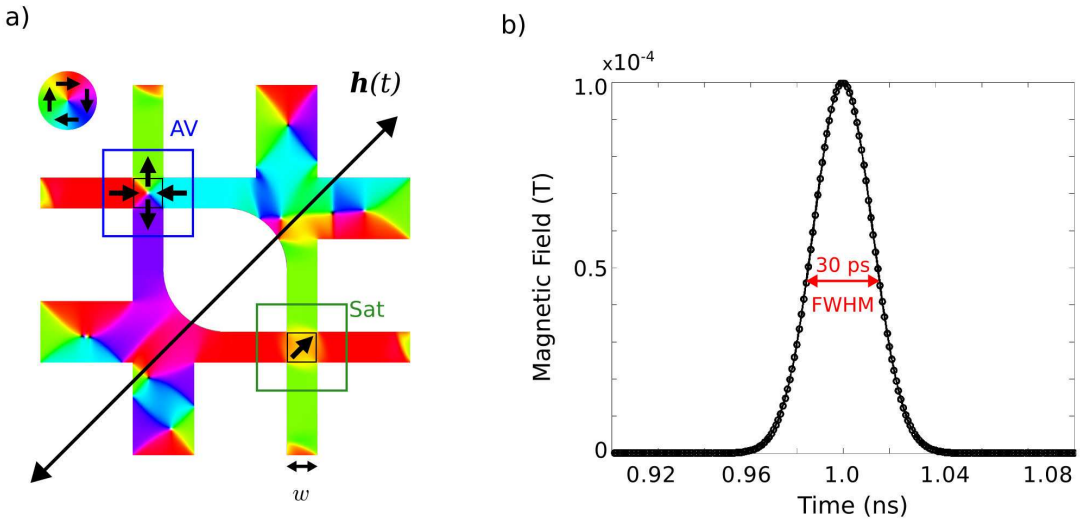

Figure 5.1. a) Sample mask, the IP orientation of local spins of the initial static configuration is indicated by the color, as defined by the color wheel inset, and highlighted by the black arrows. Two regions, AV and Sat as well as corresponding subregions are defined by the big squares and small squares, respectively, and will be used to calculate the spatial modes and frequency spectra. The width of the legs is represented by w. The double arrow along the diagonal shows the direction of the excitation pulse $\boldsymbol{h}$(t) for the in-plane excitations. b) Time profile of the 30-ps Gaussian pulse, $\boldsymbol{h}$(t).

Two different square regions were defined, one that includes the intersection where the spins form an AV state and will be referred to as AV, and the Sat region, which includes the intersection where the spins align in the same direction as the magnetic field excitation $\boldsymbol{h}$(t) (Fig. 5.1a). The smaller squares inside these regions were used to obtain the frequency spectra by averaging the OOP component of the magnetization over such squares. Also, the normal mode maps were calculated for both the AV and Sat regions.

5.3. Results

5.3.1. In-plane Excitation

The details of the frequency spectra obtained from a sample with $w = 1.0$ μm after a 30 ps, 0.1 mT short IP pulse, $\boldsymbol{h}$(t) (Fig. 5.1b), are presented in Fig. 5.2, where the labels a-n) correspond to selected resonant frequencies for the AV state (blue line). The spectra were obtained by averaging the Fourier amplitude over 1.0×1.0 μm^2 subregions defined by the black boxes in the insets. The low frequency gyrotropic mode is excited at around 120 MHz and, like in the vortex case, it involves circulation of the core about its central equilibrium position. In addition to the low-frequency gyrotropic mode, a number of higher-frequency modes are observed. Notable peaks start at 1.90 and 2.22 GHz for the AV and there is significant activity at higher frequencies. The strongest peaks are at around 5.5 GHz for both AV and Sat states and a broad region with weaker but still significant amplitude is observed for higher frequencies in the AV case, while the amplitude drops more drastically at higher frequencies in the Sat case.

Fig. 5.3 shows the Fourier amplitude, A (top row), phase, ϕ (central row) and $A\cos(\phi)$ (bottom row) for the four lowest modes observed in the AV spectrum a-d). Combining the information from the amplitude and phase is actually very convenient since $A\cos(\phi)$ captures the magnetization configuration at a particular instant of time, providing a compact description of the mode, and will be used from now on to present the eigenmodes.

In Fig. 5.3 it can be seen that a-b) and c-d) represent pairs of modes that have similar amplitude characteristics respectively. The lowest frequency modes 1.90 and 2.22 GHz are very localized inside of the intersection and show an X-shaped profile where the amplitude is mainly along the diagonals with no significant amplitude in the legs. As the frequency

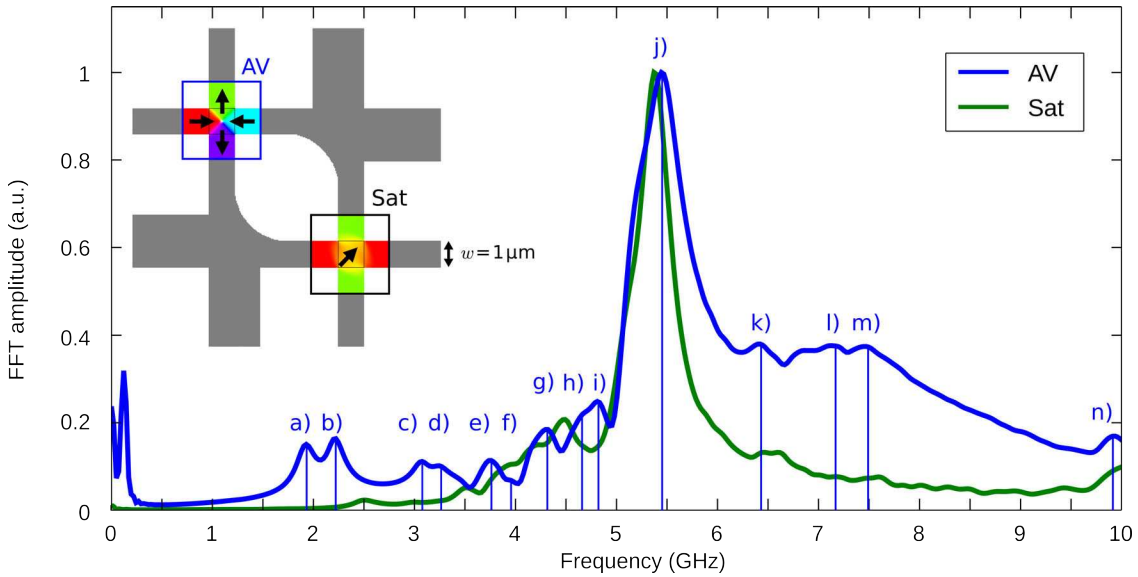

Figure 5.2. Frequency spectra calculated for the AV and Sat spin configurations after a 30 ps, 0.1 mT in-plane magnetic field pulse. The black arrows indicate the local spin orientation for each case. The spectra were obtained by averaging the Fourier amplitudes over the AV and Sat intersections (smaller black boxes) and the amplitudes have been normalized to the strongest mode of each spectrum (originally 1079 and 948.8 units, respectively).

increases so does the activity in the legs and this trend continues for modes at frequencies higher than the ones shown in Fig. 5.3. The phase information reveals that the modes shown in Fig. 5.3a-d circulate about the center of the intersection, similar to the azimuthal modes observed in vortices [82]. In Fig. 5.3a-b are pair as are c-d and the individual modes within each pair have opposite rotation direction, either clockwise or counterclockwise as indicated by the curly black arrow in the phase plots. To visualize the dynamic behavior of the normal modes the phase, ϕ, in $A\cos(\omega t+\phi)$ can be advanced over a full period to create sequences of images that unveil the evolution of the mode. Such sequences are shown in Appendix D for selected AV modes and multimedia animations can be found as supplemental material in [18] for selected AV resonant modes and corresponding off-resonances Sat modes. Analysis of the phase evolution reveals that the 1.9 and 2.2 GHz are indeed counter-clockwise and clockwise circulating modes, respectively, while the Sat state shows characteristics of standing SW's.

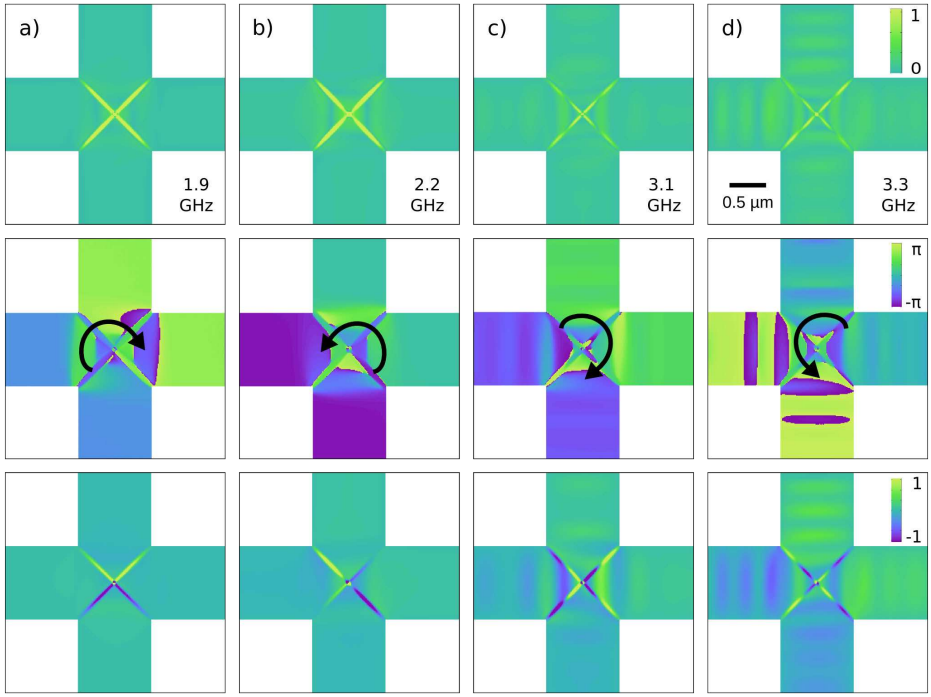

Figure 5.3. Spatial distribution of the Fourier amplitude, A (top row), phase, ϕ (central row), and product $A\cos(\phi)$ (bottom row) for the regions containing an AV with positive core polarity. These modes involve circulation and the curly black arrows represent the sense of rotation (increasing phase) around the center.

Higher frequency modes involve the superposition of different excitations within the AV and leg regions, with SW's in the legs that are quantized across the leg width. For example the modes at 3.1 and 3.3 GHz involve not only circulation around the core in the intersection region but also propagation of SW's along the legs. The resulting motion is more complex compared to the lower frequency (1.9 and 2.2 GHz) azimuthal modes. For $f \geq 3.1$ GHz there is quantization across the leg width, which is consistent with what is expected for confined SW's propagating along the leg axis [87], and the number of antinodes increases with frequency.

In order to obtain more information about the characteristic wavelengths of each mode cross-sectional cuts were extracted from the full mode maps along three particular directions: across the leg width, along the diagonal of the intersection, and along the legs (y, r, and x,

respectively, as illustrated in the insets of Fig. 5.4). These cross-sectional cuts are shown with solid lines in Fig. 5.4, normalized to the maximum amplitude of each oscillation. A 180-degree phase-shifted mirror image is also included (dashed lines) to help visualize the quantized character of the different modes. The width profiles (Fig. 5.4a) for the AV show sinusoidal-like quantization, as do the half-diagonal profiles (Fig. 5.4b). The modes in Fig. 5.4a-b are classified according to their quantization order, i.e. the number of antinodes observed across the width and half-diagonal, and are labeled using mode number indices m and n, respectively. The profiles along the legs (Fig. 5.4c) show oscillating behaviour for $f \geq$ 3.1 GHz and the wavelength tends to decrease at higher frequencies. There is no evidence of quantization in this direction and the amplitude generally decreases as a function of distance from the intersection, suggesting that the intersection acts as a SW source. Also, there is no significant activity in the legs for $f < 3.1$ GHz.

The profiles along the leg for the Sat case (Fig. 5.4d) show that most of the activity, in that case, occurs in the legs and as the frequency increases so does the amplitude in the intersection, going from basically no signal inside the intersection for the lowest modes to an amplitude of about the same value as in the legs for the highest frequency modes shown in Fig. 5.4. Also the wavelengths in the legs are longer than for the AV case. The data presented in Fig. 5.4 provides evidence of quantization and allows us to estimate the relevant wavelengths along the different directions, however because of the normalization it does not provide a direct representation of the relative strength of the modes. In addition, since the cross-sections were extracted from the modes map they only capture the profiles of the modes at a particular instant of time and to investigate the propagating character of the waves the phase must be varied, as argued earlier.

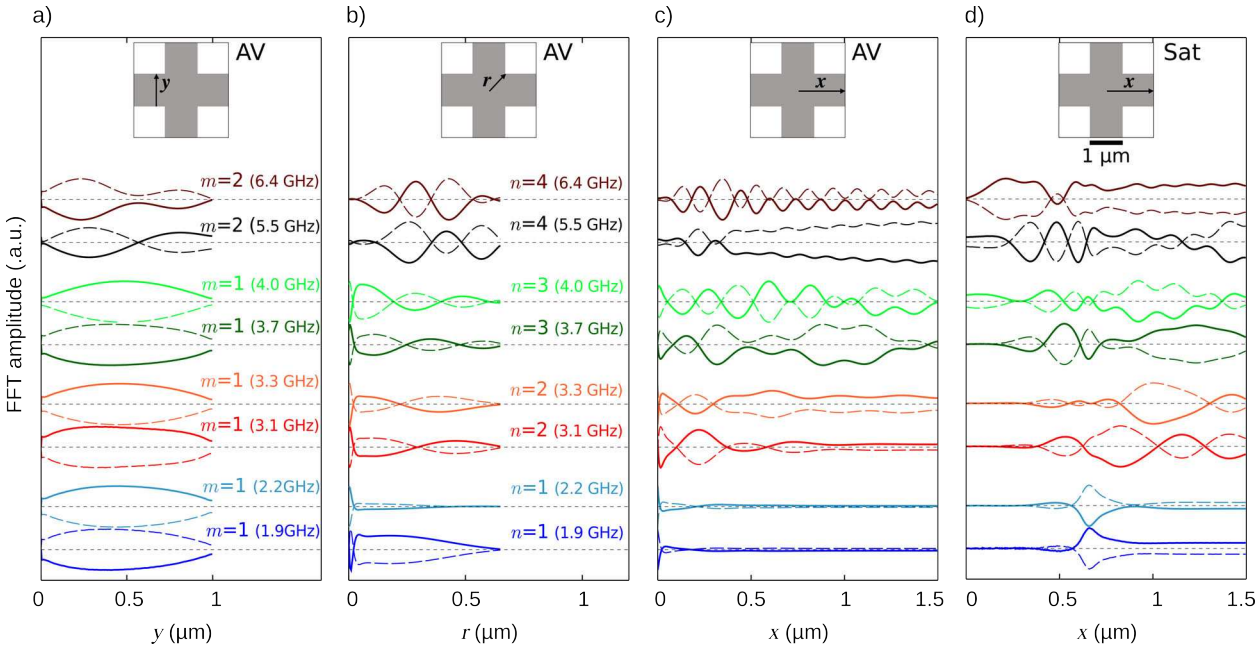

Figure 5.4. Mode profiles along different directions y, r and x as defined in each inset for a region containing an AV (a-c) and also for the Sat region along x (d). The cuts are one cell wide (4 nm) and have been normalized to the maximum amplitude of each profile. The solid and dashed lines represent $A\cos(\omega t_o + \pi)$ and $A\cos(\omega t_o - \pi)$, respectively, where the later was added for easier visualization of the mode profile. The approximate quantization number of a) the width and b) diagonal modes are labeled using m and n, respectively, based on the number of antinodes. Quantization is not expected along the legs (x direction) due to the long length, however, a dominant wavelength is generally observed for each mode for $f \geq$ 3.1 GHz, as shown in c).

Approximate values for the SW wavelengths λ_y, λ_r, and λ_x along the different directions y, r, and x respectively, as defined in Fig. 5.4, were estimated based on these profile plots by simply counting the number of oscillations in a given length and are presented in table 5.1, including higher frequency modes not shown in Fig. 5.4, along with their corresponding wavenumbers $k_i = 2\pi/\lambda_i$. In some cases complex beating patterns were observed along the diagonal and the legs, indicating the superposition of more than one wave, and a single wavelength could not be established visually.

Two dimensional mode maps for the AV and Sat cases are presented in the far left and right columns of Fig. 5.5, respectively, for selected frequencies from the the AV spectrum,

f (GHz)	m	λ_y (μm)	k_y (μm^{-1})	n	λ_r (μm)	k_r (μm^{-1})	λ_x (μm)	k_x (μm^{-1})
1.90	1	2.00	3.14	1	1.41	4.44	—	—
2.22	1	2.00	3.14	1	1.41	4.44	—	—
3.07	1	2.00	3.14	2	0.71	8.89	0.40	15.71
3.27	1	2.00	3.14	2	0.71	8.89	0.33	18.85
3.74	1	2.00	3.14	3	0.47	13.33	0.29	21.99
3.97	1	2.00	3.14	3	0.47	13.33	0.24	26.70
4.32	1	2.00	3.14	—	—	—	0.20	31.42
4.64	1	2.00	3.14	—	—	—	0.18	34.56
4.81	1	2.00	3.14	—	—	—	0.18	34.56
5.47	2	1.00	6.28	4	0.35	17.77	0.16	39.27
6.42	2	1.00	6.28	4	0.35	17.77	0.13	47.12
7.15	3	0.67	9.42	5	0.28	22.21	0.12	53.41
7.47	3	0.67	9.42	6	0.24	26.66	0.11	56.55
9.93	3	0.67	9.42	8	0.18	35.54	0.08	75.40

Table 5.1. Dominant wavelengths and corresponding wavenumbers across the width (y), along the half-diagonal (r), and along the leg (x) (See Fig. 5.4a). The values for the mode numbers and wavelengths represent the best estimate obtained by visual inspection of the oscillations in a given length from the mode profiles shown in Fig. 5.4. Blank spaces indicate a single value could not be determined using this method.

indicated by the letters a-n) in Fig. 5.2. Note that at these frequencies the Sat modes are mainly off-resonance. In addition, two dimensional spatial Fourier transforms, which convert the mode information from the spatial domain into reciprocal space, were performed on selected regions of each one of these modes. The spatial Fourier transform is a more general and, in principle, accurate way to obtain the relevant k's and λ's as compared to the simple approach of just counting the number of oscillations, and it is particular advantageous when complex beating patterns are observed since modes that are not immediately apparent visually can be identified more readily.

The results of the spatial Fourier analysis for the intersection regions defined by the dashed lines in Fig. 5.5 are shown in the second and fourth columns of Fig. 5.5 for the AV and Sat configuration respectively. The symmetry observed in the spatial Fourier maps reflects the symmetry of the normal modes, so it is not surprising that extended lines along the diagonals are observed for the AV case, which occurs because the modes are localized along

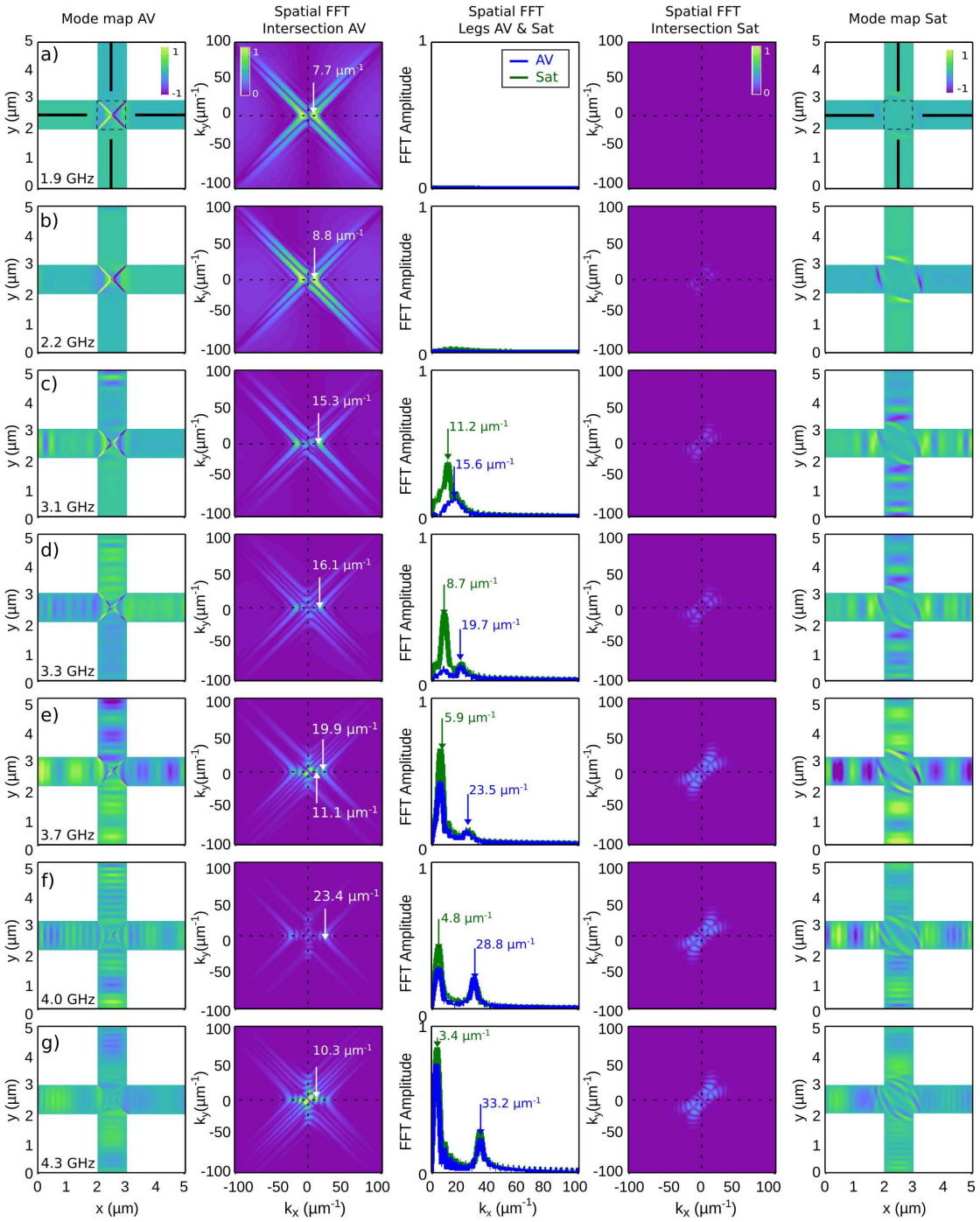

Figure 5.5. Mode maps ($A\cos\phi$) for the AV (far left) and Sat (far right) regions after a 0.1 mT, 30 ps IP excitation. Two dimensional spatial Fourier transforms of the intersection regions defined by dashed lines in the mode maps, are in shown columns 2 (AV) and 4 (Sat). One-dimensional spatial Fourier transform along the black lines in legs for both AV and Sat are shown in the central column. White arrows represent the intersection with the horizontal axis and provide an estimate for the wavevector inside the intersection, directed along the leg k_x.

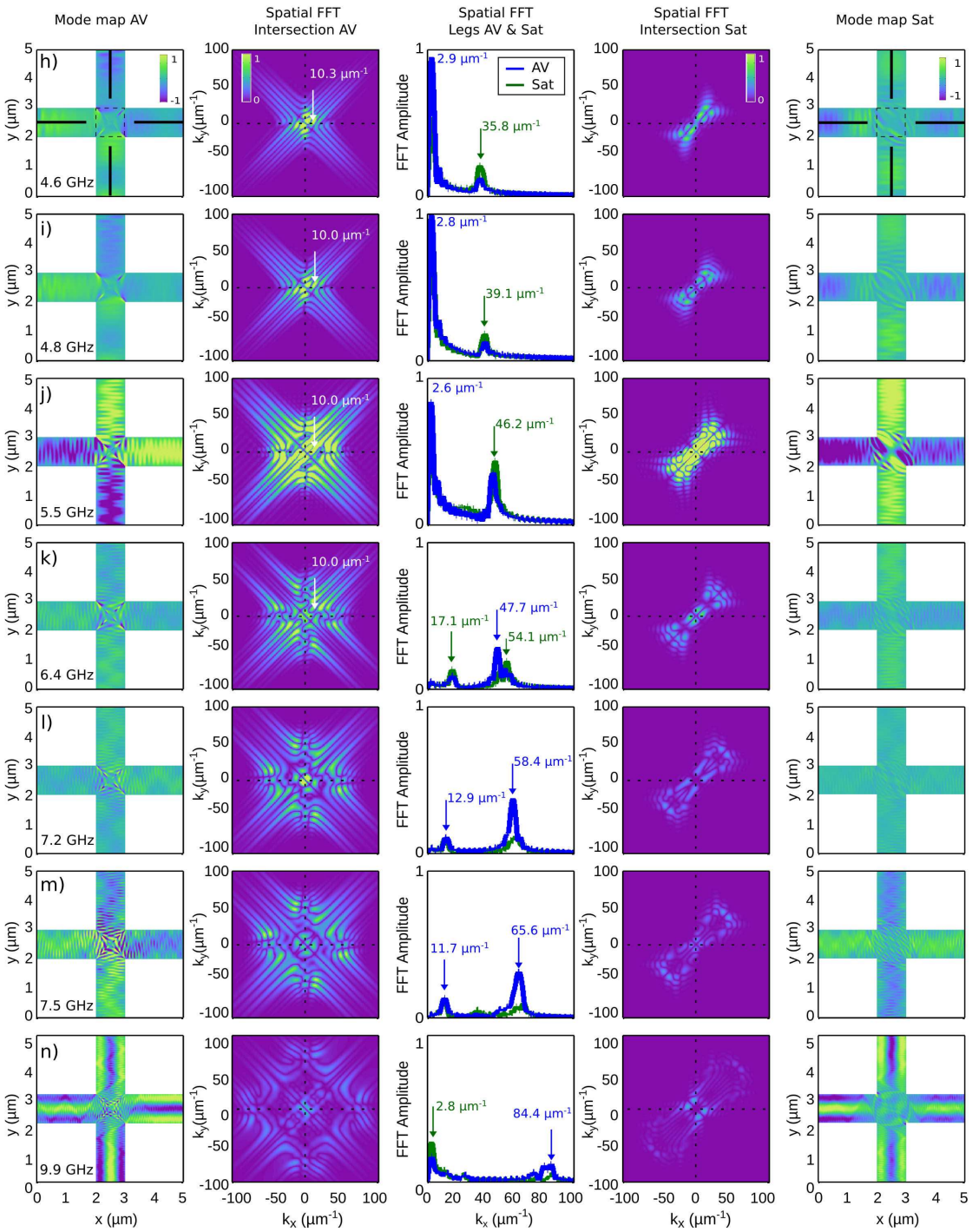

Figure 5.6. Continued from 5.5. Mode maps and Spatial Fourier Transforms after a 0.1 mT, 30 ps IP excitation.

the diagonals. The intersection with the horizontal axis in the spatial Fourier transform is associated with the dominant leg-directed wavenumber in the intersection $k_{x,int}$. These values

and the corresponding wavelengths $\lambda_{x,int}$ are listed in table 5.2. The Fourier plots become more complex for higher frequencies and the number of intersections with the horizontal axis increases, making it more difficult to assign a definite value to $k_{x,int}$.

f (GHz)	$k_{x,int}$ (μm^{-1})	$\lambda_{x,int}$ (μm)	$k_{x,leg}$ (μm^{-1})	$\lambda_{x,leg}$ (AV) (μm)	$k_{x,leg}$ (Sat) (μm^{-1})	$\lambda_{x,leg}$ (Sat) (μm)
1.90	7.7	0.82	—	—	—	—
2.22	8.8	0.72	—	—	—	—
3.07	15.3	0.41	15.6	0.40	11.2	0.56
3.27	16.1	0.39	19.7	0.32	8.7	0.72
3.74	19.9	0.32	23.5	0.27	5.9	1.06
3.97	23.4	0.27	28.8	0.22	4.8	1.31
4.32	10.3	0.61	33.2	0.19	3.4	1.85
4.64	10.3	0.61	2.9	2.17	35.8	0.18
4.81	10.0	0.63	2.8	2.24	39.1	0.16
5.47	10.0	0.63	2.6	2.42	46.2	0.14
6.42	10.0	0.63	47.7	0.13	54.1	0.13
7.15	—	—	58.4	0.11	58.4	0.11
7.47	—	—	65.6	0.10	65.6	0.10
9.93	—	—	84.4	0.07	2.8	2.24

Table 5.2. Dominant leg-directed wavenumbers, obtained from spatial Fourier transform, of the intersection ($k_{x,int}$) and leg ($k_{x,leg}$) regions shown in Fig. 5.5, and corresponding wavelengths ($\lambda = 2\pi/k$).

In addition to the full spatial Fourier transforms of the intersection, transform of the profiles along the legs (black lines Fig. 5.5) were also explored to find the dominant k. The central column of Fig. 5.6 shows spatial Fourier spectra that have been averaged over lines that start 0.5 μm away from the intersection and extend 1.5 μm along the legs. For the two lowest modes the amplitude is basically at the level of numerical noise, as expected, because no activity was observed in the legs for these modes. As the frequency increases some activity can be distinguished. At 3.07 GHz the one-dimensional Fourier spectra along the legs indicate that there is a single dominant wavenumber: 15.6 μm^{-1} for the AV case whereas the dominant wavenumber for the Sat case is 11.2 μm^{-1}. At higher frequencies, additional peaks are observed for both AV and Sat cases. In some cases the dominant Fourier amplitudes change depending on the magnetic state of the intersection. For instance

for the 3.27 GHz mode the high k_x SW mode dominates when the intersection is in the AV state while the lower k_x mode is favoured for the Sat case.

5.3.2. Out-of-plane Excitation

Due to the symmetry of a uniform OOP field, it should not be expected excitation of modes with azimuthal characteristics nor excitation of the gyrotropic mode since an OOP field does not produce displacement of the core. For magnetic vortices, modes in the GHz-range with radial symmetry are observed experimentally [80]. In this section the response of AVs in the pound-key-structure to an OOP excitation are explored. The normalized frequency spectra after the application of a 0.1 mT, 30 ps uniform gaussian pulse are presented in Fig. 5.7 for the AV and Sat regions, and compared to the IP excitation.

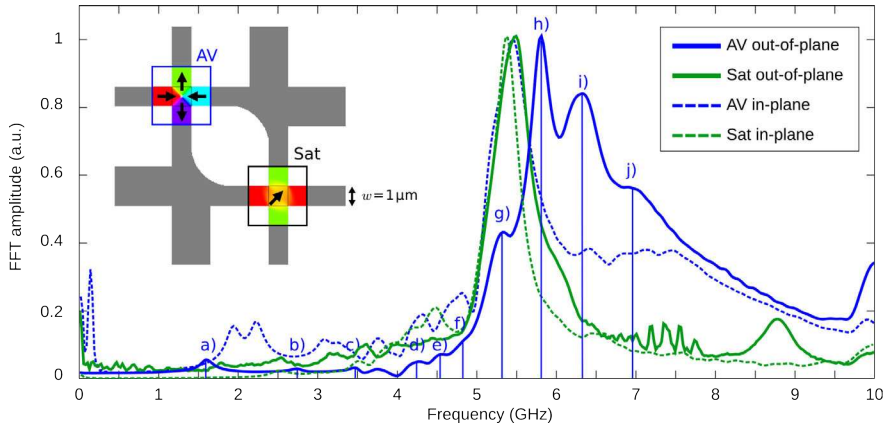

Figure 5.7. Frequency spectra for the out-of-plane (solid lines) and in-plane excitations (dashed lines) for the AV and Sat regions. A 0.1 mT, 30 ps uniform Gaussian pulse was applied perpendicular to the sample plane. The spectra were obtained by averaging the Fourier amplitudes over the AV and Sat intersections (smaller black boxes) and the amplitudes have been normalized to the strongest mode of each spectrum (originally 455.8 and 429.5, respectively, for the OOP case and 1079 and 948.8 units, respectively, for the IP case).

Both states present rich dynamic spectra with low amplitude peaks for f <5 GHz after which a strong response is observed reaching a peak of maximum amplitude at 5.80 GHz for the AV state and at 5.48 GHz for the Sat case. The amplitude decreases gradually with

increasing frequency after that. For AV state, the first resonant peak is located at ∼1.6 GHz, slightly below the first azimuthal mode in the IP spectrum and some weaker, well-separated, peaks are observed in the 2-4 GHz range. Several consecutive sharp peaks are observed in the 7-8 GHz range for the Sat case. Comparisons with additional simulations revealed that the presence of these peaks is rather an anomaly. Even further, observation of the mode maps corresponding to these peaks revealed a checkerboard pattern that is thought to be due to artifacts in the simulations, likely due to the fact that the magnitude of the OOP is relatively small (0.1 mT) but the magnetic susceptibility is lower in the OOP direction as compared to the IP case.

Fig. 5.8 shows the profiles of the normal modes along selected directions, which were calculated in the same way as for Fig. 5.4 for the IP case. The profiles for the OOP modes also exhibit quantization and the indices m and n were used to describe the mode quantization following the same definition as for the IP case. The characteristic wavelengths, obtained following the same procedure as for the IP case via spatial FFT of the normal modes, are presented in Fig. 5.9 alongside the spatial FFT over the intersection region and along the legs in a layout similar to what was used for the IP case (Fig. 5.5).

5.3.3. Discussion of IP vs. OOP results

The results from micromagnetic simulations and mode maps analysis presented so far show that depending on the direction of the excitation field, IP or OPP, different types of AV modes are excited. The lowest frequency modes obtained after an IP excitation are azimuthal-like modes that have circulation around the center with opposite handedness, exhibit an X shape along the diagonals and are localized within the intersection. Meanwhile an OPP pulse excited modes that, similar to the azimuthal ones, have an X shape along the

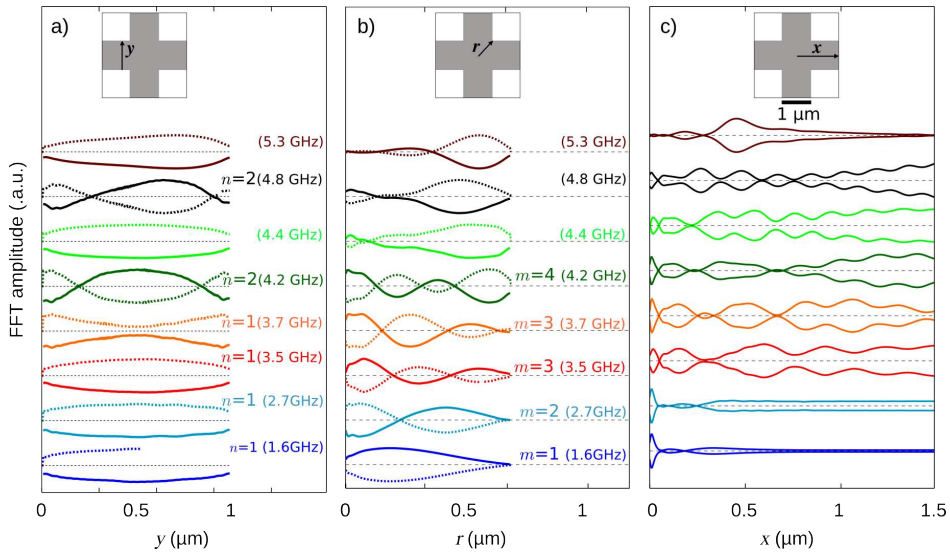

Figure 5.8. Mode profiles along different directions y, r and x as defined in each inset for a region containing an AV. The cuts are one cell wide (4 nm) and have been normalized to the maximum amplitude of each profile. The solid and dashed lines represent $A\cos(\omega t_o + \pi)$ and $A\cos(\omega t_o - \pi)$, respectively, where the later was added for easier visualization of the mode profile. The approximate quantization number of a) the width and b) diagonal modes are labelled using m and n, respectively, based on the number of antinodes.

diagonals and are localized within the intersection, however there is an important difference because in this case the half-diagonals are all in phase and there is no circulation, resembling radial modes of a vortex. The quantization order along the diagonal, n, increases with the frequency for both cases (IP and OOP). The fact that an IP pulse excites modes with circulation while an OOP pulse does not, is related to the fact that the static spin state experiences a torque that leads to differing relative phases along the diagonals for the two excitations. From a perspective of potential applications, the interaction of circulating modes with propagating SW's coming in from the legs could potentially be used to redirect incoming SW's preferentially towards one of the legs which may be useful for circulator devices.

Now, the propagation in the legs is examined in more detail. To facilitate the comparison of the results from IP and OOP excitations, the remaining discussion focused on a few selected AV modes for each type of excitation. These modes are specified in figure 5.11

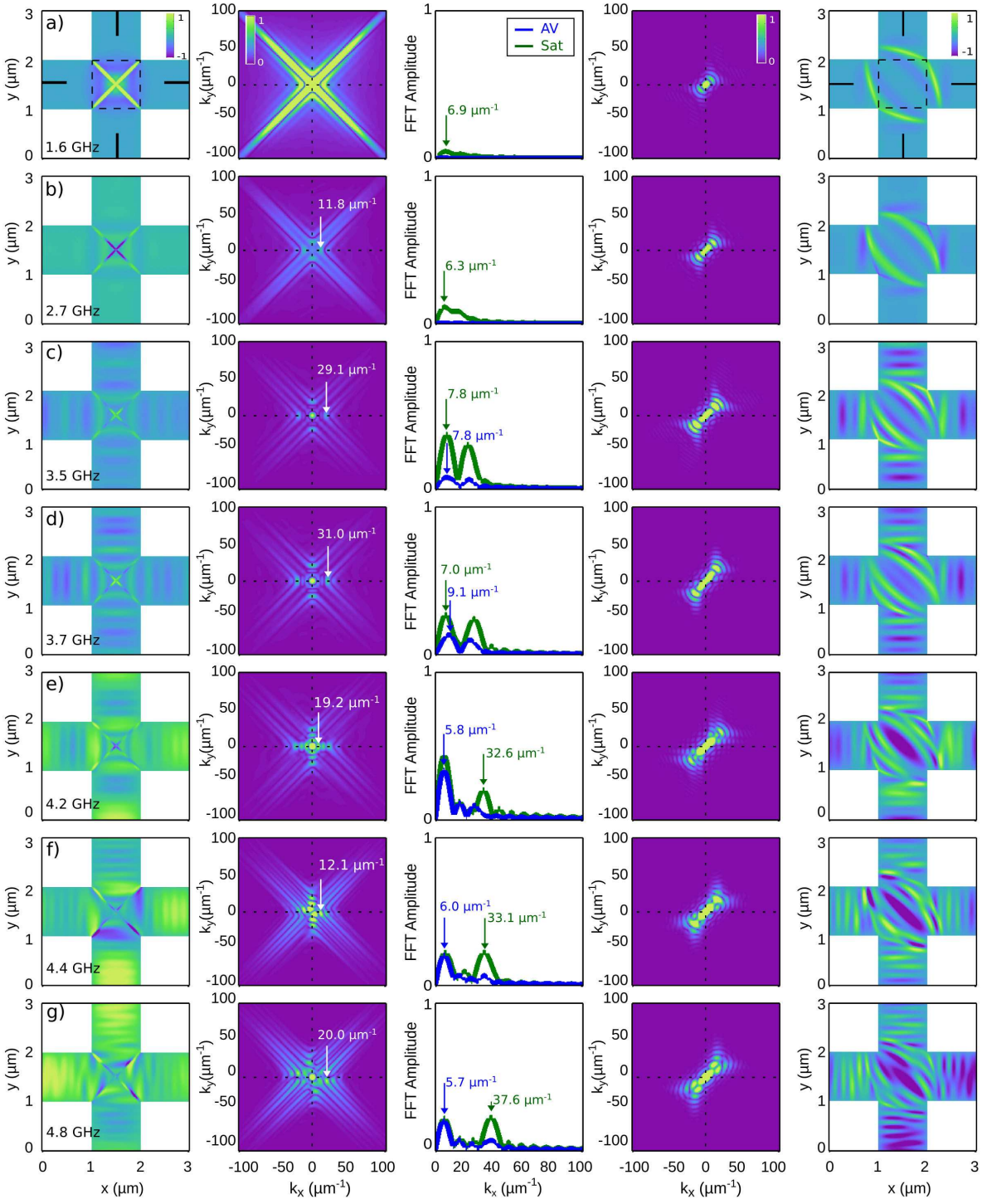

Figure 5.9. Mode maps and Fourier transforms after a 0.1 mT, 30 ps OOP excitation. The figure layout follows that of Fig. 5.5.

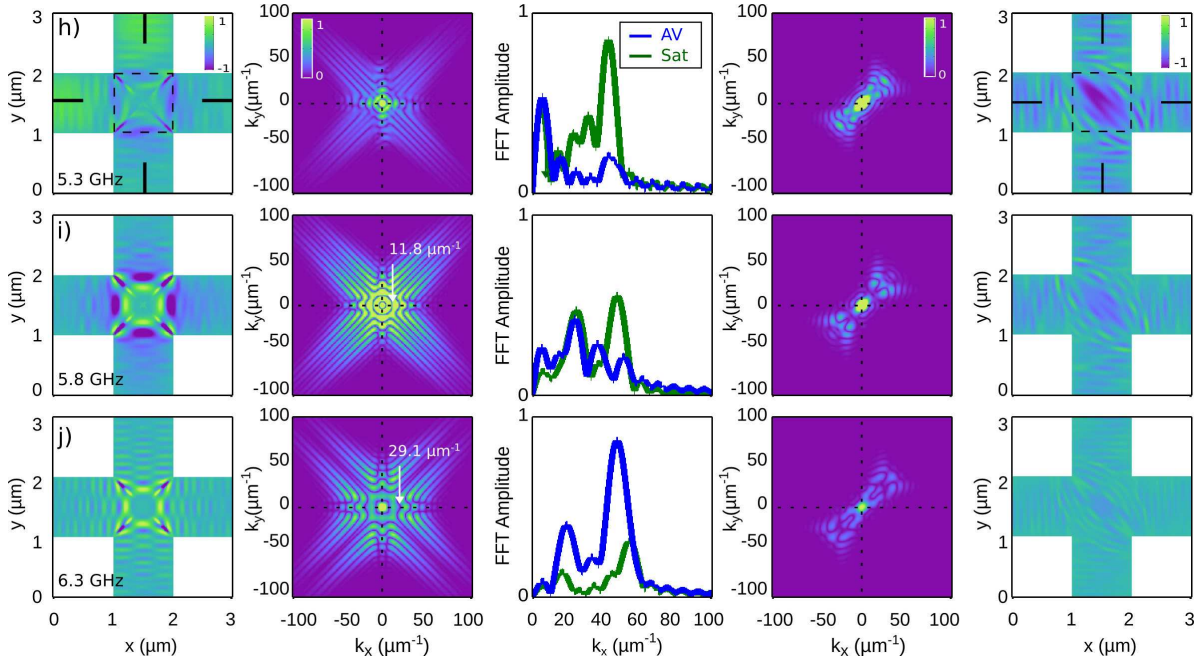

Figure 5.10. Continued from Fig. 5.9. Mode maps and Fourier transforms after a 0.1 mT, 30 ps OOP excitation.

where the spectra for the IP excitation are the same as those presented in Fig. 5.2 and the spectra for the OOP excitation were obtained by using an infinitely long 0.5 mT uniform field, applied perpendicular to the sample and relaxing to equilibrium after removing the field. This long pulse produced a response very similar to that obtained with a short pulse except for an enhancement in the excitation of the first mode and also helped to avoid numerical artifacts, details of the comparison between short vs. long pulse are presented in section 5.3.5. The frequencies and quantization characteristics for these modes are shown in Table 5.3.

No significant response in the legs was observed for any of the lowest-frequency modes f_{1a}, f_{1b}, f_{r1}, and f_{r2} (see Figs. 5.5a and 5.9a), however the results for higher frequencies show that in some cases the magnetic state of the intersection (AV or Sat) affects the dynamic response in the legs for both excitation directions. For example, for the azimuthal mode f_{2b} the AV state exhibits a shorter wavelength in the legs ($\lambda \sim 0.33$ μm) as compared to the Sat

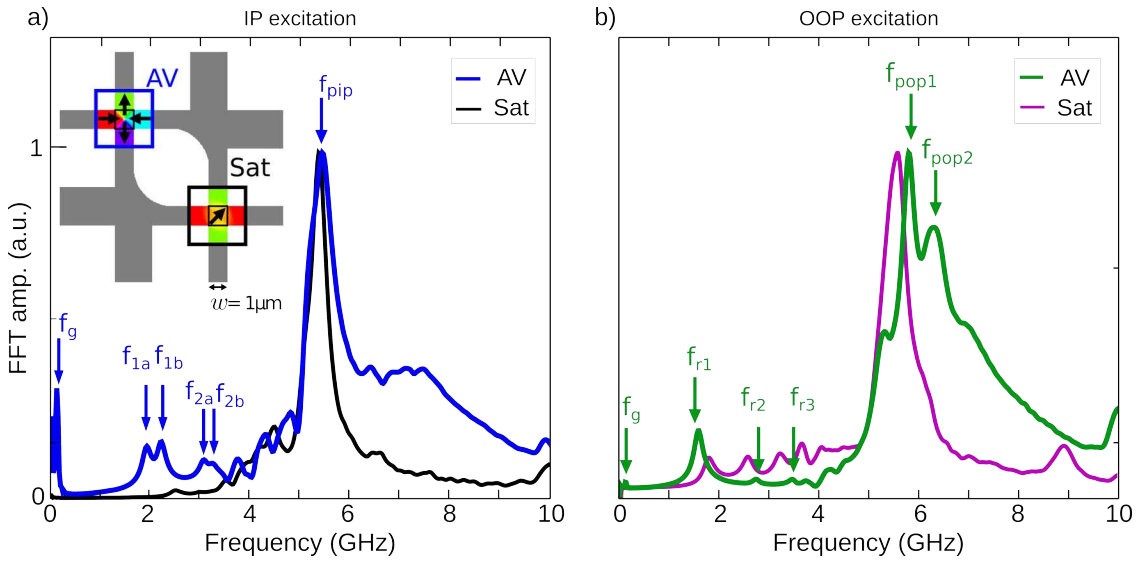

Figure 5.11. Spectra obtained for AV and Sat magnetic states in response to a) IP and b) OOP excitations. The small squares in the intersections indicate the regions over which the Fourier amplitude was averaged to obtain these spectra.

mode	f (GHz)	n	m (AV)	m (Sat)	description	excitation
f_{1a}	1.90	1	1	1	azimuthal	IP
f_{1b}	2.22	1	1	1	azimuthal	IP
f_{2a}	3.07	2	1	1	azimuthal	IP
f_{2b}	3.27	2	1	1	azimuthal	IP
f_{pip}	5.47	4	2	2	prominent	IP
f_{r1}	1.59	1	1	1	radial	OOP
f_{r2}	2.75	2	1	1	radial	OOP
f_{r3}	3.48	3	1	1	radial	OOP
f_{pop1}	5.80	3	3	2	prominent	OOP
f_{pop2}	6.32	3	3	2	prominent	OOP

Table 5.3. Selected modes and quantization values along the half-diagonal (n) and across the leg width (m).

state ($\lambda \sim 1$ μm) as can be seen from the mode maps in Fig. 5.5d and animations of this mode (see supplementary material in[18]) reveal that SWs propagate in opposite directions along the legs for AV and Sat states. The values from the spatial FFT (central column of the same figure) confirms that at this frequency there are two different k_x's for both states (11.1 and 19.9 μm^{-1}) and that the lower k_x is almost completely suppressed for the AV while for the Sat is the higher k_x that prevails. This preference towards a particular higher or lower

k_x, based on the magnetic state of the intersection, is a general characteristic that is also observed in the other modes excited with either an IP or OOP field.

To the best of our knowledge no analytical theory currently exists that can be used to predict the frequencies and mode profiles of the AV resonances, however the legs are longitudinally magnetized microstrips and hence it is instructive to examine the leg dynamics in the context of BV SW. Dispersion curves for this configuration (BV), assuming infinitely long elements and material parameters listed in section 3.3, were calculated following references [88, 87] for a width of $w = 1$ μm. The first three width-quantized BV dispersion curves are shown in Fig. 5.12 along with simulation values of f and k_x (symbols), extracted from the central column of Figs. 5.9 and 5.5 for both the AV and Sat states, respectively. The dispersion curves show that there is a minimum frequency f_{min} at around 3 GHz below which no SW's are allowed in the legs. This is consistent with the fact that no significant leg activity is observed for the f_{1a}, f_{1b}, f_{r1}, and f_{r2} modes. There are simply no allowed SW modes within the legs at these frequencies. At the minimum frequency $f_{min} = 3.07$ GHz the dominant k_x of AV and Sat, for the IP excitation, line-up well with the calculated first width-quantized BV dispersion curve (m=1) and k_x for AV and Sat lie on sides of the dispersion curve that have opposite slope and therefore opposite group velocity. This is consistent with what is observed in the animations of the corresponding mode maps ([18]) where SW's travel outwardly from the intersection for the AV state and inwardly for the Sat state. There is a general good agreement between the values extracted from the simulations for frequencies $f > f_{min}$ and points in the calculated dispersion curves that correspond to propagating spin waves.

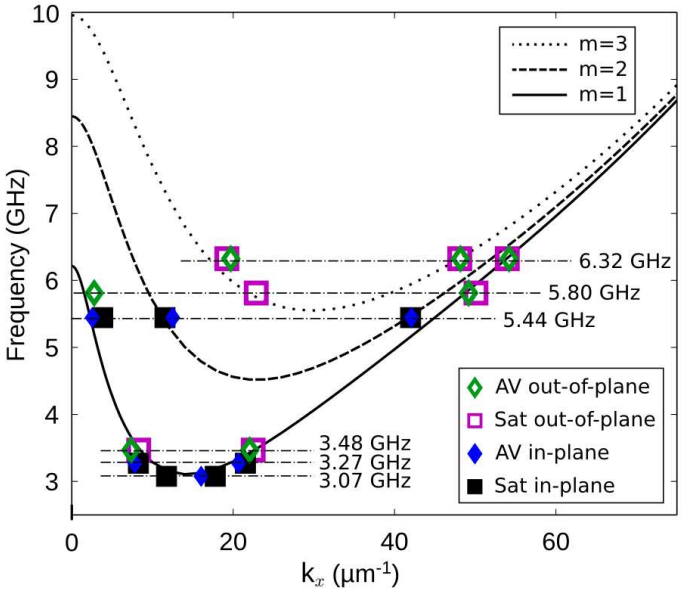

Figure 5.12. Dispersion curves for backward volume geometry (curved lines), calculated as in [88, 87] assuming infinitely long elements for a width of $w = 1$ μm and simulation results (symbols) for the leg-directed k's of the different AV modes after an IP and OOP excitation (see Figs. 5.5 and 5.9).

Despite agreement, the dispersion curves do not explain why the spin state favors one particular k_x over the other and information from the mode maps might help to understand this process. For example, for the f_{2a} mode, it can be seen from Fig. 5.5d that the leg-directed component of k_r inside the intersection, $k_{x,int}$=16.1 μm^{-1}, (see Table 5.2) is closer to the highest of the two possible k_x's in the legs (8.7 and 19.7 μm^{-1}) for the AV state while this is not the case for the Sat state. The analysis of the mode maps can also help to explain the transition in leg quantization from m=1 to 3 for the AV modes (OOP excitation). Since the response of the diagonals for f_{r2} and f_{r3} AV modes is in-phase, they couple naturally to $m = 1$ propagating modes, however for f_{pop1} and f_{pop2} the three-fold quantization between the diagonals favors coupling to modes with $m = 3$. The f_{pop1} and f_{pop2} AV and Sat modes differ not only in width quantization (m=3 and 2 respectively) but also in dominant k_x in the leg.

On a different aspect, the extended micro-wires of the pound-key geometry, compared to an astroid, offer the possibility of propagating BV SW's from the intersection to the legs or vice versa, or of use in devices where spin waves are generated elsewhere but where control at the intersection is desired. Since the static spin configuration is such that the spins bend smoothly from any given leg into the two orthogonal legs at the intersection, fan-in, fan-out operations are possible. Furthermore, since the intersection spin state can be easily erased or reset using an external magnetic field, reconfigurable devices can be constructed.

5.3.4. Size dependence

Since the frequencies of vortex modes change as a function of structure size, the effect of changing the dimensions of the sample on the frequency spectra of the AV modes was also investigated. The overall width of the samples was varied using w=3, 6, and 12 μm (field excitations of 0.50, 0.25, and 0.10 mT respectively) and maintaining a constant thickness t=37 nm. The results obtained for the spectra of AV modes are presented in Fig. 5.13a-b for an IP and OOP field excitation respectively. In both cases a systematic shift of the spectra toward higher frequencies is observed as the w is reduced but many of the overall characteristics are otherwise similar. Inspection of the mode maps (see appendix D) to make sure that the frequencies in the spectra corresponded to the spatial features and symmetries of each mode allowed us to track them as a function of the sample aspect ratio $\beta = t/w$ and the results are shown in Fig. 5.13c. An almost linear trend was observed for all of the modes, with the frequencies increasing as a function of β. The splitting of the n=1 azimuthal modes (f_{1a}-f_{1b}) is slightly larger than for the $n = 2$ pair (f_{2b}-f_{2a}) but both modes are split by an amount larger than the gyrotropic frequency for all β, similar to what is reported for azimuthal vortex modes [89] for which the splitting mechanism involves hybridization of

the gyrotropic and the azimuthal modes. Given the similarities in magnitude for the AV azimuthal modes with those of vortex states, the splitting mechanism might be the same.

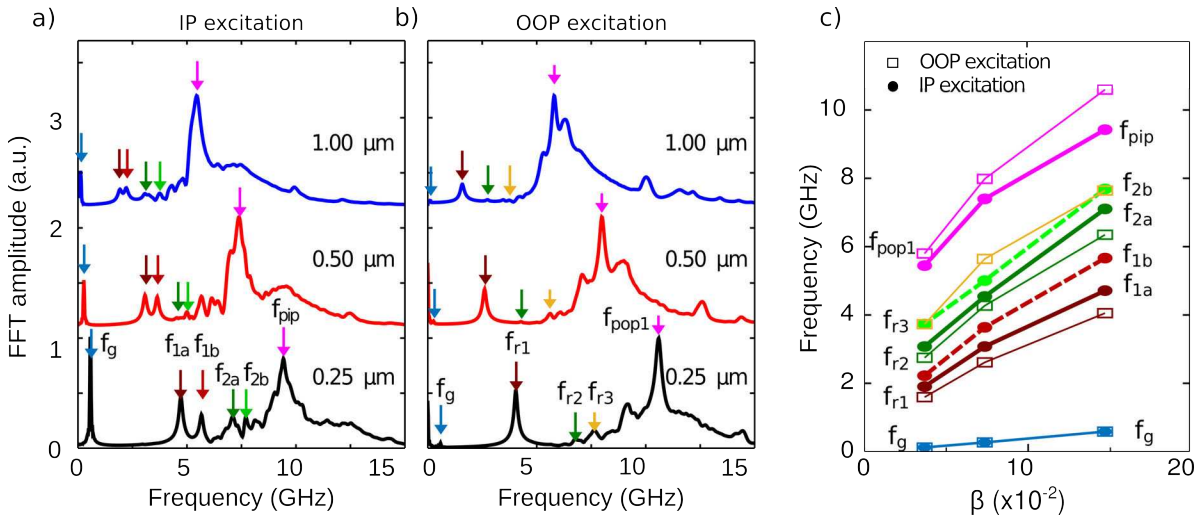

Figure 5.13. Frequency spectra obtained for different sample sizes w, after a) an IP pulse and b) OOP pulse were applied. The dependence of the frequency of selected modes with the aspect ratio (β=thickness/width) is shown in c). The amplitudes of the excitations were 0.50, 0.25, and 0.10 mT for samples with w=3,6, and 12 μm respectively.

5.3.5. Effect of pulse duration

In this section we explore how the duration of the field or the type of excitation (pulsed vs. continuous wave) affects the dynamic response of the AV structure. Simulations were performed comparing the dynamic response of the system after the application of:

1) Long excitation, where the initial state was first relaxed under a 0.5 mT uniform magnetic field applied along the main diagonal (45 degrees w.r.t. the horizontal axis). After equilibrium was reached, the magnetic field was removed and the subsequent magnetization dynamics were recorded;

2) Short pulse, where the time-evolution of the magnetization was recorded after a spatially uniform 0.1 mT Gaussian magnetic field pulse with FWHM of 30 ps. The pulse was

applied along the main diagonal at time t=1 ns as shown in Fig. 5.1b. The motivation to use a short pulse was to reduce the response of the gyrotropic mode and focus on the higher frequency modes instead. The basic reasoning is that if the pulse duration is short enough the vortex core will not be displaced as far from the equilibrium position as it would with a long pulse therefore the reducing the duration of the gyrotropic mode, i.e reducing the amount of time that core will takes to return to its equilibrium position, and the its Fourier amplitude as well. Also, the reason to chose a lower amplitude for the pulsed magnetic field as compared to the long excitation is because the abrupt ($\Delta t \to 0$) removal of the magnetic field does, in principle, excite all modes of the spectrum ($\Delta f \to \infty$), that are allowed by the symmetry of the excitation, and the power is in that case expected to be distributed over a larger number of modes;

3)Driven excitation, where a 0.1 mT microwave field is swept through different discrete frequencies of the spectrum. This is similar to how many experiments are done and should, in principle provide a cleaner mode map because only the mode matching the excitation frequency should be excited and there should be no contribution from other resonant modes.

As a general rule the comparison of the different excitations was done for small samples (w= 252 nm) while for bigger samples (w=1 μm) only short pulsed fields were used, to save on computational time. For the OOP case, since it does not displace the vortex from its equilibrium position it should not, in principle, excite the gyrotropic mode and there is no need to use short pulses, however for comparison purposes a test simulation was run with 0.1 mT excitation field applied perpendicular to the sample.

In all three situations, the magnetic field was spatially uniform and applied along the diagonal of the sample for the IP case and perpendicular to the plane of the sample for the

OOP case. The amplitude of the magnetic field was kept low enough to avoid destroying the AV state and to ensure that we were in the linear regime. The simulations were done on a smaller sample (w = 252 nm and thickness 37 nm) to save on computational time and the results are shown in Fig. 5.14. The spectra were obtained by averaging the Fourier amplitude over the AV intersection region (black square box in figure 5.1).

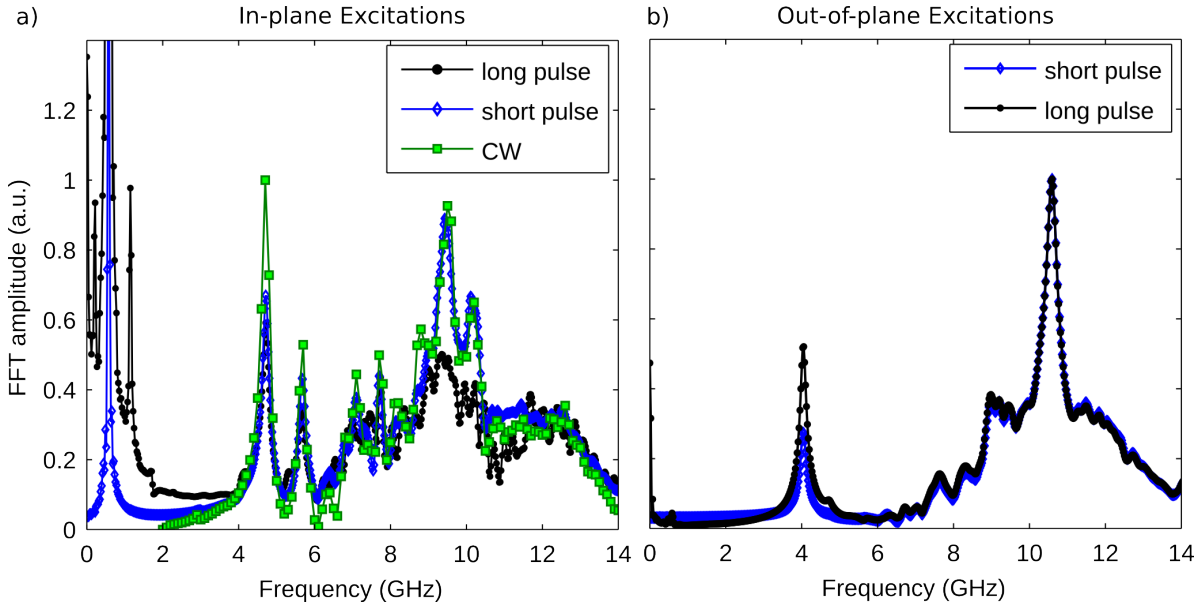

Figure 5.14. Spectra obtained after excitation fields applied a)IP and b)OOP. The width of the narrow leg was w=252 nm and the thickness was 37 nm.

The general characteristics of the spectra for IP excitation (Fig. 5.14a) are very similar for all of the excitation methods with two well-defined, prominent peaks in the low frequency part (4.7 and 5.7 GHz) and a broad region of activity at higher frequencies with several peaks that overlap. There are some noticeable differences between the responses to a long and short pulse excitations that could be related to the fact that the short pulse excites the low frequency gyrotropic mode with a lower amplitude than the long pulse, and consequently interference from this mode is less likely. The number of points in the CW spectra is lower than for the other two cases, because the procedure used for this case required to

magnetization to reach a steady state at a given frequency before moving on to the next frequency value and a bigger frequency step was chosen to save on computational time. The low frequencies in the CW excitation ($f < 2$ GHz) were also avoided for the same time-saving considerations. The response to a CW and a short pulse IP excitation are very similar and justifies the decision to use short pulses instead of CW. For the OOP case, the long pulse is slightly more efficient in exciting the low frequency mode around 4 GHz, and a minor secondary peak around 4.7 GHz can also be observed. The overall agreement, however, also gives us the confidence to compare different results obtained using either excitation.

5.4. Conclusions

Micromagnetic simulations were conducted on magnetically-soft pound-key-shaped structures, containing AV and Sat states in the intersections of narrow legs, to investigate the high frequency dynamics of a magnetic AV. It was found that the AV state exhibits modes of gyrotropic and azimuthal character for an IP excitation, and radial-type modes for an OOP excitation, where the lowest frequency modes localized in the intersections while higher frequency modes couple to propagating spin waves in the structure legs. The wavevectors of such leg modes are consistent with calculations of BV SW dispersion curves in long microstrips, however, the particular mode that is excited is influenced by the magnetic state of the intersection and the relevant length scales, which offers new possibilities of spin wave generation and manipulation on the nanoscale.

CHAPTER 6

Tri-disk System

Magnetic vortices are often found in micron- and submicron-sized patterned structures, such as disks or squares, that are magnetically soft [90, 67]. For cylindrical samples of appropriate thickness to diameter aspect ratio [8], the vortex represents the ground (lowest energy) state and has a spin distribution such that, at remanence, the spins curl smoothly describing concentric circles around the central core, as illustrated by the black arrows in Fig. 6.1a.

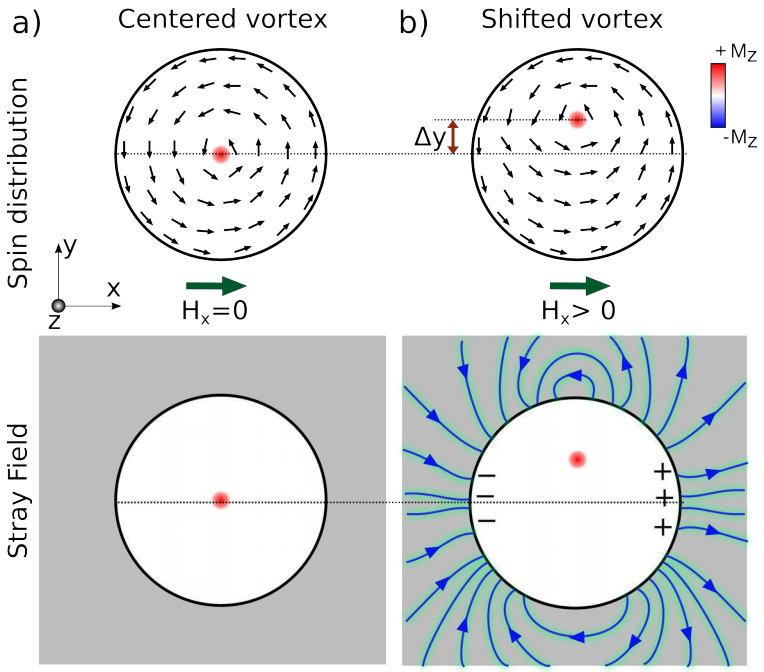

Figure 6.1. Spin distributions of a vortex in a disk are shown in for the case when a) No external field (green arrow) is applied and the vortex core is at the center of the disk and b) when an external field H_x¿0 is applied along the x-direction producing a shift of the core in a perpendicular direction by an amount Δy. This creates magnetic side-surface charges (+/− symbols) and stray fields as illustrated in bottom row.

Near the edge the spins are aligned parallel to the disk rim, therefore there are no side-surface magnetic charges that generate demagnetizing fields and in consequence the

magnetostatic energy is minimized. In addition, having adjacent spins aligned almost parallel to each other minimizes the exchange energy. At the center the spins can not longer align parallel to each other while simultaneously being in the plane of the disk so they tilt OOP to minimize the exchange energy and avoid a singularity. Other energy contributions, such as Zeeman or magnetocrystalline are either zero or small and hence ignored. Since the energy is an even function of the magnetization the different values of the chirality ($\chi = \pm 1$) and polarity ($p = \pm 1$) produce the same total energy therefore the vortex is a double-degenerate state.

Consider now a situation where an external magnetic field is applied to a vortex. As a result, the core is shifted from its static equilibrium position in a direction perpendicular to the external field as shown in Fig. 6.1a, the in-plane magnetization will no longer exhibit flux closure and a net magnetization will develop along the direction of the external field leading to magnetic charges on the side surfaces and the appearance of stray fields around the structure. If a second structure is placed in close proximity to the first one, vortices can interact dynamically with one another via magnetostatic interactions. Coupling of magnetic vortices has been investigated for pairs [91–93], linear chains [19], and for 2-D arrays [94, 95, 92, 96–99, 21, 100]. These effects include splitting of the resonant frequency into two distinct modes for the case of a vortex pair, the frequencies of which depend on the vortex polarities[92].

Coupling effects are important for a variety of applications including vortex-based magnonics [100], for increasing the signal from vortex-based spin torque oscillators [101, 33], and they may also lead to new devices since it was recently shown that the dependence of the resonance frequencies on the polarities can be used as means to dynamically control and read out the polarization state of coupled vortices [102].

In this chapter, I compare the results obtained using micromagnetic simulations to an analytical theory of vortex dynamics that includes magnetostatic interaction to determine the extent that the analytical expressions can be used to predict the behavior of interacting vortices. The majority of contents presented here have been published in [23]. Also, I have contributed to an experimental paper based on time resolved X-ray Photoemission Microscopy (TR-PEEM) measurements [24] on a similar system consisting of three Permalloy disks with radii of R= 2 μm. In the sections below I will describe my work on simulations of coupled magnetic vortices.

6.1. Background

Attempts to describe the magnetostatic interaction between magnetic vortices analytically are usually based on different models for the magnetization distribution of a vortex while being shifted from its equilibrium position, including the "rigid vortex" [103] and poles-free (a.k.a. two-vortex, surface charge free) models [78, 8] as limiting cases. The rigid vortex model assumes a particular magnetization distribution [104] that does not deform as the vortex is displaced from the equilibrium, maintaining circular symmetry around the core. Such a model overestimates the gyrotropic frequency and the inter-disk coupling energy therefore does not describe the vortex dynamics adequately, however it is a simple model and its accuracy improves for short inter-disk separations. The poles-free model assumes the existence of an additional, virtual, vortex located outside of the disk and allows deformation of the magnetization distribution with small surface charges on the top and bottom surfaces, near the vortex core, and no surface charges at the edges of the disk. Comparison of these two models against micromagnetic simulations [78] show that the rigid vortex model tends

to overestimate the gyrotropic frequency while the poles-free model provides a more realistic description of the low frequency dynamics.

6.1.1. Thiele's equation

In general, the dynamics of magnetic textures, including vortices, can be obtained by integrating the LLG equation. However this usually involves solving a system of non-linear coupled differential equations of non-local variables and simpler approaches are often preferred, because by using simple analytical expressions to express the physics of a system one can gain a great deal of insight into its behavior, as demonstrated by models such as the harmonic oscillator or the ideal gas frequently used in physics. One such simple approach, for the magnetization dynamics, was formulated by Thiele [105], who expressed the problem in terms of forces acting on a domain wall. This description was later applied to magnetic vortices [106], and it has henceforth served as the basis for most models of vortex dynamics. In the case of confined geometries such as thin disks, the Thiele equation can be written as [78]:

$$\mathbf{G} \times \frac{d\mathbf{X}}{dt} + \mathbf{F} = M\frac{d^2\mathbf{X}}{dt^2} \tag{6.1}$$

where $\mathbf{X} = (X, Y)$ is a vector that describes the position of the core of a magnetic vortex, M is the mass tensor and for a single vortex it is diagonal: $M_{ij} = M_o\delta_{ij}$. The term $\mathbf{G} = -G\hat{\mathbf{z}}$ is known as the gyrovector and the gyroconstant G is defined as $G = 2\pi M_s t\gamma p\chi$ where t is the thickness, M_s is the saturation magnetization, p is the core polarity ($p = \pm 1$), χ is the vorticity ($\chi = +1$ for a vortex), and γ is the gyromagnetic ratio. The force vector $\mathbf{F}$ is defined in terms of the potential energy U of the shifted vortex, which in general includes

contributions such as exchange, magnetostatic, Zeeman and anisotropy energy, such that $\mathbf{F}(\mathbf{X}) = -\nabla U(\mathbf{X})$. Thiele's equation assumes that the vortex configuration remains rigid (no distortion) during its displacement although non-rigid models have also been used [78]. In addition, a damping term $\hat{D}\frac{d\mathbf{X}}{dt}$ can also be added to eq. 6.1, where $\hat{D}$ is known as the damping tensor [107].

From an analytical perspective Thiele's equation (6.1) describes the dynamics of a magnetic vortex in terms of the collective coordinates of its core $\mathbf{X}$. The first term represents a Magnus-like force that acts on the vortex in a direction that is perpendicular to its velocity, also referred to as gyroforce. The second term acts as a restoring force directed towards the center of the disk and it is mainly due to the increase in magnetostatic energy of the shifted core. For small displacements of a vortex from its central equilibrium position $\mathbf{X} = 0$, the interplay between the restoring and gyroforce gives rise to a spiraling motion, also known as the gyromode, with a characteristic resonance frequency f_o, as illustrated in Fig. 6.2. The brown line in Fig. 6.2a indicates the path that the shifted vortex core follows, at remanence, towards its equilibrium position after being shifted by a 5 mT magnetic field. The time-evolution of the in-plane components of the magnetization exhibit a damped sinusoidal behavior (Fig. 6.2b) with a gyrotropic frequency $f_o = 680$ MHz as evidenced by the Fourier spectrum shown in Fig. 6.2c. This gyromode can be described as the oscillation of a harmonic oscillator [108].

6.2. Method

To study the dynamics of interacting magnetic vortices in a system of three Permalloy disks in an equilateral-triangle arrangement (Fig. 6.3) micromagnetic simulations using

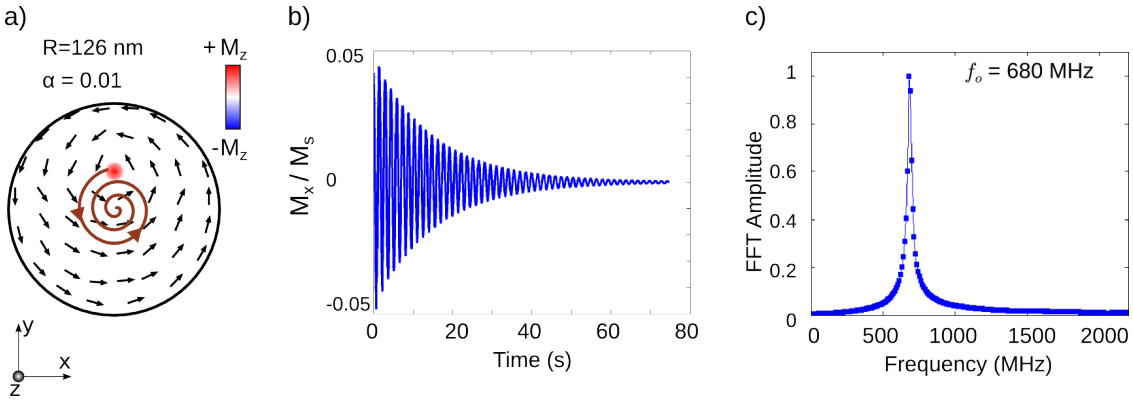

Figure 6.2. Micromagnetic simulations of gyrotropic mode in a single disk (thickness 20nm). The spin configuration (black arrows) and spiral trajectory (brown line) that the shifted core will follow towards its equilibrium, after a H_x=5 mT field is turned off, are shown in a). Damped sinusoidal oscillation of in-plane component of the magnetization is shown in b) for normalized M_x. The Fourier spectrum of M_x in c) shows a single resonant frequency f_o at ∼680 MHz.

OOMMF were performed. Disks with fixed radius R = 126 nm and thickness t = 20 nm but variable inter-disk center-to-center separation D were considered. Material parameters typical for Permalloy were used, saturation magnetization $M_s = 8.6 \times 10^5$ A/m, gyromagnetic ratio $\gamma = 1.76 \times 10^{11}$ $s^{-1}T^{-1}$, exchange stiffness constant $A = 1.3 \times 10^{-11}$ J/m, and magnetocrystallyne anisotropy was neglected. A variety of combinations of vortex polarities p and chiralities χ were examined for the case R/D=0.45, which corresponds to D=280 nm for R=126 nm. The dependence of the resonant frequencies on D was simulated for selected p and χ combinations for R/D ranging from 0.20 (D=630 nm for R=126 nm), which corresponds to the situation where the disks are far enough apart that the magnetostatic interactions are small (edge-to-edge separation of 378 nm), up to R/D=0.49 where the disks are almost touching each other (edge-to-edge separation is only 4 nm). A static magnetic field of μ_oH=5 mT was initially applied along the direction connecting two disks centers (x-direction) using a large damping parameter α=1 for fast convergence, after the system reached equilibrium the field was abruptly removed and the dynamics were modeled using

a realistic damping coefficient α=0.01. Additional simulations were conducted for selected configurations with α= 0.001 to construct spatial profiles of the individual eigenmodes. Using such small value for α implies longer simulation time however it does also reduces the amount of mode overlap and hence it helps to get cleaner mode profiles.

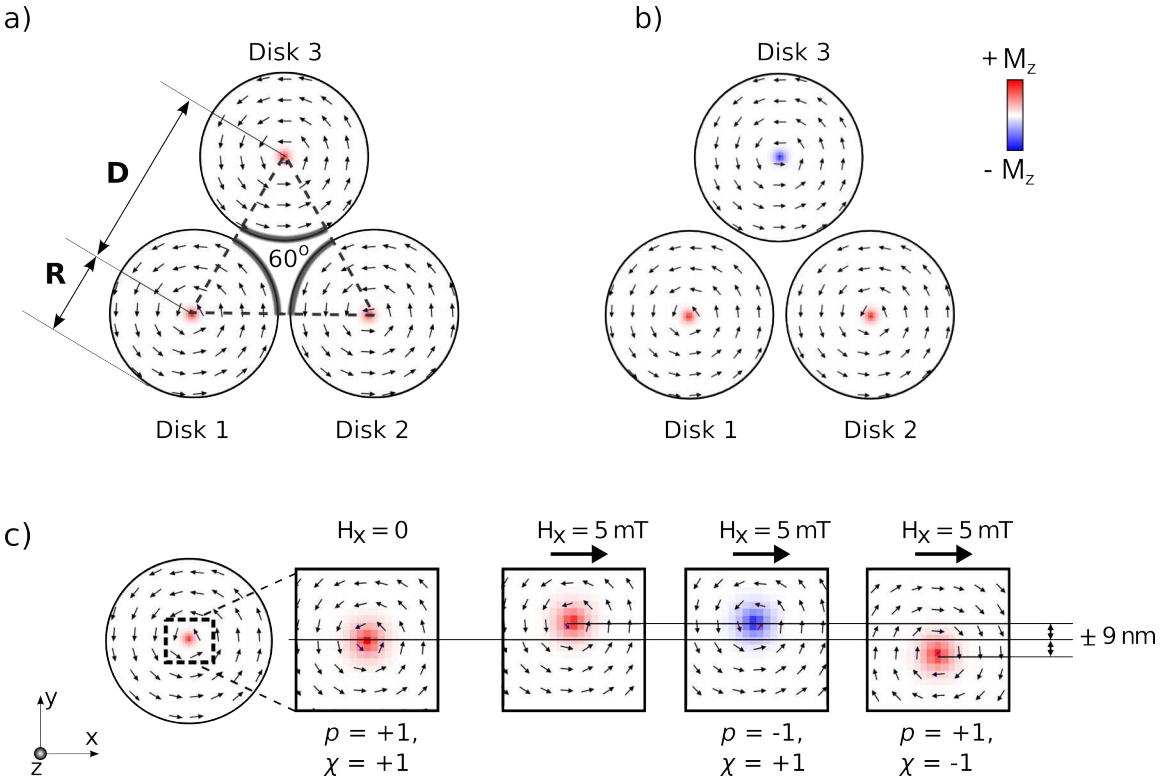

Figure 6.3. Three magnetic disks of radius R are arranged such that they form an equilateral triangle with inter-disk separation D. Black arrows represent the direction of the spins in the plane of the disk, while the out-plane direction is indicated by the red /blue colors. The case where all polarities are the same (p=+1) and where one polarity differs from the others (p=-1) are shown in a) and b) respectively. c) The vortex core shifts along ±y depending on the chirality when a static field H_x is applied along the x-direction.

Simulated spin distributions of the magnetic vortices, in the equilateral-triangle arrangement, for different combinations of core polarities are shown in Fig. 6.3, where all three disks have the same polarity in 6.3a and one polarity is opposite to the others in Fig. 6.3b. The initial positions of the vortices and consequently the initial phase of the vortex oscillations depend on the chirality but not the polarity as illustrated in 6.3c; where a magnetic field

applied in the positive x-direction causes the core to shift in the +y (-y) direction when χ=+1 (-1).

6.3. Results

Fig. 6.4 shows the time-evolution of the magnetization of each disk, of the equliateral-triangle set, and the corresponding Fourier spectra for a variety of polarity combinations and fixed, identical chirality for R/D=0.45. For this separation, the disks are close enough together to observe measurable splitting of the resonances. The disks in the right column of Fig. 6.4 have core polarities opposite to those in the left column. In general, the responses for each of the disks show multiple resonances and the details of the temporal responses vary with the choice of polarity; however, Fourier spectra show particular sets of dominant frequencies: those associated with disks that have all the same polarity and those with one polarity reversed. When p and χ and are all the same (Figs. 6.4a and 6.4b), two frequencies are observed: a dominant resonance at 630 MHz, slightly lower than that of a single disk f_o and a weaker resonance at 690 MHz. The same spectral response and overall temporal characteristics are present for other χ combinations as well (not shown). The vortex cores all gyrate with the same handedness since the polarities are the same and hence close-to-constant core separations are maintained at all times. In contrast, when one of the disks has a polarity that is opposite to the others, three distinct resonant frequencies are observed at 600, 660, and 750 MHz (Figs. 6.4c,e,g and 6.4d,f,h) and pronounced beating patterns are detected in the time domain.

For a given confiifguration, the core with the opposite polarity will gyrate with opposite handedness compared to the others, leading to variations in the separation between the cores

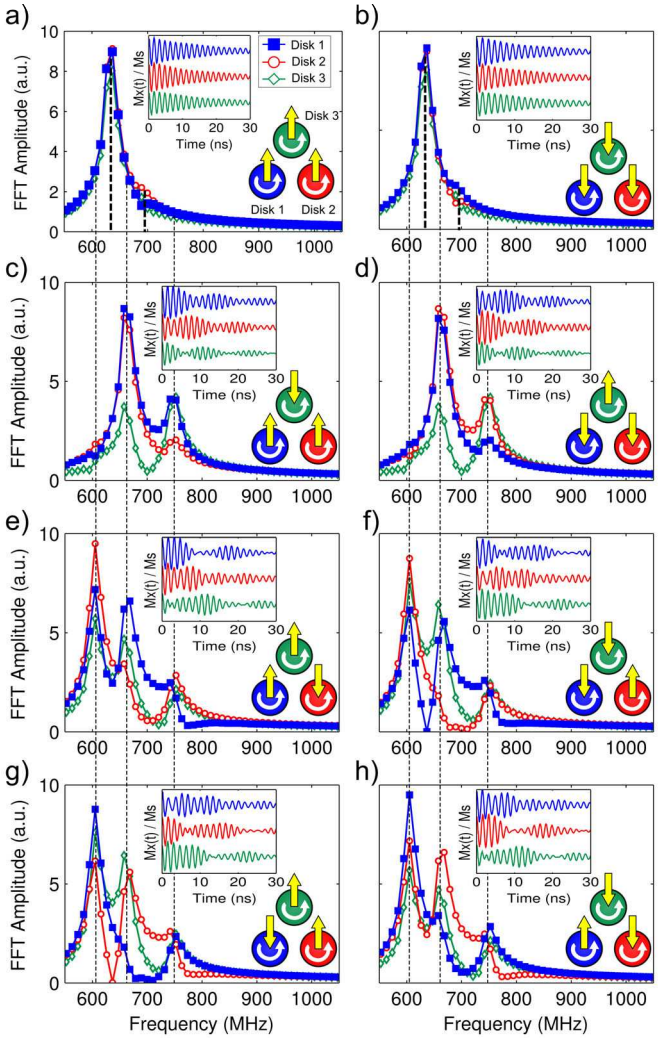

Figure 6.4. Micromagnetic simulations of three interacting disks with R/D =0.45 for a variety of p (vertical arrows) and fixed, identical χ (curved arrows). Fourier transforms of the x-component of the volume-average magnetization M_x of each disk are shown. The insets show M_x as a function of time. In all cases, the maximum amplitude of the oscillations is $M_x/M_s \sim 0.1$. When p are (a) all up and (b) all down, a strong resonance at 630 MHz as well as a weaker resonance at 690 MHz are observed, whereas three resonances of 600, 660, and 750 MHz are observed when one core is down and the others are up ((c), (e), and (g)) or one is up and two are down ((d), (f), and (h)).

and more complex temporal interactions. The phases and the relative mode amplitudes and hence the details of the temporal patterns depend on the exact p and χ configuration, but the frequencies depend only on the relative p of the three cores. No significant effect due to χ was found as shown in Fig. 6.5.

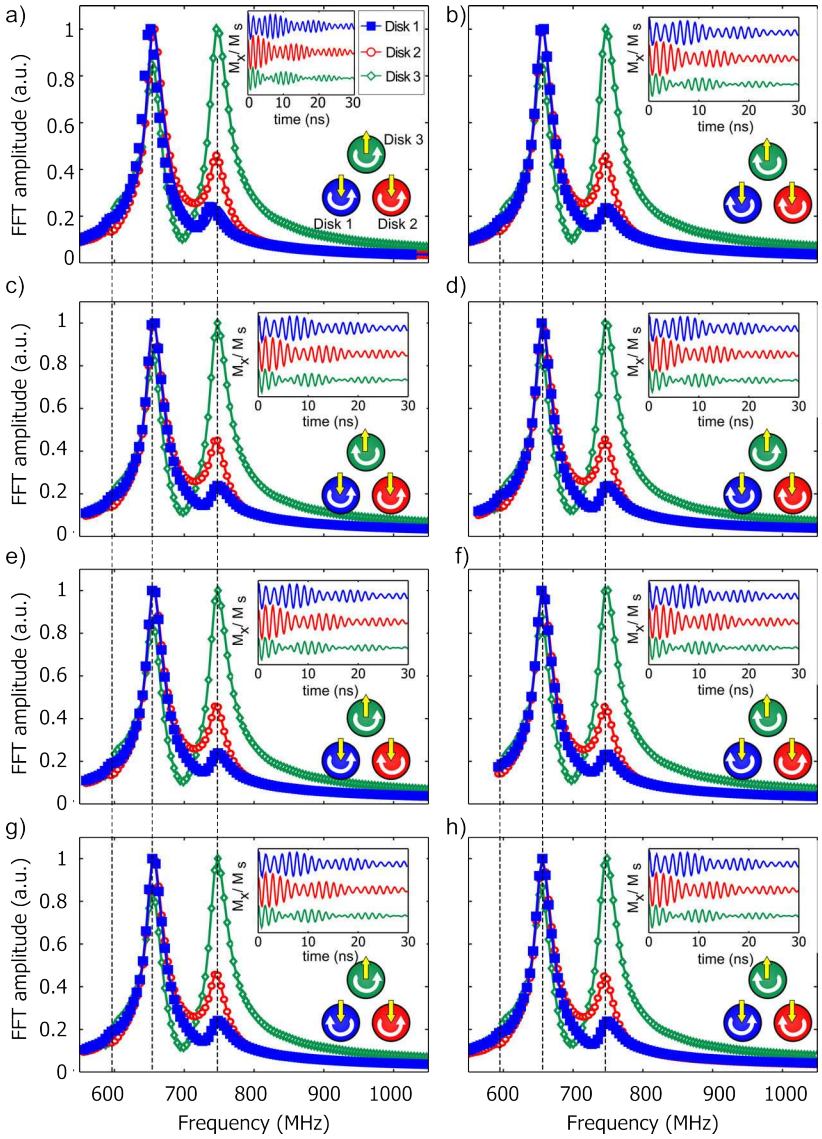

Figure 6.5. Micromagnetic simulations of three interacting disks with R/D =0.45 for a variety of χ (curved arrows) and fixed, identical p (straight arrows). Fourier transforms of the x-component of the volume-average magnetization M_x of each disk are shown. The insets show M_x as a function of time. In all cases, the maximum amplitude of the oscillations is $M_x/M_s \sim 0.1$. No significant difference was noticed due to different χ configuration.

Figure 6.7 shows the influence of the inter-disk separation on the resonant frequencies. When all vortices have the same p (Fig. 6.7a), the resonance splits into two different modes as the disks are brought closer together, whereas when one p is opposite to the others, three different frequencies are observed (Fig. 6.7b). In both cases, the magnitude of the splitting

increases with decreasing D. The coupling effects on the resonant frequencies are most apparent when the disks are almost touching (R/D =0.49) with a maximum shift of 22%. When the disks are further apart (R/D =0.20), the vortices in each disk oscillate at the single disk frequency f_o.

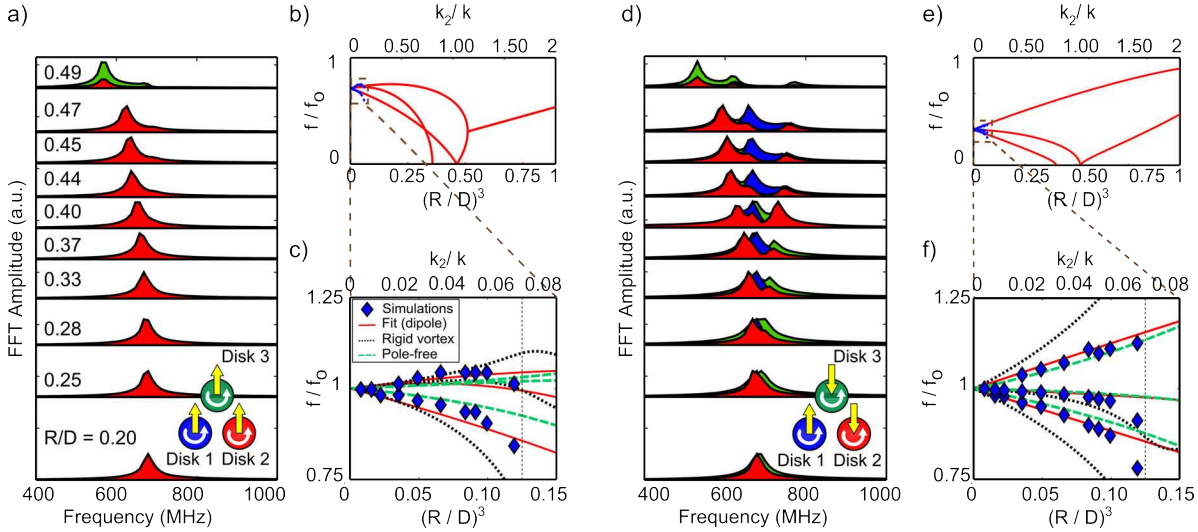

Figure 6.6. The Fourier spectra for each of the three disks are shown for a range of D for the cases when a) all vortices have the same core polarities (p=+1), and in d), there is one opposing polarity (p=-1). The baselines of the spectra are shifted by an amount proportional to D. The corresponding resonant frequencies from simulations (symbols) and theory (lines) are shown as a function of $(R/D)^3$ in (b) and (e), for p=+1 and p=-1 respectively. A zoomed-in image for both cases is included in c) and f) comparing the simulation results with different theoretical predictions. The solid green line represents the dipole-dipole interaction model where $C_{fit} = 2.82 \pm 0.06$ was used as the only fitting parameter. The disks are in contact for $R/D \geq 0.5$ (vertical dotted line).

6.4. Analytical Calculations

Theoretical models have been developed to describe the expected modes for vortices coupled via dipolar fields that are generated by the moving vortices for a variety of geometries. Calculations have been conducted for vortices in a 2D square array [100], for the normal modes for two disks that are excited together [109], and a more general treatment examines vortex pairs as well as 2D square and hexagonal arrays [20]. The main focus of the previous

work has been on the calculation of interaction integrals for specific models of the vortex spin distribution, e.g., the poles-free model [20]. In this section, a theory of the expected modes for the triangular arrangement considered in the simulations is derived using a simple dipole-dipole interaction model. The theoretical model used here was developed by Dr. Oleg Tchernyshyov and it has been published in reference [23]. My role was to run the micromagnetic simulations and compare the results with those predicted by such model.

For small displacements of a vortex $\mathbf{X}$ from its central equilibrium position, the restoring force and resonance frequency can be written as $\mathbf{F} = -k\mathbf{X}$ and $\omega_o = k/G$, respectively where G=$2\pi M_s t/\gamma$ is now defined as the gyrotropic constant that is independent of p and χ. Reference [110] gives an expression for ω_o in terms of the magnetic and geometrical parameters of the disk. In the limit of small aspect ratio $\beta = t/R \ll 1, \omega_o = \frac{5}{9\pi}\gamma\mu_o M_s\beta$, which corresponds to $k_{approx} = \frac{10\mu_o M_s^2 t^2}{9R}$. This estimate is reasonable for $\beta < 0.1$; however for the geometry used here $\beta = 0.16$, so calculating k using the full expressions in Ref. [110], $k = 0.81 \cdot k_{approx}$ was obtained. This corresponds to a frequency of 688.3 MHz, while the value obtained from micromagnetic simulations for a single disk was f_o= 680 MHz.

Magnetic vortices in adjacent disks will be coupled via magnetostatic interactions, however, the interactions are only significant when the space between the disks is considerably smaller than the disk diameter. A multipole expansion can be used to fully describe the magnetostatic interactions [20] and, in general, multiple terms are needed to obtain an accurate description. Nevertheless, as we will show below, the expressions obtained using just the dipole-dipole interactions are sufficient to describe the eigenfrequencies as a function of the inter-disk separation and the eigenvalues, which describe the vortex motion patterns associated with each mode. For more details on the calculations see the Appendix.

When an in-plane magnetic field is applied to a disk containing a vortex there is an associated Zeeman energy, $E_z = \mu_o \mathbf{H} \cdot \mathbf{d}$, where $\mathbf{d}$ is the induced magnetic moment of the disk. For small displacements, the dipole moment $\mathbf{d}$ of a shifted vortex can be approximated as

$$\mathbf{d} = -C\chi M_s t R \hat{\mathbf{z}} \times \mathbf{X} \tag{6.2}$$

where the dimensionless factor C is a function of t/R. The dipole-dipole interaction energy between the disks is

$$E_{int} = \frac{\mu_o}{4\pi D_{ij}^3} \left(\mathbf{d}_i \cdot \mathbf{d}_j - 3 \left(\mathbf{D}_{ij} \cdot \mathbf{d}_i \right) \left(\mathbf{D}_{ij} \cdot \mathbf{d}_i \right) \right) \tag{6.3}$$

where $\mathbf{D}_{ij}$ is the unit vector pointing from the center of disk i to the center of disk j, which can be written in terms of the vortex displacements as

$$E_{int} = k_2 \chi_i \chi_j \left(\mathbf{X}_i \cdot \mathbf{X}_j - 3 \left(\hat{\mathbf{z}} \cdot \mathbf{D}_{ij} \times \mathbf{X}_i \right) \left(\hat{\mathbf{z}} \cdot \mathbf{D}_{ij} \times \mathbf{X}_j \right) \right) \tag{6.4}$$

where $k_2 = C^2 \mu_o M_s^2 t^2 R^2 / 4\pi D^3$ for circular disks. For two disks arranged along the x-axis, this interaction energy reduces to $E_{int} = \chi_1 \chi_2 (k_2 x_1 x_2 - 2k_2 y_1 y_2)$. This can be written more generally in the form $E_{int} = \chi_1 \chi_2 (n_x x_1 x_2 + n_y y_1 y_2 + \mathcal{O}(|\vec{x_j}|^3))$, as in Ref. [20], where n_x and n_y are interaction coefficients that can be calculated for not just dipolar but also higher order magnetostatic interaction effects. For purely dipolar interactions, $n_x = k_2$ and $n_y = -2k_2$. Methods for calculating the coefficients n_x and n_y for two specific theoretical models of the vortex spin distribution, the rigid vortex model and the poles-free model, are given in Ref. [20] (see Eq. (13)) where the interaction energies are integrated over the full vortex magnetization distributions.

Regardless of the form of the interaction energy, the Lagrangian for an ensemble of disks is given by

$$L = \sum_i \left[(-p_i) G \dot{x}_i y_i - \frac{k}{2} |\mathbf{x}_i|^2 \right] - \sum_{i<j} E_{int}^{ij} \tag{6.5}$$

and together with the Lagrange equation for generalized coordinates q_i

$$\frac{d}{dt}\left(\frac{\partial L}{\partial \dot{q}_i}\right) - \frac{\partial L}{\partial q_i} = 0 \tag{6.6}$$

provide a description of the dynamic evolution of the system. We can completely remove the chiralities from the description by switching variables to $\mathbf{x}_i \to \chi_i \mathbf{x}_i$, which means that the shifts in frequencies are independent of χ_i. They will, however, depend on p. There are only two possible spectra based on the vortex polarities, one when all cores point in the same direction and another when one of the polarities is opposite to the others. Without loss of generality, we shall set $p_1 = p_2 = 1$, and leave $p_3 = p$ to distinguish the two possibilities. In order to take advantage of the symmetry, disks 1 and 2 are set along the x-axis, then the dipolar energy of the system can be written as

$$E_{int} = n_x x_1 x_2 + n_y y_1 y_2 + \frac{1}{4}(n_x + 3n_y)(x_1 + x_2)x_3 + \frac{1}{4}(3n_x + n_y)(y_1 + y_2)y_3 - \frac{\sqrt{3}}{4}(n_x - n_y)(x_2 - x_1)y_3 - \frac{\sqrt{3}}{4}(n_x - n_y)(y_2 - y_1)x_3. \tag{6.7}$$

Defining new coordinates $\overline{x} = (x_1 + x_2)/\sqrt{2}, \overline{y} = (y_1 + y_2)/\sqrt{2}, d = (x_1 - x_2)/\sqrt{(2)}$, and $\Delta = (y_1 - y_2)/\sqrt{(2)}$, then the the interaction energy can alternatively be written as

$$E_{int} = n_x x_1 x_2 + n_y y_1 y_2 + \frac{\sqrt{2}}{4}(n_x + 3n_y)\overline{x}x_3 + \frac{\sqrt{2}}{4}(3n_x + n_y)\overline{y}y_3 - \frac{\sqrt{6}}{4}d(x_2 - x_1)y_3 - \frac{\sqrt{6}}{4}(n_x - n_y)\Delta x_3. \quad (6.8)$$

Replacing this expression in the Lagrange equation 6.6 and rearranging conveniently, the equations of motion are given by

$$G\begin{pmatrix} \dot{\overline{y}} \\ \dot{y}_3 \\ \dot{d} \end{pmatrix} = \begin{pmatrix} (k + n_x) & \frac{\sqrt{2}}{4}(n_x + 3n_y) & 0 \\ p\frac{\sqrt{2}}{4}(n_x + 3n_y) & pk & \frac{\sqrt{6}}{4}(n_x - n_y) \\ 0 & -\frac{\sqrt{6}}{4}(n_x - n_y) & -(k - n_y) \end{pmatrix} \begin{pmatrix} \overline{x} \\ x_3 \\ \Delta \end{pmatrix}, \quad (6.9)$$

$$G\begin{pmatrix} \dot{\overline{x}} \\ \dot{x}_3 \\ \dot{\Delta} \end{pmatrix} = \begin{pmatrix} -(k + n_y) & -\frac{\sqrt{2}}{4}(3n_x + n_y) & 0 \\ -p\frac{\sqrt{2}}{4}(3n_x + n_y) & -pk & -p\frac{\sqrt{6}}{4}(n_x - n_y) \\ 0 & \frac{\sqrt{6}}{4}(n_x - n_y) & (k - n_x) \end{pmatrix} \begin{pmatrix} \overline{y} \\ y_3 \\ d \end{pmatrix}. \quad (6.10)$$

If only dipolar coupling is considered, then the equations of motion reduce to

$$G\begin{pmatrix} \dot{\overline{y}} \\ \dot{y}_3 \\ \dot{d} \end{pmatrix} = \begin{pmatrix} (k + k_2) & -\frac{5\sqrt{2}}{4}k_2 & 0 \\ -p\frac{5\sqrt{2}}{4}k_2 & pk & p\frac{3\sqrt{6}}{4}k_2 \\ 0 & -\frac{3\sqrt{6}}{4}k_2 & -(k + 2k_2) \end{pmatrix} \begin{pmatrix} \overline{x} \\ x_3 \\ \Delta \end{pmatrix}, \quad (6.11)$$

$$G\begin{pmatrix}\dot{\overline{x}}\\ \dot{x}_3\\ \dot{\Delta}\end{pmatrix}=\begin{pmatrix}-(k-2k_2) & -\frac{\sqrt{2}}{4}k_2 & 0\\ -p\frac{\sqrt{2}}{4}k_2 & -pk & -p\frac{3\sqrt{6}}{4}k_2\\ 0 & \frac{3\sqrt{6}}{4}k_2 & (k-k_2)\end{pmatrix}\begin{pmatrix}\overline{y}\\ y_3\\ d\end{pmatrix}. \tag{6.12}$$

If we now take the derivative of equation 6.12 and then replace 6.11 in the right side of the resulting equation, we can obtain a new equation of the form

$$\begin{pmatrix}\ddot{\overline{x}}\\ \ddot{x}_3\\ \ddot{\Delta}\end{pmatrix}=\begin{pmatrix}A_{11} & A_{12} & A_{13}\\ A_{21} & A_{22} & A_{23}\\ A_{31} & A_{32} & A_{33}\end{pmatrix}\begin{pmatrix}\overline{x}\\ x_3\\ \Delta\end{pmatrix}. \tag{6.13}$$

with the coefficients A_{ij} being defined in terms of k, k_2 and p by matrix multiplication of the square matrices appearing in equations 6.12 and 6.11 (in that order). The eigenfrequencies and eigenvalues can be obtained numerically from the equation above using standard procedures from linear algebra. These expressions are valid for any structure shape, not just circular disks, provided that the values for k_2 (or n_x and n_y), which can be derived for just a pair of disks, and k, which pertains to a single structure are obtained for the geometry of interest. These parameters do depend on the structure shape and dimensions and can be found either through the evaluation of appropriate interaction integrals or, in a simpler and faster way, from simulations of just one or two disks. Furthermore, the method used to derive 6.13 can be easily adapted to any geometrical arrangement of an arbitrary number of structures.

The dependence of the eigenfrequencies of 6.13 on k_2/k or $(R/D)^3$ is shown in Figs. 6.6c and 6.6f, where the relationship between k_2/k and R/D is given by $\frac{k_2}{k}=\frac{9C^2}{40\pi}\left(\frac{R}{D}\right)^3$ (valid for circular disks) and the parameter C depends on the radius and thickness of the disk. The

solutions are not always real for all k_2/k. For $k_2/k > 2/5$, at least one frequency is imaginary, suggesting that the vortices are destabilized. In Figs. 6.6c and 6.6f, the solid green line shows the dipole-dipole interaction results using a value $C_{fit} = 2.82 \pm 0.06$ that was extracted from simultaneous fits to the results shown in both plots (where the full expression in Ref. [110] was used to find k). Although this value is comparatively larger than C extracted from simulations ($C_{dip} = 2.0 \pm 0.1$) both are on the same order of magnitude. Using C_{fit} and C from the simulations yields $k_2/k \approx 0.070$ and $k_2/k \approx 0.036$ respectively for the maximum R/D =0.5 which corresponds to the case where disks are touching (vertical dotted line in figures 6.6c and 6.6c), which is below the instability threshold. This means that the splitting observed in the simulations is larger than what is predicted by the theory. Note that the resonance frequencies obtained for R/D =0.49 were not included in the fits since the gap between the disks is as little as a single cell and edge effects may artificially increase the coupling effects; for R/D =0.44, a difference of less than 2% was observed when the cell size used in the simulations was reduced from 4×4 nm^2 to 2×2 nm^2.

6.5. Results and Discussion

The frequency spectra obtained from the simulations agree well with the theory (Eq. 6.12), provided C is used as a fitting parameter (Figs. 6.6c and 6.6d). Equation 6.13 predicts three distinct modes for both p combinations; however, when all p are the same, the two higher-frequency modes are quite close, which is why only two modes are identified in the simulations. The frequency splitting is more pronounced for p = -1. The modes become distinguishable from one another at slightly lower R/D (larger D), and the magnitude of

the splitting is larger, which is consistent with reports of stronger coupling for opposing polarities in experiments [19] and simulations [111].

There are, however, discrepancies in the predicted magnitude of the splitting effects for all of the models considered. In Fig. 6.4, the parameter C was used as a fitting parameter to set the scale of the dipolar interaction model; however, its value can be estimated from the simulations of a single vortex in an isolated disk using Eq. 6.2 and fits to the core positions and magnetization values. When the core is displaced along the y-direction, the magnitude of the magnetic moment is $|M_x/M_s| = (C/\pi)(y/R)$, where $M_x = d_x/(\pi R^2 t)$ is the x-component of the dipole moment per unit volume. In simulations of a vortex in a single disk, for a displacement of $y = 8$ nm ($y/R = 0.064$) the corresponding magnetization shift was $|M_x/M_s| = 0.04$ for t = 20 nm and R = 126 nm. This yields $C_{dip} = 2.0 \pm 0.1$, which is smaller than the value obtained from fitting, which was $C_{fit} = 2.82 \pm 0.06$, hence the dipole model underestimates the magnitude of the observed splitting. Figs. 6.6c and 6.6d also show the frequency splitting that is predicted from Eq. 6.10 using n_x and n_y for the two-vortex and poles-free models from [20], which include higher order interaction effects. The poles-free model provides closer agreement but still underestimates the splitting, whereas the rigid vortex model overestimates the effect. The functional form of $f = f_o$ vs. $(R/D)^3$ is similar for all of the models, which occurs because the ratio n_x=n_y is close to the dipolar ratio of -1/2. The simple dipolar model therefore provides a useful functional form for the splitting; however, an intermediate model for the magnetization profile of a dynamic vortex is needed to correctly predict the magnitude of the effect. The discrepancies might be related to the physical restrictions imposed on each model, for example keeping the spins "frozen-in" without distorting the zero-field magnetization distribution in the rigid

vortex model allows for a simpler mathematical description since the circular symmetry is preserved but produces excessive magnetic surface charges on the sides ignoring the fact that the spins are able to adjust its orientation, especially near the boundary, to reduce the magnetostatic energy of the system. On the other extreme the poles-free model imposes a boundary condition that does not allow any magnetic surface charges to develop on the edges, creating an over-reduction of the magnetostatic energy of the system. Thus neither model provides realistic conditions for the spins near the boundary of the disk, which leads to larger discrepancies for disks that are in close proximity.

Fig. 6.7 illustrates the normal modes for the system from Eq. 6.10. Similar results are obtained for the poles-free and rigid vortex models, again because n_x/n_y -1/2. Figs. 6.7a, 6.7c, and 6.7e show the modes for p=+1. For the lowest frequency mode (Fig. 6.7a, the cores all have close to the same phase at any given time and attractive interactions occur whenever the dipoles are aligned along an axis that connects two disk centers. A spatially uniform field pulse applied to disks with the same χ provides a phase relationship between the cores that is similar to this mode, hence this is the dominant mode in Fig. 6.6a. When the core in the top disk is reversed (Fig. 6.7b), there are still attractive interactions for lowest frequency mode but the phases are timed such that when the north or south pole of the top disk is at its lowest point it is attracted equally to both of the lower disks.

In contrast, the higher frequency modes involve mainly repulsive interactions or combinations of repulsion and attraction. Repulsive interactions occur for the two higher frequency modes for p=+1 (Figs. 6.7c and 6.7e) but at different phases for each. For p=-1, the middle mode (Fig. 6.7d) involves motion of mainly the two bottom vortices and is characterized by both attractive and repulsive interactions, whereas the highest frequency mode (Fig. 6.7f)

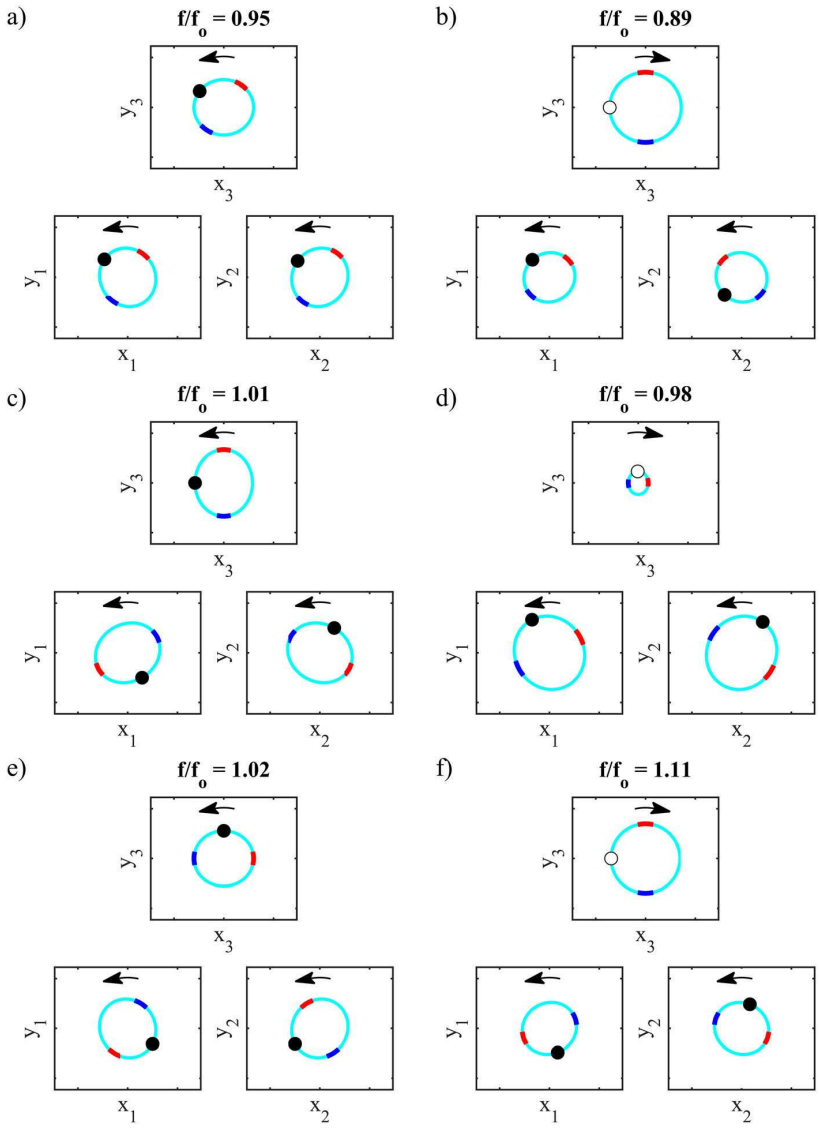

Figure 6.7. Illustration of the eigenmodes of Eq. 6.10 for R/D=0.45. The solid (cyan) ellipses show the core trajectories for each disk. The core at an instant of time is indicated by a black (white) circle for a positive (negative) p, and the arrows indicate the core's direction of travel. When the vortex core is displaced from equilibrium the dipole term dominates and the system can be treated as tiny magnets where the core shifted to the side means that are more spins in the vertical direction. For convenience parts of the ellipse are red and blue shaded to represent the north and south poles, respectively. These poles give an approximate idea of where maximum repulsion and attraction occur for a given mode. It is assumed $\chi = 1$ (counterclockwise) for all vortices.

mainly involves repulsive interactions that occur when like dipoles are aligned along an axis that connects two disk centers.

Spatial profiles of the normal modes (Fig. 6.8 shows modes for p=-1) were obtained from the simulations by calculating the Fourier transform of the z-component of the magnetization for each cell, as described in Ref. [112]. Plots of A cosϕ, where A and ϕ are the amplitude and phase, respectively, calculated from the simulations for R/D=0.45 provide a snapshot of the core positions in each disk. The opposite black and white contrast is due to an OOP distortion of the magnetization in the neighborhood of the core and resembles a secondary core with opposite polarity however, in reality, the mode will follow the path of the black or white areas not both. The phase has been shifted so that white (black) coincides with the positive (negative) pole of the dipole in the theoretical modes shown in Figs. 6.7b, 6.7d, and 6.7f to show that the relative phases observed in the simulations agree well with the eigenmodes of Eq. 6.10. Similar agreement is observed for the low frequency p=+1 mode (Fig. 6.7a), but the mode maps are not as clean for the two higher frequency p=1 modes because they are so close in frequency.

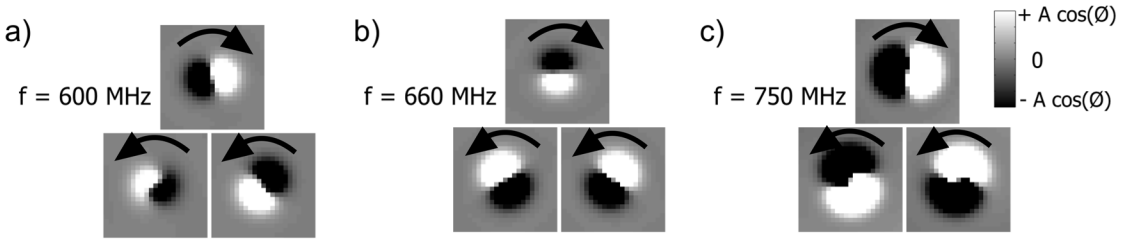

Figure 6.8. Mode maps obtained from simulations for R/D=0.45 with p =-1 where the top disk has a negative core polarity, which is the configuration shown in Figs. 6.7b, 6.7d, and 6.7f. Curly arrows indicate the circulation of the cores. Each plot represents an area of 93×93 nm^2. All of the vortices have $\chi = 1$ (counterclockwise).

6.6. Conclusions

In conclusion, micromagnetic simulations have been compared with analytical theory for a system of interacting vortices in three magnetic disks arranged in an equilateral triangle.

The theory and simulations agree on the main features of the observed dynamics. The vortex gyrotropic mode splits into three modes, the magnitude of the frequency splitting increases with decreasing inter-disk separation, and only two distinct frequency splitting behaviors are observed that depend on whether all p are the same or one polarity opposes the others, where the latter leads to stronger splitting. A simple model involving only dipolar interactions accurately captures the qualitative features of the coupled vortex dynamics including the frequencies and eigenmodes; however, a more detailed model of the dynamic vortex spin distribution will be required to improve predictions of the magnitude of the frequency splitting. Nevertheless, the simple dipole-dipole model, once calibrated for a particular disk geometry, provides an excellent description of the dynamics of interacting vortices that can be extended to more complex arrangements of magnetic vortices, including square or hexagonal arrays and chains of arbitrary geometries, which provide a simple framework for the development and optimization of new vortex-based devices. Experimental TR-PEEM measurements on a tri-disk system were also conducted as part of a collaboration with other researchers [24] where I was in charge of performing micromagnetic simulations. The experiments verify that the dipolar interactions between patterned structures are strong enough to cause a small splitting of the frequency spectrum that is consistent with the simulation and theory results discussed above.

CHAPTER 7

Conclusions

7.1. Results

Micromagnetic simulations were used to study spin textures in patterned structures. Three distinct but related topics were considered: 1) Formation of stable AV, 2) Dynamics of isolated magnetic AV, and 3) Dynamics of three interacting vortices. Experimental measurements were also conducted to study the AV formation process.

The influence of geometrical parameters and the field dependence on the formation of magnetic AV in pound-key structures was first considered. Simulations show that the asymmetries in the structure can be used to promote AV formation and regions with lower shape anisotropy lead the reversal process. In concordance with the simulations, that indicates that a significant mismatch in shape anisotropy favors AV formation, the experiments showed a formation rate of up to 80% for structures with thin external legs and wider central regions, and for magnetic fields that are aligned with the structure diagonal, whereas the formation rate is lower when there is less of a change in shape anisotropy. In addition, experimental measurements show that the optimal critical field for AV formation was slightly higher than the coercive field.

The microwave-frequency dynamics of AVs, stabilized in intersecting magnetic microstrips, was investigated using micromagnetic simulations. Gyrotropic and azimuthal modes were observed for in-plane excitations, and radial type modes for an out-of-plane excitation. These modes also couple to propagating SW in attached microstrips. The wavevectors of the leg modes are consistent with calculations of SW dispersion curves in extended wires, however, the modes are influenced by the symmetries and length scales of the intersection resonances,

and hence by the spin texture. This offer new possibilities for SW generation and manipulation on the nanoscale.

A system of interacting vortices in an equilateral-triangle arrangement was simulated and the results were compared to a simple analytical model that considers dipolar interactions only. Simulations showed that the eigenfrequency for the gyrotropic mode splits into three different modes. Although the details of the temporal behavior vary based on the initial configuration as well as the vortex core polarities, two splitting behaviors are observed: a strong splitting that occurs when all the polarities are the same as compared to a weaker splitting, when one polarity is opposite to the others. While the model underestimates the magnitude of the frequency splitting, the functional form captures the main features of the simulation better than more complex models when the coupling coefficient is used as a fit parameter so it can be used as a simple framework for modeling more complex vortex networks.

Micromagnetic simulations showed to be a very valuable tool to investigate the dynamics of non-uniform spin textures. The results obtained for the AV suggest new possibilities for generation and manipulation of SW although more research is required, e.g to find reliable ways to tune particular resonant modes for which the AV state promotes waves in the high-k end of the dispersion curve. In general, additional efforts directed to investigate the details of the dynamics response of AV textures, including in-depth comparison with experimental results, will not only contribute to the development of new technologies but also to a more fundamental understanding of these and similar textures found within the context of solid-state physics.

BIBLIOGRAPHY

[1] Y. Chen and A. Ppin, "Nanofabrication: Conventional and nonconventional methods," *Electrophoresis*, vol. 22, no. 2, pp. 187–207, 2001. 1

[2] J. Martín, J. Nogués, K. Liu, J. L. Vicent, and I. K. Schuller, "Ordered magnetic nanostructures: fabrication and properties," *Journal of Magnetism and Magnetic Materials*, vol. 256, no. 13, pp. 449 – 501, 2003.

[3] J. W. Lau and J. M. Shaw, "Magnetic nanostructures for advanced technologies: fabrication, metrology and challenges," *Journal of Physics D: Applied Physics*, vol. 44, no. 30, p. 303001, 2011.

[4] X. M. Cheng and D. J. Keavney, "Studies of nanomagnetism using synchrotron-based x-ray photoemission electron microscopy (X-PEEM)," *Reports on Progress in Physics*, vol. 75, no. 2, p. 026501, 2012.

[5] A. Biswas, I. S. Bayer, A. S. Biris, T. Wang, E. Dervishi, and F. Faupel, "Advances in top-down and bottom-up surface nanofabrication: Techniques, applications & future prospects," *Advances in Colloid and Interface Science*, vol. 170, no. 1-2, pp. 2–27, 2012.

[6] Y. Chen, "Nanofabrication by electron beam lithography and its applications: A review," *Microelectronic Engineering*, vol. 135, pp. 57–72, 2015.

[7] S. Okazaki, "High resolution optical lithography or high throughput electron beam lithography: The technical struggle from the micro to the nano-fabrication evolution," 1

[8] K. L. Metlov and K. Y. Guslienko, "Stability of magnetic vortex in soft magnetic nanosized circular cylinder," *Journal of Magnetism and Magnetic Materials*, vol. 242245,

Part 2, pp. 1015 – 1017, 2002. Proceedings of the Joint European Magnetic Symposia (JEMS'01). 2, 94, 96

[9] H. Jung, Y.-S. Yu, K.-S. Lee, M.-Y. Im, P. Fischer, L. Bocklage, A. Vogel, M. Bolte, G. Meier, and S.-K. Kim, "Observation of coupled vortex gyrations by 70-ps-time- and 20-nm-space-resolved full-field magnetic transmission soft x-ray microscopy," *Applied Physics Letters*, vol. 97, no. 22, p. 222502, 2010. 4

[10] H. Wang and C. E. Campbell, "Spin dynamics of a magnetic antivortex: Micromagnetic simulations," *Physical Review B*, vol. 76, p. 220407, 2007. 4, 69, 70

[11] A. Drews, B. Krüger, M. Bolte, and G. Meier, "Current- and field-driven magnetic antivortices," *Physical Review B*, vol. 77, p. 094413, 2008. 68, 69

[12] S. Gliga, M. Yan, R. Hertel, and C. M. Schneider, "Ultrafast dynamics of a magnetic antivortex: Micromagnetic simulations," *Physical Review B*, vol. 77, p. 060404, 2008. 69

[13] X.-J. Xing and S.-W. Li, "Spin-transfer torque driven magnetic antivortex dynamics by sudden excitation of a spin-polarized dc," *Journal of Applied Physics*, vol. 105, no. 9, p. 093902, 2009. 69

[14] T. Kamionka, M. Martens, K. W. Chou, M. Curcic, A. Drews, G. Schütz, T. Tyliszczak, H. Stoll, B. Van Waeyenberge, and G. Meier, "Magnetic antivortex-core reversal by circular-rotational spin currents," *Physical Review Letters*, vol. 105, p. 137204, 2010. 47, 69

[15] T. Kamionka, M. Martens, K. W. Chou, A. Drews, T. Tyliszczak, H. Stoll, B. Van Waeyenberge, and G. Meier, "Magnetic antivortex-core reversal by rotating magnetic fields," *Physical Review B*, vol. 83, p. 224422, 2011.

[16] M. Martens, T. Kamionka, A. Drews, B. Krger, and G. Meier, "Influence of the winding number on field- and current driven dynamics of magnetic vortices and antivortices," *Journal of Applied Physics*, vol. 112, no. 1, p. 013917, 2012.

[17] M. Pues, M. Martens, and G. Meier, "Absorption spectroscopy of isolated magnetic antivortices," *Journal of Applied Physics*, vol. 116, no. 15, p. 153903, 2014.

[18] G. A. Riley, H. J. J. Liu, M. A. Asmat-Uceda, A. Haldar, and K. S. Buchanan, "Observation of the dynamic modes of a magnetic antivortex using brillouin light scattering," *Physical Review B*, vol. 92, p. 064423, 2015. 4, 6, 69, 73, 86, 87

[19] D.-S. Han, A. Vogel, H. Jung, K.-S. Lee, M. Weigand, H. Stoll, G. Schütz, P. Fischer, G. Meier, and S.-K. Kim, "Wave modes of collective vortex gyration in dipolar-coupled-dot-array magnonic crystals," *Scientific reports*, vol. 3, p. 2262. 4, 95, 111

[20] O. V. Sukhostavets, J. González, and K. Y. Guslienko, "Multipole magnetostatic interactions and collective vortex excitations in dot pairs, chains, and two-dimensional arrays," *Physical Review B*, vol. 87, p. 094402, 2013. 104, 105, 106, 111

[21] J. Shibata and Y. Otani, "Magnetic vortex dynamics in a two-dimensional square lattice of ferromagnetic nanodisks," *Physical Review B*, vol. 70, no. 1, p. 012404, 2004. 4, 95

[22] M. Asmat-Uceda, L. Li, A. Haldar, B. Shaw, and K. S. Buchanan, "Geometry and field dependence of the formation of magnetic antivortices in pound-key-like structures," *Journal of Applied Physics*, vol. 117, no. 17, p. 173902, 2015. 6, 46, 69

[23] M. Asmat-Uceda, X. Cheng, X. Wang, D. J. Clarke, O. Tchernyshyov, and K. S. Buchanan, "A comparison of numerical simulations and analytical theory of the dynamics of interacting magnetic vortices," *Journal of Applied Physics*, vol. 117, no. 12, p. 123916, 2015. 6, 96, 105

[24] X. Wang, D. Keavney, M. Asmat-Uceda, K. Buchanan, A. Melikyan, and X. Cheng, "Time-resolved photoemission electron microscopy imaging of mode coupling between three interacting magnetic vortices," *Applied Physics Letters*, vol. 105, no. 10, p. 102408, 2014. 6, 96, 115

[25] L. D. Landau and E. Lifshitz, "On the theory of the dispersion of magnetic permeability in ferromagnetic bodies," *Physikalische Zeitschrift der Sowjetunion*, vol. 8, no. 153, pp. 101–114, 1935. 7

[26] W. F. Brown, *Micromagnetics*. Interscience Publisher, 1963. 7, 10, 18

[27] T. L. Gilbert, "A phenomenological theory of damping in ferromagnetic materials," *IEEE Transactions on Magnetics*, vol. 40, no. 6, pp. 3443–3449, 2004. 7

[28] T. Gilbert, "A lagrangian formulation of the gyromagnetic equation of the magnetization field," *Physical Review*, vol. 100, p. 1243, 1955. 7

[29] T. Olson, B. Lengsfield, G. J. Parker, M. Shiimoto, M. Sugiyama, and L. Xu, "Optimizing Modeled ECC Media Structures for MAMR," *IEEE Transactions on Magnetics*, vol. 52, no. 2, pp. 1–8, 2016. 8

[30] C. Park, J. J. Kan, C. Ching, J. Ahn, L. Xue, R. Wang, A. Kontos, S. Liang, M. Bangar, H. Chen, S. Hassan, M. Gottwald, X. Zhu, M. Pakala, and S. H. Kang, "Systematic

optimization of 1 Gbit perpendicular magnetic tunnel junction arrays for 28 nm embedded STT-MRAM and beyond," in *2015 IEEE International Electron Devices Meeting (IEDM)*, pp. 26.2.1–26.2.4, 2015.

[31] M.-A. Bolte, G. D. Meier, and I. D. P. Möller, "Understanding and predicting the electronic and dynamic behavior of nanoscale magnetic random access memory (MRAM) cells using micromagnetic modelling and simulation," in *Proceedings of the 19th European Conference on Modelling and Simulation 2005 (ECMS 2005)*, pp. 574–579, 2005. 8

[32] R. A. Van Mourik, T. Phung, S. S. P. Parkin, and B. Koopmans, "In-line spin-torque nano-oscillators in perpendicularly magnetized nanowires," *Physical Review B*, vol. 93, p. 014435, 2016. 8

[33] V. Pribiag, I. Krivorotov, G. Fuchs, P. Braganca, O. Ozatay, J. Sankey, D. Ralph, and R. Buhrman, "Magnetic vortex oscillator driven by dc spin-polarized current," *Nature Physics*, vol. 3, no. 7, pp. 498–503, 2007. 8, 95

[34] K.-S. Lee and S.-K. Kim, "Conceptual design of spin wave logic gates based on a machzehnder-type spin wave interferometer for universal logic functions," *Journal of Applied Physics*, vol. 104, no. 5, p. 053909, 2008. 8

[35] A. Khitun, D. E. Nikonov, M. Bao, K. Galatsis, and K. L. Wang, "Feasibility study of logic circuits with a spin wave bus," *Nanotechnology*, vol. 18, no. 46, p. 465202, 2007.

[36] M. P. Kostylev, A. A. Serga, T. Schneider, B. Leven, and B. Hillebrands, "Spin-wave logical gates," *Applied Physics Letters*, vol. 87, no. 15, p. 153501, 2005.

[37] R. Hertel, W. Wulfhekel, and J. Kirschner, "Domain-wall induced phase shifts in spin waves," *Physical Review Letters*, vol. 93, p. 257202, 2004.

[38] D. A. Allwood, G. Xiong, M. D. Cooke, C. C. Faulkner, D. Atkinson, N. Vernier, and R. P. Cowburn, "Submicrometer ferromagnetic NOT gate and shift register," *Science*, vol. 296, no. 5575, pp. 2003–2006, 2002. 8

[39] J. E. Miltat and M. J. Donahue, "Numerical micromagnetics: Finite difference methods," in *Handbook of Magnetism and Advanced Magnetic Materials*, Wiley Online Library, 2007. 8

[40] M. Bode, M. Heide, K. Von Bergmann, P. Ferriani, S. Heinze, G. Bihlmayer, A. Kubetzka, O. Pietzsch, S. Blügel, and R. Wiesendanger, "Chiral magnetic order at surfaces driven by inversion asymmetry," *Nature*, vol. 447, no. 7141, pp. 190–193, 2007. 10

[41] Z. Li and S. Zhang, "Domain-wall dynamics driven by adiabatic spin-transfer torques," *Physical Review B*, vol. 70, p. 024417, 2004. 10

[42] J. C. Maxwell, *A treatise on electricity and magnetism*, vol. 2. Clarendon press, 1873. 12

[43] J. A. Osborn, "Demagnetizing factors of the general ellipsoid," *Physical Review*, vol. 67, pp. 351–357, 1945.

[44] E. C. Stoner, "The demagnetizing factors for ellipsoids," *The London, Edinburgh, and Dublin Philosophical Magazine and Journal of Science*, vol. 36, no. 263, pp. 803–821, 1945.

[45] M. Beleggia, M. D. Graef, and Y. Millev, "Demagnetization factors of the general ellipsoid: An alternative to the maxwell approach," *Philosophical Magazine*, vol. 86, no. 16, pp. 2451–2466, 2006. 12, 63

[46] R. I. Joseph and E. Schlmann, "Demagnetizing field in nonellipsoidal bodies," *Journal of Applied Physics*, vol. 36, no. 5, pp. 1579–1593, 1965. 12

[47] Y. D. Yan and E. D. Torre, "On the computation of particle demagnetizing fields," *IEEE Transactions on Magnetics*, vol. 25, no. 4, pp. 2919–2921, 1989.

[48] A. J. Newell, W. Williams, and D. J. Dunlop, "A generalization of the demagnetizing tensor for nonuniform magnetization," *Journal of Geophysical Research: Solid Earth*, vol. 98, no. B6, pp. 9551–9555, 1993. 25

[49] A. Aharoni, "Demagnetizing factors for rectangular ferromagnetic prisms," *Journal of Applied Physics*, vol. 83, no. 6, pp. 3432–3434, 1998.

[50] D. Chernyshenko and H. Fangohr, "Computing the demagnetizing tensor for finite difference micromagnetic simulations via numerical integration," *Journal of Magnetism and Magnetic Materials*, vol. 381, pp. 440–445, 2015. 12

[51] C. Kittel, "Physical theory of ferromagnetic domains," *Reviews of modern Physics*, vol. 21, no. 4, p. 541, 1949. 13

[52] J. Stöhr and H. Siegmann, *Magnetism: From Fundamentals to Nanoscale Dynamics*. Series in Solid-State Sciences. Springer, 2006. 17

[53] A. Hubert and R. Schäfer, *Magnetic domains: the analysis of magnetic microstructures*. Springer Science & Business Media, 2008. 18

[54] G. Bertotti, *Hysteresis in magnetism: for physicists, materials scientists, and engineers*. Academic press, 1998. 19

[55] K. Y. Guslienko and A. N. Slavin, "Boundary conditions for magnetization in magnetic nanoelements," *Phys. Rev. B*, vol. 72, p. 014463, 2005. 20

[56] C. J. García-Cervera, "Numerical micromagnetics: a review," 2007. 23

[57] J. D. Jackson and R. F. Fox, "Classical electrodynamics," *American Journal of Physics*, vol. 67, no. 9, pp. 841–842, 1999. 24

[58] C. Abert, F. Bruckner, C. Vogler, R. Windl, R. Thanhoffer, and D. Suess, "A full-fledged micromagnetic code in fewer than 70 lines of NumPy," *Journal of Magnetism and Magnetic Materials*, vol. 387, pp. 13–18, 2015. 25, 26

[59] D. Wei, *Micromagnetics and Recording Materials*, ch. 2. Springer Science & Business Media, 2012. 26

[60] M. Donahue and D. Porter, "Interagency report nistir 6376," *National Institute of Standards and Technology, Gaithersburg, MD*, 1999. 29, 53

[61] A. Vansteenkiste, J. Leliaert, M. Dvornik, M. Helsen, F. Garcia-Sanchez, and B. Van Waeyenberge, "The design and verification of mumax3," *AIP Advances*, vol. 4, no. 10, p. 107133, 2014. 30, 53

[62] W. Rave and A. Hubert, "Magnetic ground state of a thin-film element," *IEEE Transactions on Magnetics*, vol. 36, no. 6, pp. 3886–3899, 2000. 33

[63] M. Grimsditch, G. K. Leaf, H. G. Kaper, D. A. Karpeev, and R. E. Camley, "Normal modes of spin excitations in magnetic nanoparticles," *Physical Review B*, vol. 69, p. 174428, 2004. 35

[64] R. D. McMichael and M. D. Stiles, "Magnetic normal modes of nanoelements," *Journal of Applied Physics*, vol. 97, no. 10, p. 10J901, 2005. 35

[65] K. H. Bennemann, *Non-linear optics in metals*. Oxford University Press, 1998. 42

[66] K. Y. Guslienko, V. Novosad, Y. Otani, H. Shima, and K. Fukamichi, "Field evolution of magnetic vortex state in ferromagnetic disks," *Applied Physics Letters*, vol. 78, no. 24, p. 3848, 2001. 46

[67] R. Cowburn, D. Koltsov, A. Adeyeye, M. Welland, and D. Tricker, "Single-domain circular nanomagnets," *Physical Review Letters*, vol. 83, no. 5, p. 1042, 1999. 46, 94

[68] P. Vavassori, N. Zaluzec, V. Metlushko, V. Novosad, B. Ilic, and M. Grimsditch, "Magnetization reversal via single and double vortex states in submicron permalloy ellipses," *Physical Review B*, vol. 69, no. 21, pp. 3–8, 2004. 46

[69] A. Vogel, A. Corinna Niemann, C. Stenner, A. Drews, M.-Y. Im, P. Fischer, and G. Meier, "Vortex dynamics in triangular-shaped confining potentials," *Journal of Applied Physics*, vol. 112, no. 6, p. 063916, 2012. 46

[70] A. Vogel, T. Kamionka, M. Martens, A. Drews, K. W. Chou, T. Tyliszczak, H. Stoll, B. Van Waeyenberge, and G. Meier, "Coupled vortex oscillations in spatially separated permalloy squares," *Physical review letters*, vol. 106, no. 13, p. 137201, 2011. 46

[71] A. Haldar and K. S. Buchanan, "Magnetic antivortex formation in pound-key-like nanostructures," *Applied Physics Letters*, vol. 102, p. 112401, 2013. 46, 48, 49, 58, 69

[72] P. E. Roy, J. H. Lee, T. Trypiniotis, D. Anderson, G. A. C. Jones, D. Tse, and C. H. W. Barnes, "Antivortex domain walls observed in permalloy rings via magnetic force microscopy," *Physical Review B*, vol. 79, p. 060407, 2009. 47

[73] K. Shigeto, T. Okuno, K. Mibu, T. Shinjo, and T. Ono, "Magnetic force microscopy observation of antivortex core with perpendicular magnetization in patterned thin film of permalloy," *Applied Physics Letters*, vol. 80, no. 22, pp. 4190–4192, 2002. 47

[74] M. Pues, M. Martens, T. Kamionka, and G. Meier, "Reliable nucleation of isolated magnetic antivortices," *Applied Physics Letters*, vol. 100, no. 16, p. 162404, 2012. 47, 48

[75] V. L. Mironov, O. L. Ermolaeva, S. A. Gusev, A. Y. Klimov, V. V. Rogov, B. A. Gribkov, O. G. Udalov, A. A. Fraerman, R. Marsh, C. Checkley, R. Shaikhaidarov,

and V. T. Petrashov, "Antivortex state in crosslike nanomagnets," *Physical Review B*, vol. 81, p. 094436, 2010. 47, 48

[76] B. Cullity and C. Graham, *Introduction to Magnetic Materials*. John Wiley & Sons, 2009. 64

[77] B. E. Argyle, E. Terrenzio, and J. C. Slonczewski, "Magnetic vortex dynamics using the optical Cotton-Mouton effect," *Physical Review Letters*, vol. 53, pp. 190–193, 1984. 68

[78] K. Y. Guslienko, B. A. Ivanov, V. Novosad, Y. Otani, H. Shima, and K. Fukamichi, "Eigenfrequencies of vortex state excitations in magnetic submicron-size disks," *Journal of Applied Physics*, vol. 91, no. 10, pp. 8037–8039, 2002. 68, 96, 97, 98

[79] J. P. Park, P. Eames, D. M. Engebretson, J. Berezovsky, and P. A. Crowell, "Imaging of spin dynamics in closure domain and vortex structures," *Physical Review B*, vol. 67, p. 020403, 2003.

[80] M. Buess, R. Höllinger, T. Haug, K. Perzlmaier, U. Krey, D. Pescia, M. R. Scheinfein, D. Weiss, and C. H. Back, "Fourier transform imaging of spin vortex eigenmodes," *Physical Review Letters*, vol. 93, p. 077207, 2004. 68, 81

[81] M. Buess, T. Haug, M. R. Scheinfein, and C. H. Back, "Micromagnetic dissipation, dispersion, and mode conversion in thin permalloy platelets," *Physical Review Letters*, vol. 94, p. 127205, 2005.

[82] J. P. Park and P. A. Crowell, "Interactions of spin waves with a magnetic vortex," *Physical Review Letters*, vol. 95, p. 167201, 2005. 68, 73

[83] X. J. Xing, Y. P. Yu, S. X. Wu, L. M. Xu, and S. W. Li, "Bloch-point-mediated magnetic antivortex core reversal triggered by sudden excitation of a suprathreshold spin-polarized current," *Applied Physics Letters*, vol. 93, no. 20, p. 202507, 2008. 69

[84] A. Drews, B. Kruger, G. Meier, S. Bohlens, L. Bocklage, T. Matsuyama, and M. Bolte, "Current- and field-driven magnetic antivortices for nonvolatile data storage," *Applied Physics Letters*, vol. 94, no. 6, p. 062504, 2009.

[85] A. Kunz, E. C. Breitbach, and A. J. Smith, "Antivortex dynamics in magnetic nanostripes," *Journal of Applied Physics*, vol. 105, no. 7, p. 07D502, 2009. 69

[86] M. Curcic, B. Van Waeyenberge, A. Vansteenkiste, M. Weigand, V. Sackmann, H. Stoll, M. Fähnle, T. Tyliszczak, G. Woltersdorf, C. H. Back, and G. Schütz, "Polarization selective magnetic vortex dynamics and core reversal in rotating magnetic fields," *Physical Review Letters*, vol. 101, p. 197204, 2008. 69

[87] M. P. Kostylev, G. Gubbiotti, J.-G. Hu, G. Carlotti, T. Ono, and R. L. Stamps, "Dipole-exchange propagating spin-wave modes in metallic ferromagnetic stripes," *Physical Review B*, vol. 76, p. 054422, 2007. 74, 87, 88

[88] K. Y. Guslienko and A. N. Slavin, "Magnetostatic Green's functions for the description of spin waves in finite rectangular magnetic dots and stripes," *Journal of Magnetism and Magnetic Materials*, vol. 323, no. 1819, pp. 2418 – 2424, 2011. 87, 88

[89] K. Y. Guslienko, K.-S. Lee, and S.-K. Kim, "Dynamic origin of vortex core switching in soft magnetic nanodots," *Physical Review Letters*, vol. 100, p. 027203, Jan 2008. 89

[90] T. Shinjo, T. Okuno, R. Hassdorf, K. Shigeto, and T. Ono, "Magnetic vortex core observation in circular dots of permalloy," *Science*, vol. 289, no. 5481, pp. 930–932, 2000. 94

[91] H. Jung, K.-S. Lee, D.-E. Jeong, Y.-S. Choi, Y.-S. Yu, D.-S. Han, A. Vogel, L. Bocklage, G. Meier, M.-Y. Im, *et al.*, "Tunable negligible-loss energy transfer between dipolar-coupled magnetic disks by stimulated vortex gyration," *Scientific reports*, vol. 1, no. 59. 95

[92] S. Sugimoto, Y. Fukuma, S. Kasai, T. Kimura, A. Barman, and Y. Otani, "Dynamics of coupled vortices in a pair of ferromagnetic disks," *Physical review letters*, vol. 106, no. 19, p. 197203, 2011. 95

[93] A. Vogel, M. Martens, M. Weigand, and G. Meier, "Signal transfer in a chain of stray-field coupled ferromagnetic squares," *Applied Physics Letters*, vol. 99, no. 4, p. 042506, 2011. 95

[94] K. Arai, T. Okuda, K. Fukumoto, M. Kotsugi, T. Ohkouchi, K. Kodama, T. Kimura, Y. Haruyama, T. Nakamura, T. Matsushita, H. Osawa, T. Muro, S. Matsui, A. Kakizaki, Y. Otani, and T. Kinoshita, "Dynamics of magnetostatically coupled vortices observed by time-resolved photoemission electron microscopy," *Japanese Journal of Applied Physics*, vol. 50, no. 5R, p. 053001, 2011. 95

[95] K.-S. Lee, H. Jung, D.-S. Han, and S.-K. Kim, "Normal modes of coupled vortex gyration in two spatially separated magnetic nanodisks," *Journal of Applied Physics*, vol. 110, no. 11, p. 113903, 2011. 95

[96] A. Awad, G. Aranda, D. Dieleman, K. Guslienko, G. Kakazei, B. Ivanov, and F. Aliev, "Spin excitation frequencies in magnetostatically coupled arrays of vortex state circular permalloy dots," *Applied Physics Letters*, vol. 97, no. 13, p. 132501, 2010. 95

[97] A. Barman, S. Barman, T. Kimura, Y. Fukuma, and Y. Otani, "Gyration mode splitting in magnetostatically coupled magnetic vortices in an array," *Journal of Physics D: Applied Physics*, vol. 43, no. 42, p. 422001, 2010.

[98] A. Vogel, A. Drews, T. Kamionka, M. Bolte, and G. Meier, "Influence of dipolar interaction on vortex dynamics in arrays of ferromagnetic disks," *Physical review letters*, vol. 105, no. 3, p. 037201, 2010.

[99] A. Y. Galkin, B. Ivanov, and C. Zaspel, "Collective modes for an array of magnetic dots in the vortex state," *Physical Review B*, vol. 74, no. 14, p. 144419, 2006. 95

[100] J. Shibata, K. Shigeto, and Y. Otani, "Dynamics of magnetostatically coupled vortices in magnetic nanodisks," *Physical Review B*, vol. 67, no. 22, p. 224404, 2003. 95, 104

[101] N. Locatelli, V. Naletov, J. Grollier, G. De Loubens, V. Cros, C. Deranlot, C. Ulysse, G. Faini, O. Klein, and A. Fert, "Dynamics of two coupled vortices in a spin valve nanopillar excited by spin transfer torque," *Applied Physics Letters*, vol. 98, no. 6, p. 062501, 2011. 95

[102] S. Jain, V. Novosad, F. Y. Fradin, J. E. Pearson, V. Tiberkevich, A. N. Slavin, and S. D. Bader, "From chaos to selective ordering of vortex cores in interacting mesomagnets," *Nature communications*, vol. 3, p. 1330, 2012. 95

[103] K. Y. Guslienko, V. Novosad, Y. Otani, H. Shima, and K. Fukamichi, "Magnetization reversal due to vortex nucleation, displacement, and annihilation in submicron ferromagnetic dot arrays," *Physical Review B*, vol. 65, p. 024414, 2001. 96

[104] N. Usov and S. Peschany, "Magnetization curling in a fine cylindrical particle," *Journal of Magnetism and Magnetic Materials*, vol. 118, no. 3, pp. L290 – L294, 1993. 96

[105] A. Thiele, "Steady-state motion of magnetic domains," *Physical Review Letters*, vol. 30, no. 6, p. 230, 1973. 97

[106] D. L. Huber, "Dynamics of spin vortices in two-dimensional planar magnets," *Physical Review B*, vol. 26, pp. 3758–3765, 1982. 97

[107] K. Y. Guslienko, "Low-frequency vortex dynamic susceptibility and relaxation in mesoscopic ferromagnetic dots," *Applied Physics Letters*, vol. 89, no. 2, p. 022510, 2006. 98

[108] J.-Y. Kim and S.-B. Choe, "Simple harmonic oscillation of ferromagnetic vortex core," *journal of Magnetics*, vol. 12, no. 3, pp. 113–117, 2007. 98

[109] O. V. Sukhostavets, J. M. Gonzalez, and K. Y. Guslienko, "Magnetic vortex excitation frequencies and eigenmodes in a pair of coupled circular dots," *Applied physics express*, vol. 4, no. 6, p. 065003, 2011. 104

[110] K. Y. Guslienko, X. Han, D. Keavney, R. Divan, and S. Bader, "Magnetic vortex core dynamics in cylindrical ferromagnetic dots," *Physical review letters*, vol. 96, no. 6, p. 067205, 2006. 105, 110

[111] J.-H. Kim, K.-S. Lee, H. Jung, D.-S. Han, and S.-K. Kim, "Information-signal-transfer rate and energy loss in coupled vortex-state networks," *Applied Physics Letters*, vol. 101, no. 9, p. 092403, 2012. 111

[112] M. Yan, G. Leaf, H. Kaper, R. Camley, and M. Grimsditch, "Spin-wave modes in a cobalt square vortex: Micromagnetic simulations," *Physical Review B*, vol. 73, no. 1, p. 014425, 2006. 114

APPENDIX A

AV CRITICAL FIELD SIMULATIONS USING MUMAX (2D) AND OOMMF (3D)

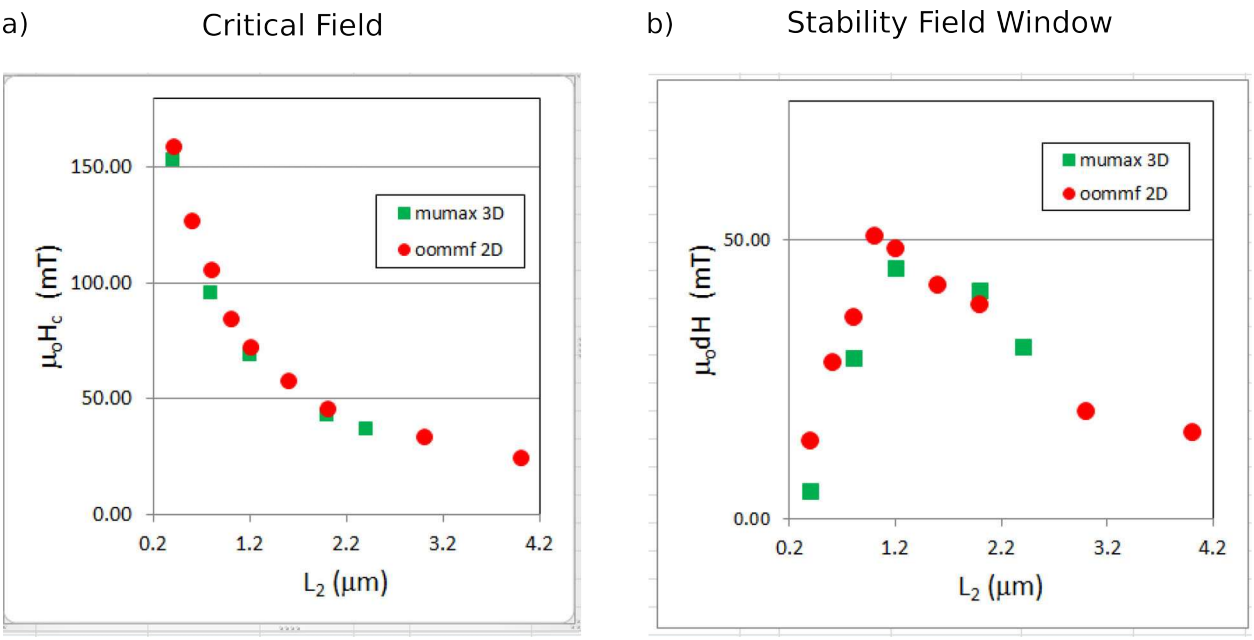

Figure A.1. Simulation results for the coercivity $\mu_o H_c$ and field window of AV stability $\mu_o \Delta H$ obtained using 2D and 2D simulations with OOMMF and MuMax[3] respectively, shown as a function of the sample width, L_2, for scaled versions of structure AV-S3 ($L_2 = 1.0, 1.6$ and 4.0 μm). The sample thickness was 40 nm and cell sizes of $4\times4\times40$ nm^3 and $4\times4\times4$ nm^3 were used for the 2D and 3D simulations, respectively.

APPENDIX B

MOKE SETUP

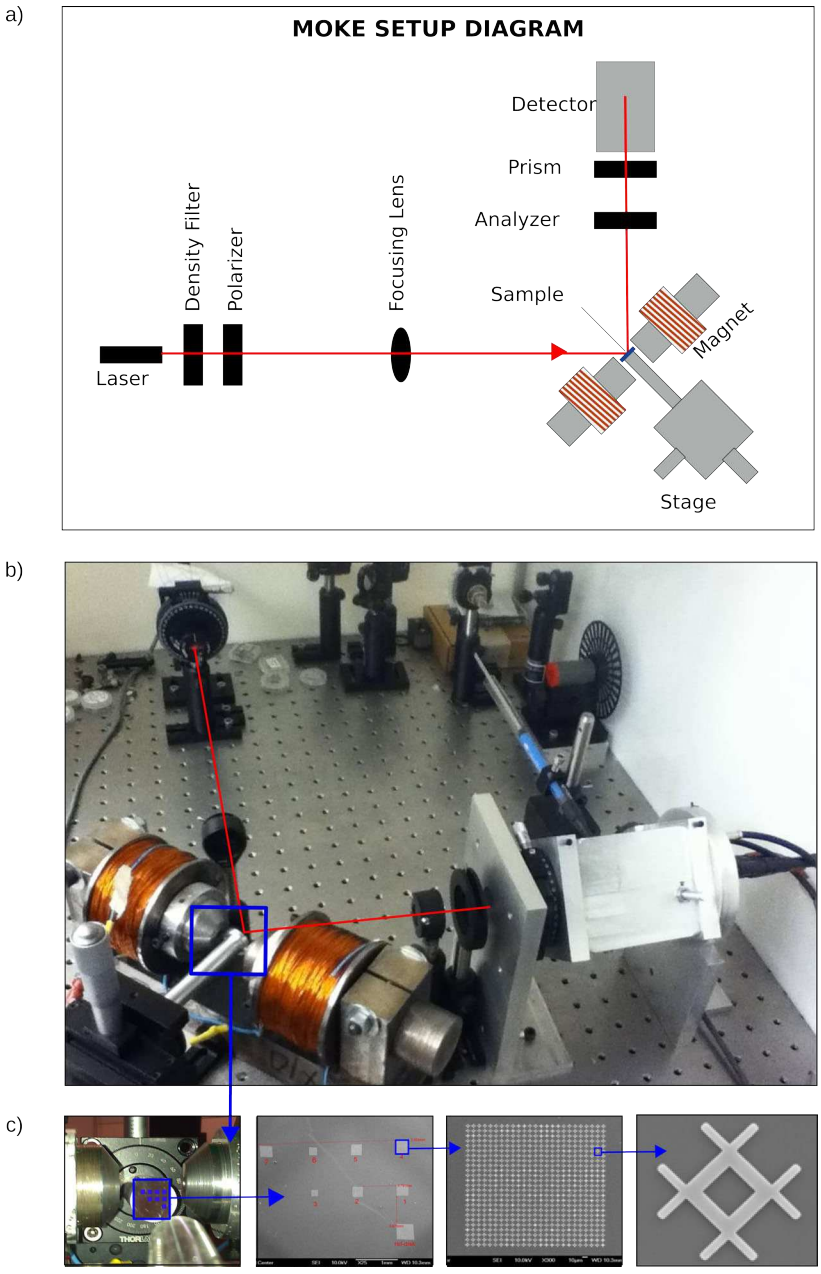

Figure B.1. Schematic diagram and a picture of the MOKE equipment used in this study are shown in a) and b) respectively. The system was covered with a plastic enclosure to minimize air currents. Details of the layout of the different arrays and one of the pound-key structures (AV-S3) used in this study are shown at different magnifications in c).

APPENDIX C

Example scripts to run simulations using MuMax and OOMMF

```
/* MuMax3
#########################################################
# Description: hysteresis loop for 400 nm AV pound-key like structure
# Cubic cells of 4nm cellsize (3D simulations). This is intended to address the fact that
# thickness of ~40nm is comparable with lateral dimensions of the legs for this structure
Created on 3/27/2015 by Martin Asmat-Uceda. Colorado State University
Last updated 08/10/2016 by Martin Asmat-Uceda
#########################################################
*/
////////////////////////////////////////////////////
////// FILES AND CONSTANTS //////
////////////////////////////////////////////////////
direc:=  "/media/kristen/titanic/titan/hysteresis/"
outfile:= "hyster_AV2C_2L_0400nm"
mask:=  sprint(direc,"mask_AVC.png")
ang:=  pi/4 //Angle in radians at which the magnetic field is applied, w.r.t the horizontal

////////////////////////////////////////////////////
///// MATERIAL PARAMETERS /////
////////////////////////////////////////////////////
// for Permalloy //
Msat  = 8.6E5  //saturation magnetization for Py (in A/m)
Aex   = 1.3E-11  //exchange constant (in J/m)
alpha = 1  //damping constant (unitless) for static case

////////////////////////////////////////////////////
////// GEOMETRY AND MESH //////
////////////////////////////////////////////////////
//sample dimensions in m//
length:= 400E-9
width:=  400E-9
thickness:=   40E-9
//mesh and cell dimensions//
dx:=  4E-9 // Cellsize (in m) along x direction
dy:=  4E-9 // Cellsize (in m) along y direction
dz:=  4E-9 // Cellsize (in m) along z direction
Nx:=ceil(length/dx) // Number of cells along x direction
Ny:=ceil(width/dy) // Number of cells along y direction
Nz:=ceil(thickness/dz) // Number of cells along z direction
SetGridsize(Nx,Ny,Nz)
SetCellsize(dx,dy,dz)
setgeom(imageShape(mask))

////////////////////////////////
/// INITIAL STATE ////
////////////////////////////////
m = Uniform(1,1,0)

////////////////////////////////////////
////// EXTERNAL FIELD //////
////////////////////////////////////////
tableadd(B_ext)
B:=0.0
B_max:= 200.0E-3 //Maximum field for hysteresis in T
//B_nuc1:=-153.0E-3 //Field before nucleation of AV
B_nuc1:=-150.0E-3 //Field before nucleation of AV
step1:=(B_nuc1-B_max)/2
B_nuc2:=-154.0E-3 //Field after nucleation of AV
B_ann1:=-158.0E-3 //Field after annihilation of AV
step2:=(B_ann1-B_nuc2)/2
//B_ann2:=-161.0E-3 //Field after annihilation of AV
B_ann2:=-165.0E-3 //Field after annihilation of AV
```

Figure C.1. Example script to run 3D simulations of hysteresis loops on an AV-hosting pound-key structure with total width of 400 nm using MuMax^3.

```
for B=B_max; B >= B_nuc1; B+=step1{
 B_ext = vector(B*Cos(ang),B*Sin(ang),0)
 if B==B_max{TableAddVar(B*1E3,"Field","mT")}
 relax()
 tableSave()
 saveas(m,sprint(outfile,"_B",floor(B*1E3),"mT"))
 print("External Field: ",B*1E3,"mT;  ", B_ext)
}

for B=B_nuc1-1E-3; B >= B_nuc2; B+=-1E-3{
 B_ext = vector(B*Cos(ang),B*Sin(ang),0)
 relax()
 tableSave()
 saveas(m,sprint(outfile,"_B",floor(B*1E3),"mT"))
 print("External Field: ",B*1E3,"mT;  ", B_ext)
}

for B=B_nuc2+step2; B >= B_ann1; B+=step2{
 B_ext = vector(B*Cos(ang),B*Sin(ang),0)
 relax()
 tableSave()
 saveas(m,sprint(outfile,"_B",floor(B*1E3),"mT"))
 print("External Field: ",B*1E3,"mT;  ", B_ext)
}

for B=B_ann1-1E-3; B >= B_ann2; B+=-1E-3{
 B_ext = vector(B*Cos(ang),B*Sin(ang),0)
 relax()
 tableSave()
 saveas(m,sprint(outfile,"_B",floor(B*1E3),"mT"))
 print("External Field: ",B*1E3,"mT;  ", B_ext)
}

for B=B_ann2-1E-3; B >= -B_max; B+=step1{
 B_ext = vector(B*Cos(ang),B*Sin(ang),0)
 relax()
 tableSave()
 saveas(m,sprint(outfile,"_B",floor(B*1E3),"mT"))
 print("External Field: ",B*1E3,"mT;  ", B_ext)
}
```

Figure C.2. Example script to run 3D simulations of hysteresis loops on an AV-hosting pound-key structure with total width of 400 nm using MuMax^3. Continued

```
/* MuMax3
################################################################
# Script to get apply a gaussian pulse a given angle to a sample containing antivortices
# For a gaussian pulse, FWHM =2 sqrt(2*ln2)*sigma  & sigma= FWHM/(2*sqrt(2*ln2))=FWHM/2.35482
Created on 04/16/2015 by Martin Asmat-Uceda - Colorado State university
Last modified on 06/06/2015 by Martin Asmat-Uceda
################################################################
*/
////////////////////////////////////////
////// FILES AND CONSTANTS //////
////////////////////////////////////////
direc:=  "/media/kristen/titanic/titan/mumax/AVL_modes_map/"
mask:=  sprint(direc,"masks/AVL_mask_based_on_mfm.png")
m_0:=  sprint(direc,"initial_states/AVL_2L3_024um_t37nm_initAV_and_paral_relaxed_and_250ns.ovf")
outfilebase:= "AVL_2L3_024um_t37nm_initAV_and_paral_inplane_pulse"

////////////////////////////////
// MATERIAL PARAMETERS //
////////////////////////////////
// for Permalloy //
Msat  = 8.0E5   //saturation magnetization for Py (in A/m)
Aex   = 1.3E-11   //exchange constant (in J/m)
alpha = 0.01   //damping constant (unitless) for static case

////////////////////////////////
/// GEOMETRY AND MESH ///
////////////////////////////////
//sample dimensions in m//
width:=  3024E-9
height:= 3024E-9
thickness:=   37E-9
//mesh and cell dimensions//
dx:=  4E-9 // Cellsize (in m) along x direction
dy:=  4E-9 // Cellsize (in m) along y direction
dz:=  37E-9 // Cellsize (in m) along z direction
Nx:=ceil(width/dx) // Number of cells along x direction
Ny:=ceil(height/dy) // Number of cells along y direction
Nz:=ceil(thickness/dz) // Number of cells along z direction
SetGridsize(Nx,Ny,Nz)
SetCellsize(dx,dy,dz)
setgeom(imageShape(mask))

//////////////////////////////
////// INITIAL STATE //////
//////////////////////////////
m.loadfile(m_0)  //loads initial magnetization from ovf file

//////////////////////////////
//// EXTERNAL FIELD ///
//////////////////////////////
B_amp:= 5.0E-4  // External magnetic field (in T) (1E-4 T = 1 Oe)
ang:= 45*pi/180  // Angle (in deg) at which the magnetic field is applied
t0:=1.0E-9;
FWHM:=30.0E-12;
sigma:=FWHM/2.35482;
B_ext=vector(B_amp*exp(-pow((t-t0)/sigma,2)/2)*cos(ang), B_amp*exp(-pow((t-t0)/sigma,2)/2)*sin(ang), 0)

//////////////////////////////
////////   SAVE   /////////
//////////////////////////////
tableadd(B_ext)
tableautosave(10E-12)
autosave(m,25E-12) //FFT max frequency is (2*sampling rate)^-1,then 25E-12 s, leads to max freq of 20GHz

//////////////////////////////
/// RUN SIMULATION ///
//////////////////////////////
MaxDt=0.5E-12
run(31E-9)
```

Figure C.3. Example script to apply a Gaussian magnetic field to an AV-hosting pound-key structure with a total width of 3024 nm using MuMax^3.

```
# MIF 2.1
# Script to relax a tri-disk system after removing an initial field
# Created on Dec. 09, 2013 by Martin Asmat-Uceda. Colorado State University
# Last modified on Dec. 09, 2013 by Martin Asmat-Uceda
#############################################################################################
set pi [expr 4*atan(1.0)]
set mu0 [expr 4*$pi*1e-7]  ;# in T.m/A
set Ms    860e3  ;# Saturation Magnetization for Permalloy in A/m
set alphaval  0.01   ;# Damping parameter
Parameter cellsize 4e-9  ;# in m
Parameter amp  40.0  ;# Amplitude of the applied field, in mT (1 mT = 10 Oe)
set length   2.128e-6 ;# in m
set width   1.984e-6 ;# in m
set thickness  0.030e-6 ;# in m
set mask_file  3disks_R126_D280.bmp
set init_dom_file 3disks_manyfields_test-Oxs_TimeDriver-Magnetization-00-0001802.omf
set outfilebase  ./3disks_manyfields_relax_test
########################################
Specify Oxs_ImageAtlas:atlas [subst {
  xrange {0 $length}
  yrange {0 $width}
  zrange {0 $thickness}
  viewplane xy
  image $mask_file
  colormap {
  black   magnetic
    white    nonmagnetic
  }}]
#######################################
Specify Oxs_RectangularMesh:mesh [subst {
  cellsize {$cellsize $cellsize $thickness}
  atlas :atlas}]
#######################################
Specify Oxs_UniformExchange {
  A  13E-12}
 #######################################
Specify Oxs_Demag {}
 #######################################
Specify Oxs_UZeeman [subst {
  multiplier $amp
  Hrange {
    {0 0 0 0 0 0 1}
  }}]
#######################################
Specify Oxs_RungeKuttaEvolve:evolver [subst {
  alpha $alphaval}]
#######################################
Specify Oxs_TimeDriver [subst {
 basename $outfilebase
 vector_field_output_format {binary 4}
 scalar_output_format %.15g
 evolver evolver
 mesh :mesh
 stopping_dm_dt 1
 stage_count 0
 Ms {Oxs_AtlasScalarField {
   atlas :atlas
   values {
     nonmagnetic  0
   magnetic    $Ms
 } } }
 m0 { Oxs_FileVectorField {
   atlas :atlas
   norm  1
   file $init_dom_file
 } }}]
#######################################
Destination archive mmArchive
Destination dispgraph mmGraph
Destination disp mmDisp
#######################################
Schedule DataTable dispgraph step 10
Schedule DataTable archive step 100
Schedule Oxs_TimeDriver::Magnetization disp step 10
Schedule Oxs_TimeDriver::Magnetization archive stage 100
```

Figure C.4. Example script to run OOMMF simulations of a tri-disk system (each with a radius of R=126 nm and thickness of 40 nm) that relaxes towards equilibrium after the removal of a magnetic field.

APPENDIX D

AV MODE MAPS

The dynamic behavior of the normal modes can be visualized by advancing the phase, ϕ, in $Acos(\omega + \phi)$ over a full period, where A and ϕ are the amplitude and phase at each position for a particular mode and ω is the mode frequency. The sequences of images that unveil this evolution of the modes are presented below for selected mode frequencies. All the images were obtained following the method described in 3.2.3 for simulations of the response of a Permalloy sample with leg's width of 2 μm and 37 nm thick to a 0.1 mT, 30 ps, short in-plane Gaussian pulse applied along the diagonal at $\pi/4$ degrees (w.r.t the horizontal axis). Cell size was $4 \times 4 \times 37$ nm^3, and material parameters used were typical for Permalloy: exchange stiffness constant $A = 1.3 \times 10^{-11} J/m$, saturation magnetization, $M_s = 8.0 \times 10^5 A/m$, gyromagnetic ratio, $\gamma = 1.76 \times 10^{11} \mathrm{s}^{-1}\mathrm{T}^{-1}$, damping constant, $\alpha = 0.01$ and magnetocrystalline anisotropy was neglected.

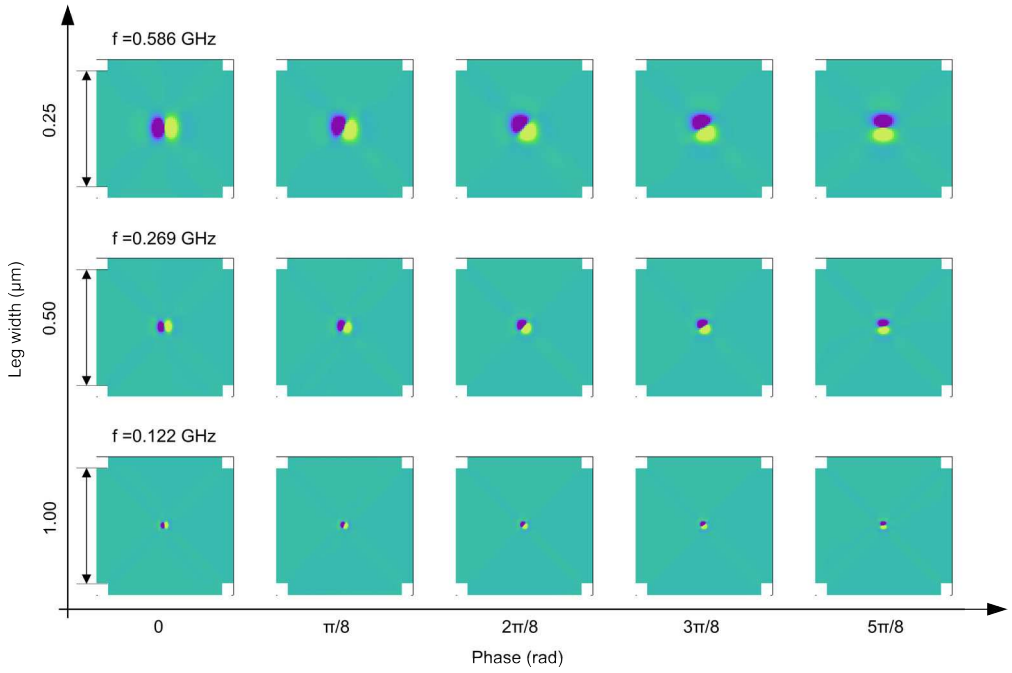

Figure D.1. Phase evolution of the f_g gyromode of an AV, for different leg widths, excited with an IP pulsed magnetic field.

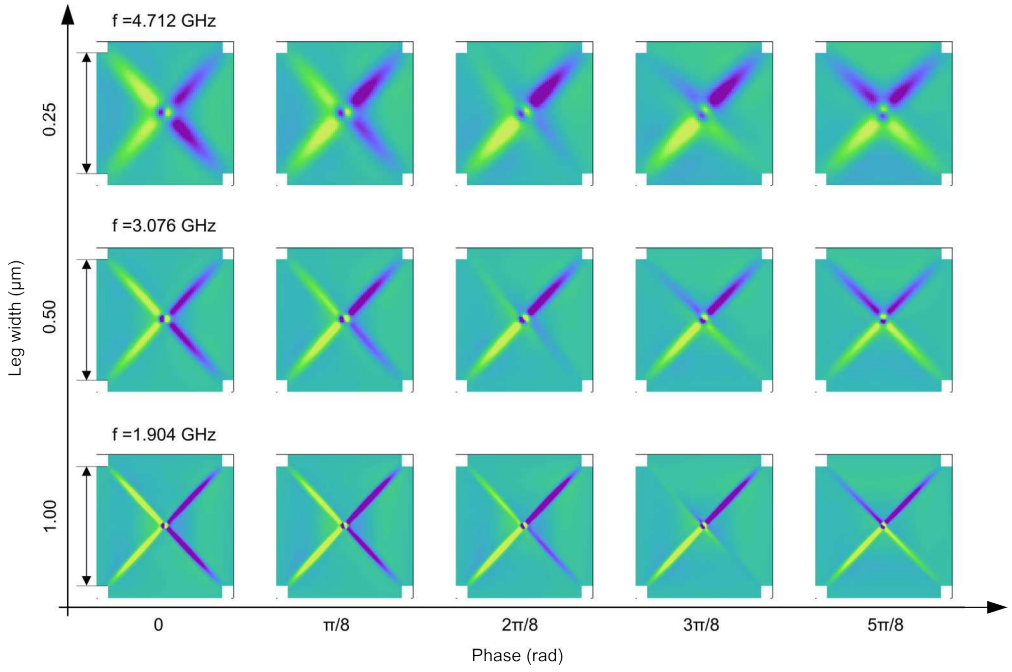

Figure D.2. Phase evolution of the f_{1a} azimuthal mode of an AV, for different leg widths, excited with an IP pulsed magnetic field.

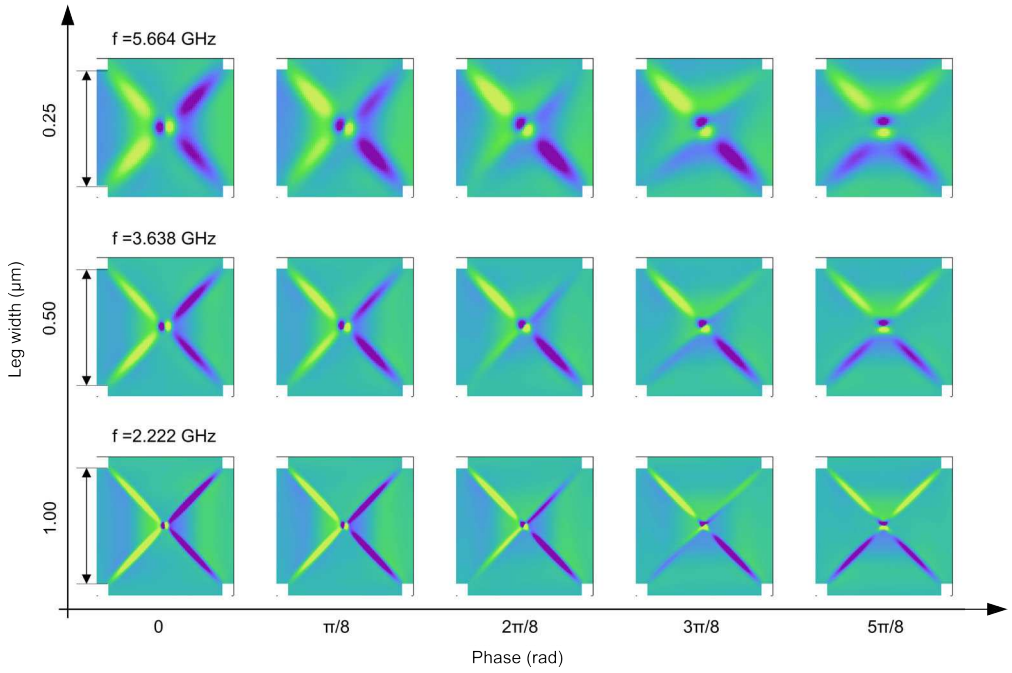

Figure D.3. Phase evolution of the f_{1b} azimuthal mode of an AV, for different leg widths, excited with an IP pulsed magnetic field.

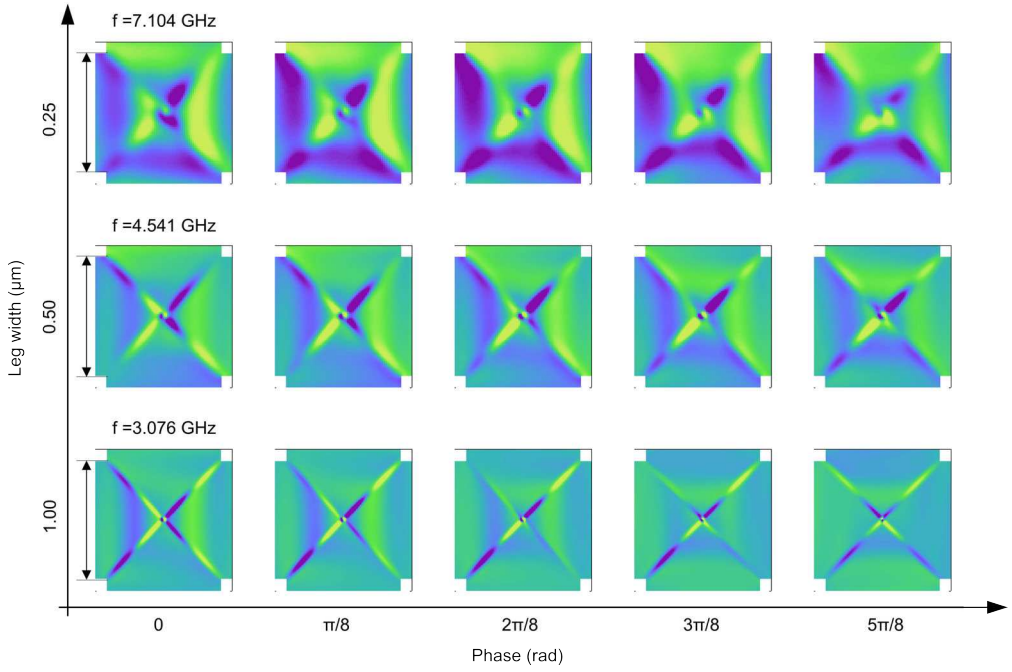

Figure D.4. Phase evolution of the f_{2a} azimuthal mode of an AV, for different leg widths, excited with an IP pulsed magnetic field.

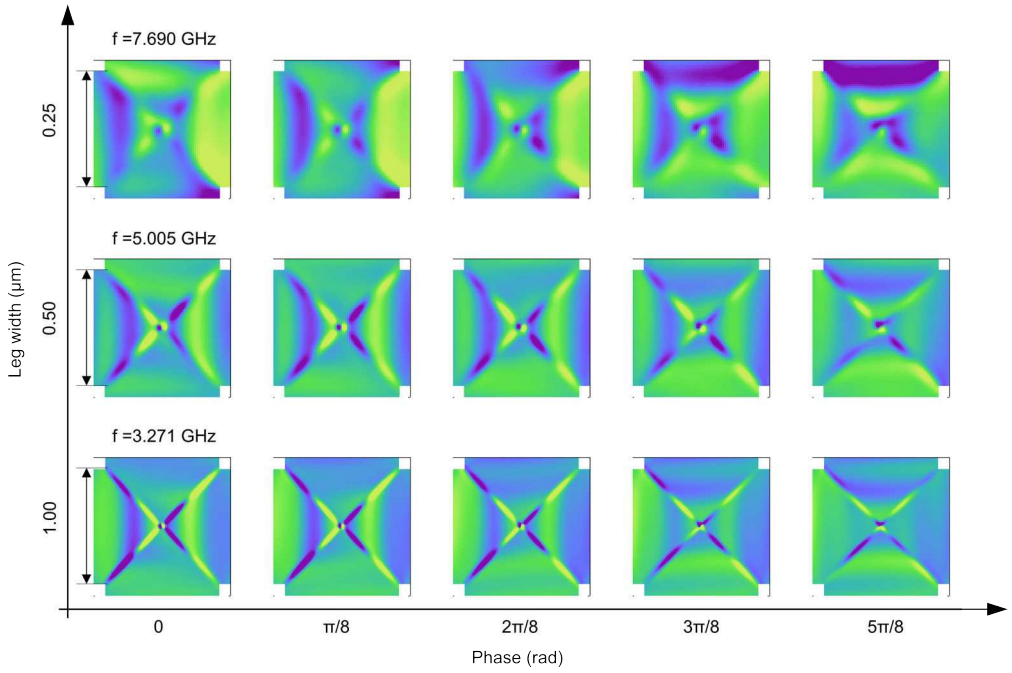

Figure D.5. Phase evolution of the f_{2b} azimuthal mode of an AV, for different leg widths, excited with an IP pulsed magnetic field.

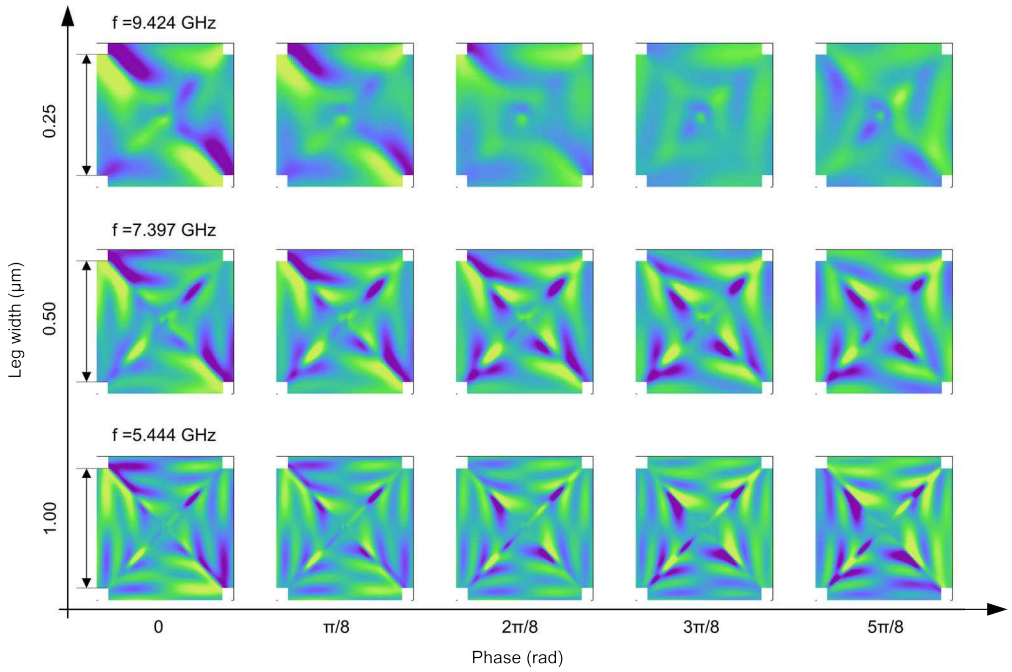

Figure D.6. Phase evolution of the f_{pip} mode of an AV, for different leg widths, excited with an IP pulsed magnetic field.

APPENDIX E

Mathematical derivation of eigenfrequencies for tri-disk system

The basic mathematical procedure to find the eigenfrequencies of coupled vortices, used in the analytical model presented in the Tri-disk chapter and published in reference [**?**], is presented in the following lines. The methods used in such references are the same as here, however more steps are included in the derivation below. Since such model considered dipolar interactions only, we start with the expression for the energy of two interacting dipoles d_i and d_j:

$$E_{dip} = \frac{\mu_o}{4\pi D_{ij}^3}\left(\vec{d_i}\cdot\vec{d_j} - 3(\hat{D_{ij}}\cdot\vec{d_i})(\hat{D_{ij}}\cdot\vec{d_j})\right)$$

but the dipolar magnetic moment of a vortex, when the core is displaced a distance $\vec{x}$ from its equilibrium position, is given by

$$\vec{d} = -C\chi M_s t R\hat{z}\times\vec{x}$$

then

$$E_{dip} = \frac{\mu_o(-CM_s tR)^2\chi_i\chi_j}{4\pi D_{ij}^3}\left((\hat{z}\times\vec{x_i})\cdot(\hat{z}\times\vec{x_j}) - 3(\hat{D_{ij}}\cdot(\hat{z}\times\vec{x_i}))(\hat{D_{ij}}\cdot(\hat{z}\times\vec{x_j}))\right)$$

then use:

$$(\vec{a}\times b)\cdot(\vec{c}\times\vec{d}) = (\vec{a}\cdot\vec{c})(\vec{b}\cdot\vec{d}) - (\vec{a}\cdot\vec{d})(\vec{b}\cdot\vec{c})$$

to get:

$$E_{dip} = k_2 \chi_i \chi_j \left((\hat{z} \cdot \hat{z})(\vec{x_i} \cdot \vec{x_j}) - (\hat{z} \cdot \vec{x_j})(\vec{x_i} \cdot \hat{z}) - 3(\hat{D_{ij}} \cdot (\hat{z} \times \vec{x_i}))(\hat{D_{ij}} \cdot (\hat{z} \times \vec{x_j})) \right)$$

where:

$$k_2 = \frac{C^2 \mu_o M_s^2 t^2 R^2}{4\pi D^3}$$

Since x_i is in plane vector and $\hat{z}$ is out of plane, the dot product is zero; then:

$$E_{dip} = k_2 \chi_i \chi_j \left((\hat{z} \cdot \hat{z})(\vec{x_i} \cdot \vec{x_j}) - 3(\hat{D_{ij}} \cdot (\hat{z} \times \vec{x_i}))(\hat{D_{ij}} \cdot (\hat{z} \times \vec{x_j})) \right)$$

Use circular property of triple product to get:

$$E_{dip} = k_2 \chi_i \chi_j \left(\vec{x_i} \cdot \vec{x_j} - 3(\hat{z} \cdot \hat{D_{ij}} \times \vec{x_i})(\hat{z} \cdot \hat{D_{ij}} \times \vec{x_j}) \right)$$

to take advantage of the symmetry, we set the two disks along the x-axis

$$D_{ij} = \hat{x}$$

we have

$$E_{dip} = k_2 \chi_i \chi_j \left(x_i x_j + y_i y_j - 3 y_i y_j \right)$$

Compare with general expression:

$$E_{int} = \chi_i \chi_j \left(n_x x_i x_j + n_y y_i y_j + O(|\vec{(}x_j)|^3) \right)$$

In our simple case

$$n_x = k_2, n_y = -2k_2$$

For three disks:

$$E_{int} = k_2\left[(x_1x_2 + y_1y_2) - 3(y_1)(y_2)\right] + k_2\left[(x_1x_3 + y_1y_3) - 3(\frac{y_1}{2} - \frac{\sqrt{3}x_1}{2})(\frac{y_3}{2} - \frac{\sqrt{3}x_3}{2})\right] + k_2\left[(x_2x_3 + y_2y_3) - 3(\frac{y_2}{2} + \frac{\sqrt{3}x_2}{2})(\frac{y_3}{2} + \frac{\sqrt{3}x_3}{2})\right]$$

from where, we have:

$$E_{int} = k_2\left[x_1x_2 - 2y_1y_2\right] + k_2\left[\left(1 - \frac{9}{4}\right)x_1x_3 + \left(1 - \frac{9}{4}\right)x_2x_3\right] + k_2\left[\left(1 - \frac{3}{4}\right)y_1y_3 + z + \left(1 - \frac{3}{4}\right)y_2y_3\right] + k_2\left[\left(\frac{3\sqrt{3}}{4}\right)x_1y_3 + \left(\frac{-3\sqrt{3}}{4}\right)x_2y_3\right] + k_2\left[\left(\frac{-3\sqrt{3}}{4}\right)y_2x_3 + \left(\frac{3\sqrt{3}}{4}\right)y_1x_3\right]$$

Then

$$E_{int} = k_2\left(x_1x_2 - 2y_1y_2 - \frac{5}{4}(x_1 + x_2)x_3 + \frac{1}{4}(y_1 + y_2)y_3 - (\frac{3\sqrt{3}}{4})(x_2 - x_1)y_3 - -(\frac{3\sqrt{3}}{4})(y_2 - y_1)x_3\right)$$

This expression can be written in a similar way to the general expression with n_x and n_y defined earlier. Also, we could define new coordinates

$$\overline{x} = \frac{(x_1 + x_2)}{\sqrt{2}}\ ,\ \overline{y} = \frac{(y_1 + y_2)}{\sqrt{2}}\ , \qquad d = \frac{(x_2 - x_1)}{\sqrt{2}}\ \text{, and } \Delta = \frac{(y_2 - y_1)}{\sqrt{2}}$$

To have:

$$E_{int} = k_2\left(x_1x_2 - 2y_1y_2 - \frac{5}{4}\overline{x}x_3 + \frac{1}{4}\overline{y}y_3 - \frac{3\sqrt{3}}{4}dy_3 - \frac{3\sqrt{3}}{4}\Delta x_3\right)$$

Now, remember that the Lagrangian for any number of disks is given by:

$$L = \sum_i -pG\dot{x}_i y_i - \frac{k}{2}|x|^2 - \sum_{i<j} E_{dip}^{ij}$$

Let's first take a look at the lagrangian for two disks:

$$L = -p_1 G(\dot{x}_1 y_1 - \dot{y}_1 x_1) - p_2 G(\dot{x}_2 y_2 - \dot{y}_2 x_2) - \frac{k}{2}(x_1^2 + y_1^2) - \frac{k}{2}(x_2^2 + y_2^2) - k_2(x_1 x_2 - 2y_1 y_2)$$

And using the Lagrange equations:

$$\frac{d}{dt}\left(\frac{\partial L}{\partial \dot{q_n}}\right) - \frac{\partial L}{\partial q_n} = 0$$

We get:

$$\frac{d}{dt}(-p_1 G y_1) - (-kx_1 - k_2 x_2) = 0$$
$$\frac{d}{dt}(-p_1 G x_1) - (-ky_1 + 2k_2 y_2) = 0$$
$$\frac{d}{dt}(-p_2 G y_2) - (-kx_2 - k_2 x_1) = 0$$
$$\frac{d}{dt}(-p_2 G x_2) - (-ky_2 + 2k_2 y_1) = 0$$

that can be expressed as:

$$\begin{pmatrix} 0 & -p_1G & 0 & 0 \\ p_1G & 0 & 0 & 0 \\ 0 & 0 & 0 & -p_2G \\ 0 & 0 & p_2G & 0 \end{pmatrix} \begin{pmatrix} \dot{x_1} \\ \dot{y_1} \\ \dot{x_2} \\ \dot{y_2} \end{pmatrix} = \begin{pmatrix} -kx_1 - k_2x_2 \\ -ky_1 + 2k_2y_2 \\ -kx_2 - k_2x_1 \\ -ky_2 + 2k_2y_1 \end{pmatrix}$$

This can be rearranged to give:

$$G \begin{pmatrix} \dot{x_1} \\ \dot{x_2} \\ \dot{y_1} \\ \dot{y_2} \end{pmatrix} = \begin{pmatrix} 0 & 0 & -kp_1 & 2k_2p_1 \\ 0 & 0 & 2k_2p_2 & -kp_2 \\ kp_1 & k_2p_1 & 0 & 0 \\ k_2p_2 & kp_2 & 0 & 0 \end{pmatrix} \begin{pmatrix} x_1 \\ x_2 \\ y_1 \\ y_2 \end{pmatrix}$$

And the eigenfrequencies can be found from the characteristic equation:

$$\begin{vmatrix} -\omega & 0 & -kp_1 & 2k_2p_1 \\ 0 & -\omega & 2k_2p_2 & -kp_2 \\ kp_1 & k_2p_1 & -\omega & 0 \\ k_2p_2 & kp_2 & 0 & -\omega \end{vmatrix} = 0$$

from where:

$$-\omega \begin{vmatrix} -\omega & 2k_2p_2 & -kp_2 \\ k_2p_1 & -\omega & 0 \\ kp_2 & 0 & -\omega \end{vmatrix} - kp_1 \begin{vmatrix} 0 & -\omega & -kp_2 \\ kp_1 & k_2p_1 & 0 \\ k_2p_2 & kp_2 & -\omega \end{vmatrix} - 2k_2p_1 \begin{vmatrix} 0 & -\omega & 2k_2p_2 \\ kp_1 & k_2p_1 & -\omega \\ k_2p_2 & kp_2 & 0 \end{vmatrix} = 0$$

breaking it down:

$$\omega\left[\omega^3-(2k_2^2p_1p_2-k^2p_2^2)\omega\right]+kp_1\left[kp_1\omega^2+kp_2(k^2-k_2^2)p_1p_2)\right]$$
$$-2k_2p_1\left[k_2p_2\omega^2+2k_2p_2(k^2-k_2^2)p_1p_2)\right]=0$$

then:

$$\omega^4+\left[-(2k_2^2p_1p_2-k^2p_2^2)+(kp_1)^2-2k_2^2p_1p_2\right]\omega^2+\left[k^2(k^2-k_2^2)(p_1p_2)^2\right.$$
$$\left.-4k_2^2(k^2-k_2^2)(p_1p_2)^2\right]=0$$

then:

$$\omega^4+\left[k^2(p_1^2+p_2^2)-4k_2^2p_1p_2\right]\omega^2+\left[k^4-5(kk_2)^2+4k_2^4\right](p_1p_2)^2=0$$

$$\omega^2=\frac{-k^2(p_1^2+p_2^2)+4k_2^2p_1p_2\pm\sqrt{\left[k^2(p_1^2+p_2^2)-4k_2^2p_1p_2\right]^2-4\left[k^4-5(kk_2)^2+4k_2^4\right](p_1p_2)^2}}{2}$$